CO_2 methanation over Ni and its structure sensitivity

A computational study

Master Thesis
E. B. Sterk

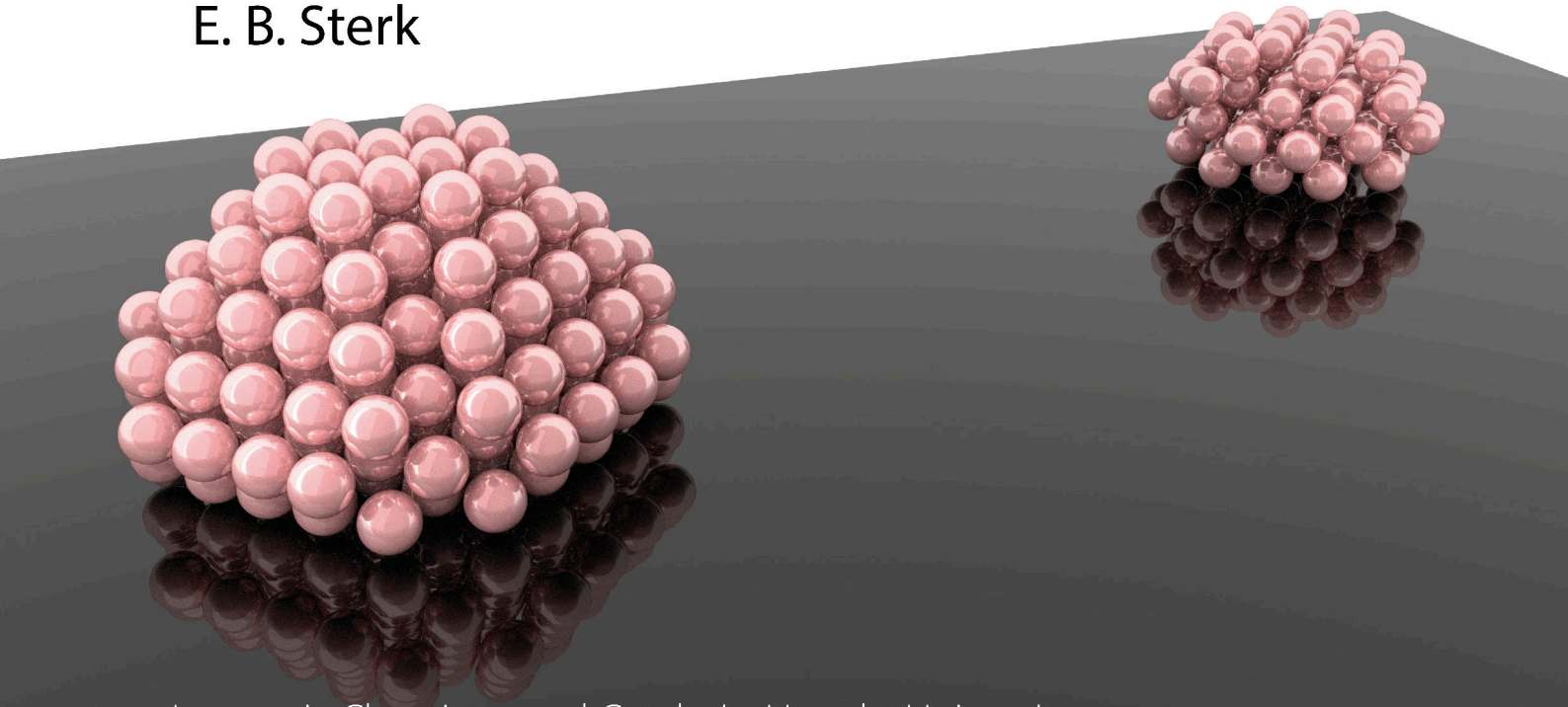

Inorganic Chemistry and Catalysis, Utrecht University
Supervisors:
Daily: MSc. C. Vogt (UU)
Dr.ir. I. A. W. Filot (TUe)
Prof.dr.ir. B. M. Weckhuysen (UU)
June 2018

Progress in science is not a simple line leading to the truth. It is more progress away from less adequate conceptions of, and interactions with, the world. [1]

Thomas S. Kuhn (1922-1996)

Abstract

The methanation of CO_2 is a reaction with the potential to reduce the negative environmental impact of CO_2 point sources and at the same time increase the large scale applicability of renewable electricity. CO_2 emitted at point sources, such as cement or steel factories, can be captured and catalytically converted towards methane over supported nickel catalysts with the use of renewably produced hydrogen. Interestingly, CO_2 hydrogenation over supported nickel nanoparticles is a structure sensitive reaction and the reaction intermediates are IR-active. This makes CO_2 hydrogenation over nickel an excellent model reaction to gain a more thorough understanding of the mechanisms behind structure sensitivity. However, the reaction mechanism is not yet fully understood. Three reaction mechanisms are postulated to be active in CO_2 hydrogenation over nickel. Firstly, direct CO_2 dissociation, secondly H-assisted CO dissociation via alcohol intermediates and thirdly H-assisted CO dissociation via formate intermediates.

The goal of this theoretical study is to explain observations from previously performed FR-IR-experiments, and thereby unravel the reaction mechanism through which CO_2 methanation over nickel is energetically most favorable. Finally, by understanding which nickel facet is most favorable in CO_2 hydrogenation, the aim is to understand observed structure sensitive effects.

An extensive DFT study is performed of all possible reaction intermediates in Ni-catalyzed CO_2 hydrogenation on four different facets; Ni(111), Ni(100), Ni(110) and Ni(211). In this way, sets of stable geometries of each reaction intermediate were obtained, which were used to study each elementary reaction step of the three reaction mechanisms (carbide, formate, alcohol) on the four nickel facets.

The results demonstrate that CO_2 hydrogenation likely proceeds via the carbide mechanism, with hydrogen-assisted CO^* dissociation. CO^* dissociation was found to be most facile via COH^* on Ni(100), Ni(110) and Ni(211) and via HCO^* on Ni(111). CO_2 hydrogenation was found to be energetically least demanding over Ni(110) with a rate limiting step of 110 kJ/mol. However, a combination of the four nickel facets results in a mechanism with the overall lowest energy profile with a rate limiting step of 99 kJ/mol.

Contents

List of Figures

List of Tables

1 Methanation - History and Potential Impact

In the first section of this chapter the physical origin of global warming is explained by means of vibrational energy and the quantized energy of sunlight. The severity of global warming is illustrated using results of temperature analyses. In the second section the research project is introduced, both as a potential contribution to the solution on the greenhouse effect as well as a method to elucidate the fundamental mechanisms behind structure sensitivity. The subsequent section give a historical introduction to the definition of catalysis by means of one of the first publications on catalysis. Thereafter, reactions on catalytic surfaces as well as the phenomenon of structure sensitivity are briefly explained.

1.1 Global Warming

The average temperature on Earth is not static. It fluctuates depending on seasons, but also weather factors such as cloudiness do play a role. Generalized, the temperature on Earth depends on the amount of energy, or heat, that enters and leaves the atmosphere. In case of the Earth, the sun is the largest provider of energy in the form of sunlight. Part of the direct sunlight heats the surface of the Earth, another part is re-radiated back into the universe by surfaces with a high refractive index such as ice and clouds.

So-called greenhouse gases in the atmosphere are able to absorb radiated energy. This phenomenon can be explained by the dual nature of (sun)light and the quantized vibrational energy of molecules. The duality of light can be described as having properties of both waves and of particles. The propagation, diffraction and interference of light can be described by a wave model, in which light is described as an electromagnetic wave [2]. The particle aspect of light is such that the energy, which is carried by light waves, is packaged in discrete bundles termed photons or quanta. The energy of a single photon is given by Equation 1.1, where h is Planck's constant and ν is the frequency of the radiation [2].

$$E = h\nu \tag{1.1}$$

The vibrational potential energy of molecules is also quantized, which means that for a given molecule the energy can't have just any value and consequently, it can only adsorb specific, or discrete, amounts of energy. This is illustrated with a model of a vibrating diatomic molecule in which the bond between the two atoms behaves like a spring, shown on the left hand side in Figure 1.1. The energy of this system as a function of the distance between the atoms can be described by the Morse potential, shown on the right in Figure 1.1. As the distance r decreases, the atoms come together and start to repel each other. This repulsion grows very strong at small values of r. When r becomes very big, the molecule dissociates and the energy goes to a constant value, which represents the energy of each of the two atoms separately. The minimum vibrational energy of the molecule is slightly higher than the bottom of the potential well. The reason for this has to do with the uncertainty principle that states that any quantum state (e.g. the ground state) must possess intrinsic uncertainty [3], thereby asserting a fundamental limit to the precision with which a quantum state can be determined. This is in line with the fact that in quantum mechanics, which will be dealt with in Chapter 3, properties of a particle are described by probability distributions [4]. This means that there cannot exist a state in which the two atoms from Figure 1.1 are motionless, which would be required if the vibrational energy of the diatomic system equals the energy in the bottom of the potential well, because then the uncertainty of both the position and momentum of

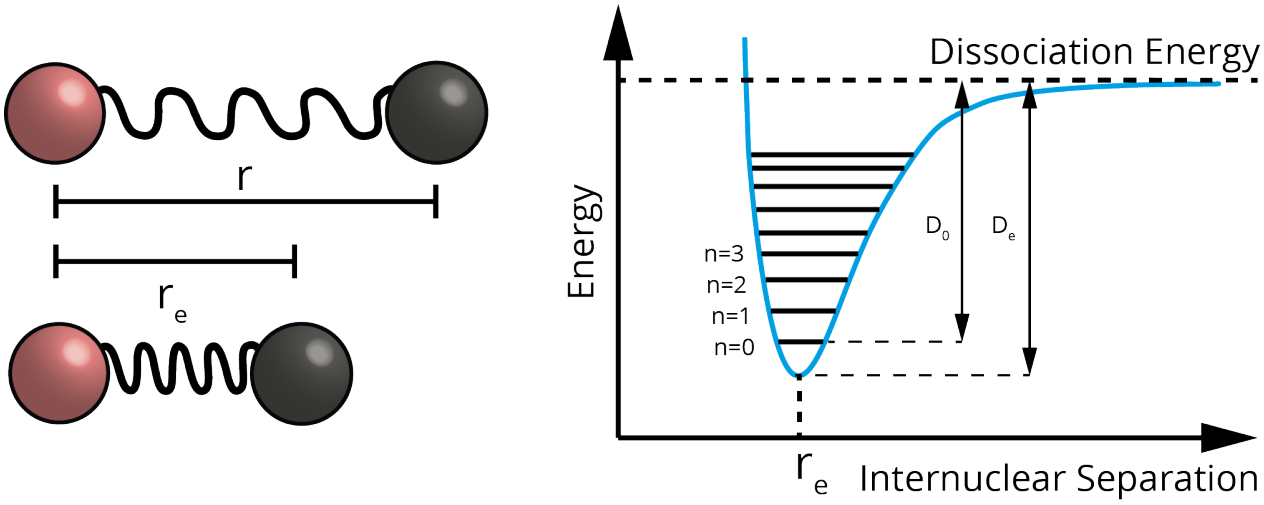

Figure 1.1: A model for the vibration of a diatomic molecule and a Morse potential energy curve for the vibration of a molecule

the system would be zero. Therefore, the ground state energy of the system must be larger than the minimum of the potential well.

This so called zero-point vibrational energy is the ground state in which the atoms vibrate with a certain frequency around the equilibrium position r_e along their bond. The energy of a vibrating molecule is quantized and the discrete vibrational energy levels are given by Equation 1.2 [4]. D_e is the dissociation energy with respect to the bottom of the potential well, D_0 is the dissociation energy with respect to the ground-state vibrational energy and β is a measure of the curvature at the bottom of the potential well. Only molecules with a changing dipole moment, onset by their vibrations, are able to interact with light and adsorb energy with the same magnitude as the differences in energy of the vibrational states [5]. This adsorption of energy can change the vibrational energy of the system from its ground state, n=0, to a higher excited state.

$$E_{vib} = D_e(1 - e^{-\beta(r-r_e)})^2 \qquad \text{with} \qquad D_e = D_0 + \frac{1}{2}h\nu \tag{1.2}$$

The energy of the infrared region of sunlight is sufficient to excite vibrations of certain molecules that are present in the atmosphere. The energy adsorbed by these gases can be released again by the emission of a photon, which occurs in all directions. The energy that radiates back towards Earth heats the lower atmosphere as well as the surface of the planet, thereby adding on to the heat the atmosphere already gets from direct sunlight. The absorption and radiation of heat by the atmosphere, often termed as the natural greenhouse effect, is necessary to support life on Earth. To illustrate the importance, if there was no greenhouse effect the average surface temperature would be -18 °C [6].

Both human and natural factors contribute to the amount of greenhouse gases in the atmosphere, and thus the warmth on Earth. An example of a natural contribution is the eruption of a volcano. During the eruption several gases and ash clouds are emitted into the atmosphere. Released sulphur dioxide and the ashes are able to reflect sunlight away from the earth, so these compounds have a cooling effect on the Earth. During the eruption of a volcano a lot of carbon dioxide, carbon monoxide and methane are released which are able to absorb heat or infrared radiation from the sun, after which this heat is re-radiated in all directions including towards the earth. Thus they

will have a warming effect on the Earth. Many greenhouse gases occur naturally in the atmosphere, such as water vapor, carbon dioxide, methane and nitrous oxide. However, there are also man-made greenhouse gases like chlorofluorocarbons and hydro-fluorocarbons which are used in e.g. refrigeration, aerosol propellants and air conditioning.

The Intergovernmental Panel on Climate Change (IPCC) compared the relative influence exerted by several climate drivers like key heat-trapping gases, aerosols and land use change of human origin on our climate between 1750 and 2005. For several climate drivers the increase or decrease in the total amount of energy reaching the surface of the Earth was calculated. The results of this

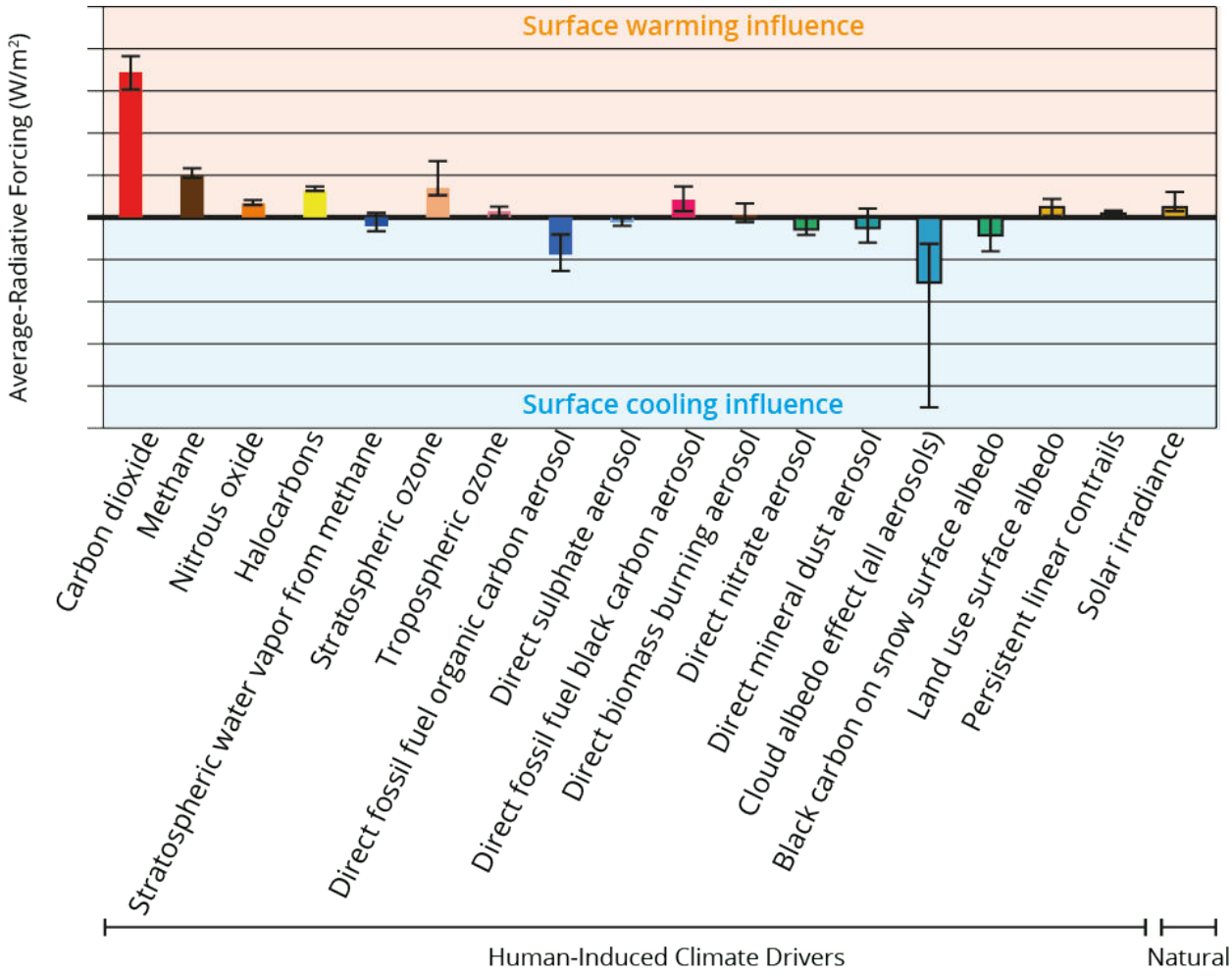

Figure 1.2: Climate influence between 1750 and 2005. Carbon dioxide, more than any other climate driver, has contributed the most to climate change. (From IPCC [7]).

research are presented in Figure 1.2. Even tough CH_4 is a more efficient greenhouse gas (traps more heat) than CO_2 does, due to the higher total bond enthalpy, it was found that CO_2 has the largest contribution to global warming of all the human-influenced climate drivers compared by the IPCC [7].

When all warming and cooling effects of all processes are in an overall balance, the temperature will fluctuate around a more or less constant value. However, since the start of the Industrial Revolution in 1750, the human contribution to the amount of greenhouse gases raised significantly. This is due to the emission of several heat trapping greenhouse gases into the atmosphere during the combustion of fossil fuels, thereby increasing the warmth captured in the Earth's atmosphere. This increase in captured energy is neither compensated by nature nor by humans. Therefore the overall effect of the increasing amount of greenhouse gases in the atmosphere is warming of the planet, also known as global warming.

According to a temperature analysis conducted by the NASA's Goddard Institute for Space Studies (GISS), the average global temperature on Earth has increased by 0.8 °C since 1880, from which $\frac{2}{3}$ of the warming has occurred since 1975 with 0.15-0.20 °C per decade [8]. To illustrate the gravity of the increase of the global temperature with 0.8 °C, in the period around 1300 to 1400 the average temperature decreased with 1.5 °C which marked a transition from the Medieval Warm Period to the Little Ice Age [9].

Because of the rising temperature, there has already been a change in the weather and climate. Some places on Earth have seen an increase in rainfall, which resulted in more severe floods. There are also places which experience more droughts which have a negative effect e.g. on the cultivation of crops. The oceans are warming and becoming more acidic, and ice caps are melting which increases the sea levels [10]. These and other changes will likely become larger and more apparent in the next few years, which will bring great challenges to our environment and society.

In order to stabilize the CO_2 concentration in the atmosphere society requires CO_2 negative emissions across from the rich CO_2 emission during the combustion of fossil fuels [11], [12]. A very drastic but unrealistic approach in aiming to solve the global warming problem would be a complete replacement of the usage of fossil fuel energy with renewable- or green- energy, for example based

on onshore and offshore winds, hydro-power, marine technologies like wave power and tidal energy, solar thermal energy, biomass and waste.

The development of green energy sources has made a great progress during the last decades. However, to switch the complete energy usage from fossil fuels towards green energy sources also depends on political and socio-economic factors besides the technological development of these sources [12]. For instance, switching towards green sources requires a large investment and it will take many years before this investment will be earned back. Another hampering aspect is the fact that current technology is based on fossil fuels. From lawnmowers to cargo boats, cooking on a gas stove, central heating and many industrial processes.

There are processes that will always emit CO_2, not because of the usage of fossil fuels, but because it is necessary chemical wise. The cement industry emits nearly 900 kg CO_2 for the production of 1000 kg cement [13]. This CO_2 emission originates from the process, as shown in Equation 1.3, which converts limestone ($CaCO_3$) to calcium oxide (CaO), the primary precursor to cement [13]. This makes the emission of CO_2 inevitable, because it is chemically impossible to convert limestone to calcium oxide without the release of CO_2.

$$CaCO_3 \longrightarrow CaO + CO_2 \tag{1.3}$$

All economic, political and practical factors make that there is not one big solution to global warming, but that there is a need for many different contributions toward a green society.

1.2 Potential Impact of CO_2 Hydrogenation

The contribution of this research project to the global warming problem, described in Section 1.1, is based upon the hydrogenation of the greenhouse gas CO_2 using H_2 to produce methane. The overall idea is summarized and presented in Figure 1.3. The required H_2 can be sustainably produced by water hydrolysis, for example from excess energy produced by solar cells. Solar cells produce the most energy during the day, which does not necessarily correspond with the main energy demand over the full day. However, currently solar cells cannot store all the excess energy they produce from solar radiation. Therefore, excess energy which is not stored on the grid or consumed directly

is sometimes discarded into the ground. This excess amount of energy from fields with a substantial amount of solar cells can be used to hydrolyze water, thereby producing the required hydrogen. Point sources of CO_2 like fossil fuel power plants, oil refineries or industrial process plants can be used as a CO_2 feed stock. Then, the hydrogenation reaction of CO_2 will actively reduce the amount of emitted CO_2 into the atmosphere, if applied in a closed cycle process during the transition from fossil fuels to renewable energy.

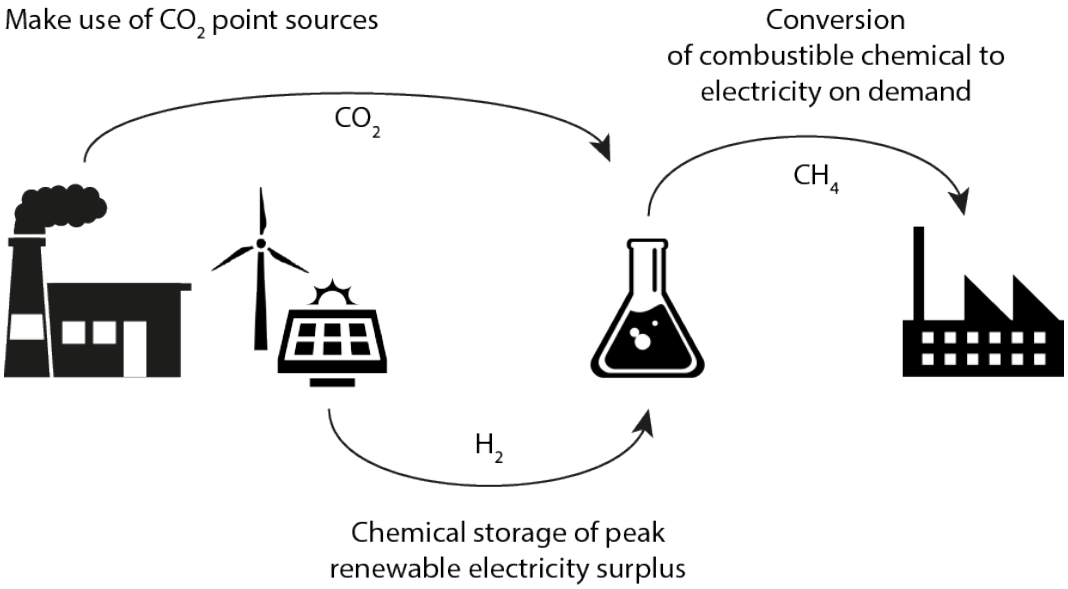

Figure 1.3: Overview of the potential contribution to the global warming problem. Produced hydrogen gas, made by using electricity surplus form renewable energy sources, is converted with CO_2 from point sources toward the combustible chemical methane.

As CO_2 shows the largest contribution to the greenhouse effect since 1750, CO_2 hydrogenation can be a convenient reaction to reduce the negative impact of CO_2 on the environment. The reaction equation of CO_2 hydrogenation is shown in Equation 1.4.

$$CO_2 + 4\,H_2 \overset{Ni}{\rightleftharpoons} CH_4 + 2\,H_2O\,. \tag{1.4}$$

This reaction was first reported by Sabatier and Senderens in 1902 [14]. They reported that CO_2 could be reduced by H_2 over different metals such as nickel, ruthenium, rhenium, platinum, iron and cobalt [14]. This reaction has a Gibbs free energy of -130.8 kJ/mol at 298 K, thermodynamically

favorable. However the reduction of the fully oxidized carbon to methane is an eight electron process with kinetic limitations, which thus requires a catalyst to achieve acceptable rates and selectivities [15]. For this reaction nickel was and still is the catalyst of choice in industries [16], although it has lower reaction rates, is less active and often requires higher reaction temperatures compared to the noble metals Pt, Ru, Rh and Pd. The significant advantage of nickel over these noble metals relies on its selectivity and its price [16].

The potential advantage of this process, besides the reduction of the negative impact on the environment, is that it reclaims CO_2 greenhouse gas by recycling it from exhaust fumes of industrial processes towards methane which can be used as an energy source. The specific energy of methane is -55.6 MJ/kg [17], which is rather low compared to -120 MJ/kg [18] for H_2 at 200bar. However, the density of H_2 (0.0899 kg/m^3 at STP) is much lower compared to CH_4 (0.717 kg/m^3 at STP) [19]. This makes direct usage of H_2 as an energy source very challenging in both the storage and distribution due to high pressures needed to compress H_2. Methane is attractive for large-scale storage of electricity because of its high conversion efficiency, the currently existing gas distribution infrastructure, such as pipelines, and the well-established and efficient end use technologies like compressed natural gas cars, heating and power stations [16].

The study of CO_2 hydrogenation has another fundamental importance besides the potential reduction of the negative impacts of CO_2 point sources. It can be very valuable to study this reaction, because we can use it as a fundamental study to gain a deeper understanding of the mechanisms behind structure sensitivity of heterogeneous catalytic reactions by metal nanoparticles. With this knowledge it might be possible to make more efficient catalysts in general, based on rational design. In the following sections catalysis and reactions on catalytic surfaces will be introduced after which structure sensitivity will be explained.

1.3 Introduction to Catalysis

Catalytic processes have been used by mankind for some thousands of years, for example in beer or wine fermentation. However, in general without truly realizing the existence of catalysts and the potential impact of catalytic processes. In 1806 the first attempt of a rational theory of catalysis was made by C.B. Désormes and N. Clément [20]. They proposed an intermediate compound theory for the *homogeneous* catalytic effect of nitrogen oxides in a lead chamber to produce sulphuric acid [20]. The reactions in this so called 'lead chamber process' took place in a series of very large lead-lined vaults [21]. The conversion of SO_2 to sulfuric acid with nitrogen oxide as a catalyst occurs in the following reaction sequence:

$$2\,NO + O_2 \longrightarrow 2\,NO_2 \tag{1.5}$$

$$SO_2 + NO_2 \longrightarrow SO_3 + NO \tag{1.6}$$

$$SO_3 + H_2O \longrightarrow H_2SO_4 \tag{1.7}$$

With the intermediate compound theory a catalyst bound to a reactant was described as an unstable intermediate compound, SO_3 in the above mentioned example, that either decomposed into the desired end product and the catalyst or reacts with an other reactant. Based on reaction equations 1.5 to 1.7 we now can conclude that the lead chamber process meets the latter option of the intermediate compound theory.

A decade later, after a thorough investigation and search for a safe miners lamp, the first publication of a *heterogeneous* catalytic reaction came out in 1817. At the beginning of the 19th century Sir Humphry Davy started with a survey to the reason and solution of the numerous explosions in coal mines in the North of England [22]. Davy was convinced that the accidents could only be prevented if the mines were lit in a safe manner without an open flame and if there was some sort of signal if the so called fire-damp - which is a mixture of atmospheric air and methane -

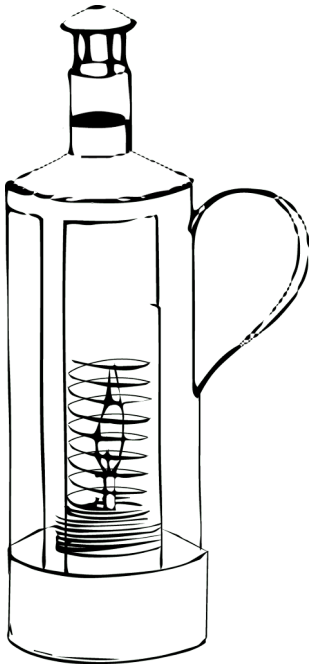

Figure 1.4: Miners safety lamp as developed by Humphry Davy. The coil of a fine platinum wire around the flame remains luminescent after the flame is extinguished when more firedamp enters the lamp.

was released during the work activities of the miners. Then the miners could leave until the level of the fire-damp was properly reduced. After systematic experimental work with the combustibility of different mixtures of fire-damp and a search to keep the fire-damp inside the lamp luminescent, Davy developed a so called miners' safety lamp depicted in Figure 1.4. For this lantern Davy fixed a thin platinum wire above a flame that originated from the combustion of firedamp. After the ignition of the damp Davy introduced more firedamp into the lantern, by which the flame extinguished and the hottest part of the platinum wire remained ignited and continued glowing for several minutes. This outcome was the exact thing that Davy was aiming for during his entire research. In his paper he wrote [23]:

"I was accidentally led to the knowledge of the fact, and, at the same time, to the discovery of a new and curious series of phenomena."

With the knowledge of today we can say that Davy had discovered the phenomenon of *heterogeneous* catalytic oxidation [22]. The reaction of methane and oxygen in the presence of platinum

is a heterogeneous catalytic oxidative reaction, with the following reaction equation:

$$CH_4 + 2\,O_2 \overset{Pt}{\rightleftharpoons} CO_2 + 2\,H_2O \tag{1.8}$$

In this reaction the methane that is present in the firedamp will be oxidized on the metal catalyst. An application of this reaction nowadays can be found in catalytic converters in vehicles in order to reduce the emission of unburnt hydrocarbons and carbon monoxide [18].

Even after these reported cases of catalysis, the concept of catalysis was still not yet defined. In the beginning of the 19th century awareness of the existence of catalytic processes started to arise. Every year J.J. Berzelius, a Swedish chemist, wrote a report of the complete progress in the field of chemistry for the Stockholm Academy of Sciences [20]. For this purpose he reviewed a number of findings on chemical change in both heterogeneous and homogeneous systems. In 1836 he published a report where he combined these findings in chemical change and gave a definition to the phenomenon of catalytic processes as a new force, he wrote [24]:

"It is, then, proved that several simple or compound bodies, soluble and insoluble, have the property of exercising on other bodies an action very different from chemical affinity. By means of this action they produce, in these bodies, decompositions of their elements and different recombination's of these same elements to which they remain indifferent."

Berzelius continued to propose the existence of a new force which he called the 'catalytic force' and he called 'catalysis' the decomposition of bodies by this force [20]. This definition of a catalyst has great resemblance to the definition which we use nowadays and is stated by the International Union of Pure and Applied Chemistry (IUPAC) [25]:

"A catalyst is a substance that increases the rate of a reaction without modifying the overall standard Gibbs energy change in the reaction."

1.4 Reaction Mechanisms

CO_2 hydrogenation over nickel nanoparticles to produce methane supported on SiO_2 is a heterogeneous catalytic reaction. In such gas/solid catalytic cycles at least one of the reactants must

be adsorbed on the metal surface [26]. This can either go via the Eley-Rideal or the Langmuir-Hinshelwood mechanism, which will be explained using the following reaction mechanism:

$$A + B \xrightarrow{cat} C \tag{1.9}$$

In the Eley-Rideal mechanism only one of the reactants, A for example, is adsorbed on the catalytic surface, denoted as A^* where the symbol * indicates an adsorbed state. Subsequently a gas molecule B reacts with chemisorbed A^* without being adsorbed itself, after which the chemisorbed product C^* either reacts further or desorbs from the catalytic surface [27]. An example of a reaction that is currently believed to follow the Eley-Rideal mechanism is the second reaction step in the production of CH_3OH by $CO_{2(g)}$ hydrogenation over Cu nanoparticles [28]. The first step is the dissociative adsorption of $H_{2(g)}$ on the catalytic Cu surface. Subsequently, $CO_{2(g)}$ reacts with an H^* adatom producing either $HCOO^*$ or $COOH^*$ [28].

In the Langmuir-Hinshelwood mechanism both reactants, A and B, are first adsorbed on the catalytic surface. Secondly, A^* and B^* migrate to each other after which they react to the chemisorbed product C^*, which either reacts further or desorbs into the gas phase [27].

The significant difference between these two mechanisms is that in the Eley-Rideal mechanism no free adsorption sites are needed, while for the Langmuir-Hinshelwood type of mechanism each reactant occupies an adsorption site on the metal surface. The Langmuir-Hinshelwood mechanism is much more common in heterogeneous catalysis, partly because the reactants are activated by the adsorption on the catalytic surface [26]. This is also the case in CO_2 hydrogenation over nickel [29].

1.5 Structure Sensitivity

Catalysis in heterogeneous catalytic systems mainly takes place on the surface of metal nanoparticles. Therefore the reaction can be considered a surface phenomenon in which the interactions of the reactants with the surface of the metal catalyst are essential for activity, selectivity and stability [26]. As a consequence the catalytic activity can be directly related to the amount of atoms on the surface of the metal nanoparticles. A larger surface area means, in principle, a greater catalytic activity. However, in a considerable number of cases the situation is not as straightforward

as hereby suggested. This has to do with the fact that the activity not only depends on the number of available surface sites, but also on the manner in which these atoms are orientated with respect to each other. A metal nanoparticle is not composed of a single surface facet like a flat terrace, but they show various irregularities like edges, corners, kinks and steps. The catalytic activity often takes place at these irregular surface sites, which offers a suitable environment for special bonding situations with reaction intermediates [30].

Reactions in which the catalytic activity also depends on the structure of the metal nanoparticle are termed structure sensitive reactions. A reaction can be considered to be structure sensitive if the rate of the reaction depends on the of the catalyst particles size [31], [32]. With a change in particle size, the catalyst particle's composition with respect to the availability of surface sites that are present is changed. This is illustrated in Figure 1.5 with different Wulff-constructed nanoparticles with a size varying from 0.6 to 8 nm. For these Wulff-constructed particles the surface energy is minimized as such that the high energy surfaces contribute a smaller fraction to the whole surface whereas the lowest energy surfaces contribute a larger fraction [30]. The larger particles thus inherently have more flat, low energy surfaces, which are called terraces, while the smaller particles

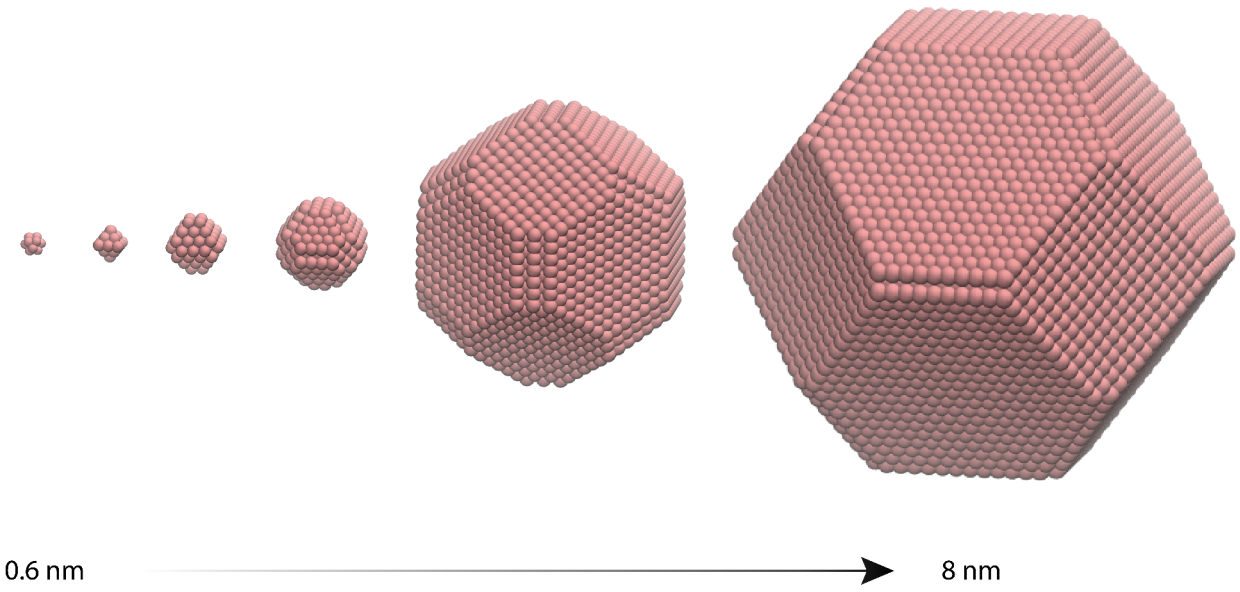

Figure 1.5: Wulff constructed nanoparticles in the size range of 0.6-8 nm.

contain more higher energy corners and stepped edges. A different surface can result in a different reaction rate, because of the difference in interaction between chemisorbed species and the various surface sites in the metal nanoparticle. The total reaction rate will be the sum of the individual reaction rates over the various surface sites, which is indicated by Equation 1.10 [33].

$$r_{total} = N_{terrace} \times r_{terrace} + N_{edge} \times r_{edge} + N_{corner} \times r_{corner} + N_{step} \times r_{step} \tag{1.10}$$

N_x is the number of surface atoms from a specific surface structure and r_x is the reaction rate on that specific surface structure.

Structure sensitivity can be divided into three main classes on the basis of the relation between the Turn Over Number (TON) and the catalyst particle size [32], which is shown in Figure 1.6. The first class shows no difference in reaction rate. The rate-limiting step for these reactions is the recombination of two adsorbates [32]. This TON-size dependency is mostly seen for example in the hydrogenation of alkyl intermediates. The behavior in the second class is typically seen for the activation of π-bonds, such as the dissociation of C=O which is preferred at a particular geometry where five or six metal atoms are arranged in such a way that a step site is created [33]. Here the

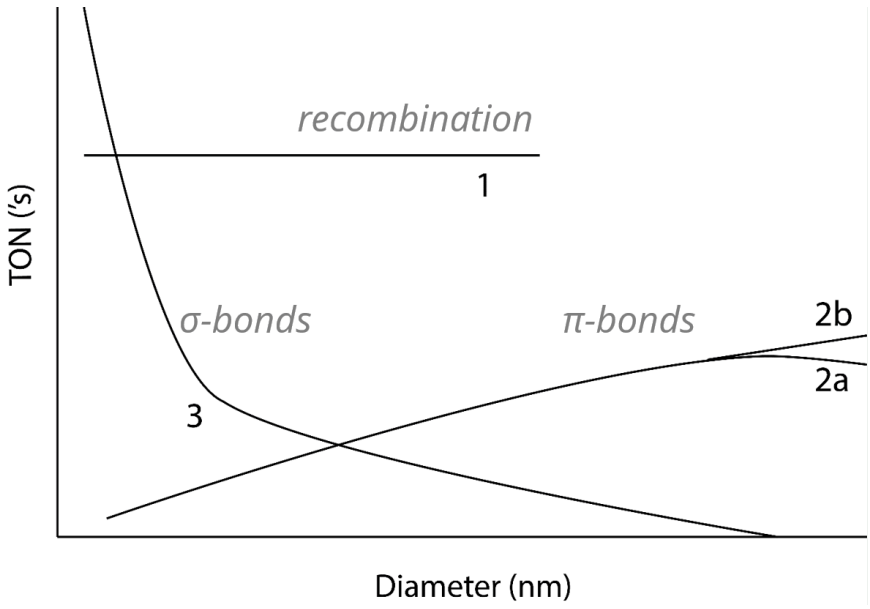

Figure 1.6: Three classes of structure sensitivity. Adapted from R.A. van Santen (2008) [32].

rate may show a maximum (2a) or may uniformly decline (2b) with a decrease in particle size [32]. In the third class, the reaction rate increases with a decrease in particle size, which is known to be true for the activation of a σ-bond [32]. For example the dissociative adsorption of CH_4 where a C-H bond is cleaved typically over a single surface metal atom [33].

Insights in the structure sensitivity of a particular reaction can be used to optimize the catalyst particle size to obtain a more efficient catalytic system. An example can be given for the adsorption of N_2 on Ni, Pt and Pd surfaces, which was studied by Hardeveld et al. [34]. They found that the adsorption of N_2 occurred on what they termed "B_5-sites", which are catalyst surface sites where an adsorbed molecule would have 5 contact points on the catalyst. They also found that the adsorption of N_2 depends on the size of the catalyst, which had to have a diameter between 15-70 Å. These two factors - the presence of B_5-sites and a specific diameter of the catalyst - are related by the physical probability to occur. For instance, when the catalysts are smaller than 15 Å, the catalysts are physically not able to form a significant amount of B_5-sites. When the catalyst is larger than 70 Å, the surface can arrange in such a way that no B_5-sites needs to be present and an almost spherical shape is maintained. Thus in perfectly Wulff constructed particles, B_5-sites can only occur when the catalyst has a diameter within the range of 15-70 Å [34].

Even though catalytic particles under reaction conditions are not likely to have perfect Wulff constructed shapes, it still illustrates the importance of particle size and the presence of different surface facets on activity of structure sensitive reactions.

2 Model

2.1 Status Quo

Recent research performed in our group has shown that CO_2 hydrogenation over well-defined SiO_2-supported nickel catalysts, ranging from 1 to 7 nm, is in fact a structure sensitive reaction [35]. Operando transmission Fourier transform infrared (FT-IR) spectroscopy was used to relate methanation activity to the occurrence and evolution of reaction intermediates. The reaction was tested using different conditions: 200 °C, 300 °C and 400 °C, and 1 bar, 5 bar, 10 bar and 20 bar. The influence of Ni mean particle size on TOF and activity corrected for the amount of nickel atoms at 400 °C, 1 bar is depicted in Figure 2.1a and 2.1b respectively. The highest TOF that was detected was found at 400 °C at 20 bar with catalyst size around 2.5 nm. All measurements showed a dependency of surface normalized activity related to particle size. This proves that the reaction is structure sensitive.

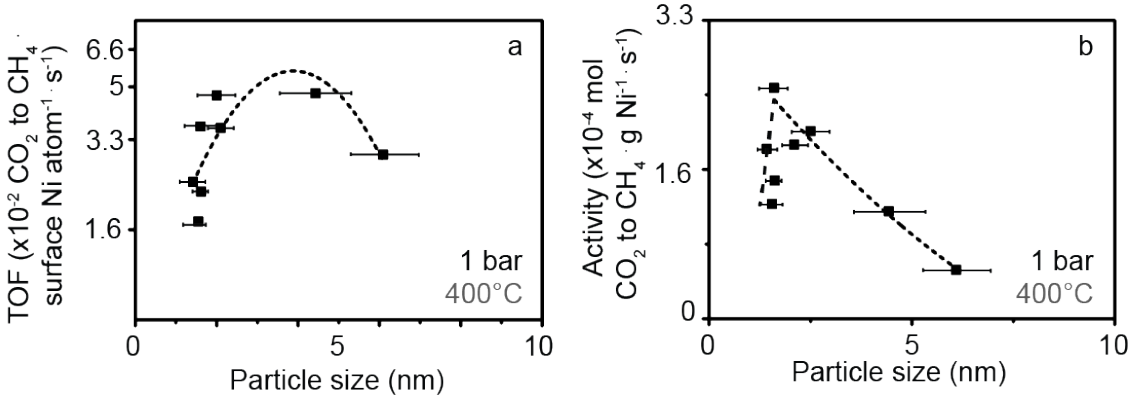

Figure 2.1: Particle size-activity relationships [35]. (a) The influence of Ni mean particle size on activity normalized to the Ni loading (400 °C, H_2/CO_2=4, 1 bar). Average TOF errors were found to be ±0.6%, and thus activity error bars lie within data markers. (b) The influence of Ni mean particle size on the TOF (400 °C, H_2/CO_2=4, 1 bar, assuming hemispherical particles and ten surface atoms per square nanometer).

Furthermore, relative amounts of different reaction intermediates could be observed using FT-IR-spectra. Three main reaction intermediates could be detected, namely CO*, gaseous CO and HCOO*. The formation of CO* and HCOO* originates from two different reaction mechanisms, the direct CO dissociation and a hydrogen assisted CO dissociation respectively. CO* was detected

in at least two binding modes. In one mode the carbon is attached to a single nickel atom, and in the other, a more strong metal-C bond, the carbon is bound to three nickel atoms. Interestingly, the catalyst with the highest activity in CO_2 hydrogenation has the largest relative amount of CO* adsorbed on a single nickel atom [35]. It was thus concluded that the rate-determining step relates to the ease with which CO* can be hydrogenated and, as a consequence, the availability of H* on adjacent sites to hydrogenate CO* [35].

The main product formed for each catalyst size is methane. The product selectivity of the smallest and largest nickel catalyst under study is depicted in Figure 2.2. For the catalyst of 1.8 nm (based on HAADF-STEM measurements) the formation of gaseous CO is up to 10 %. Besides CO and CH_4, also ethane and other C_{2+} products are formed. These C_{2+} compounds are considered to be alcohol or higher hydrocarbons. Interestingly no methanol was detected.

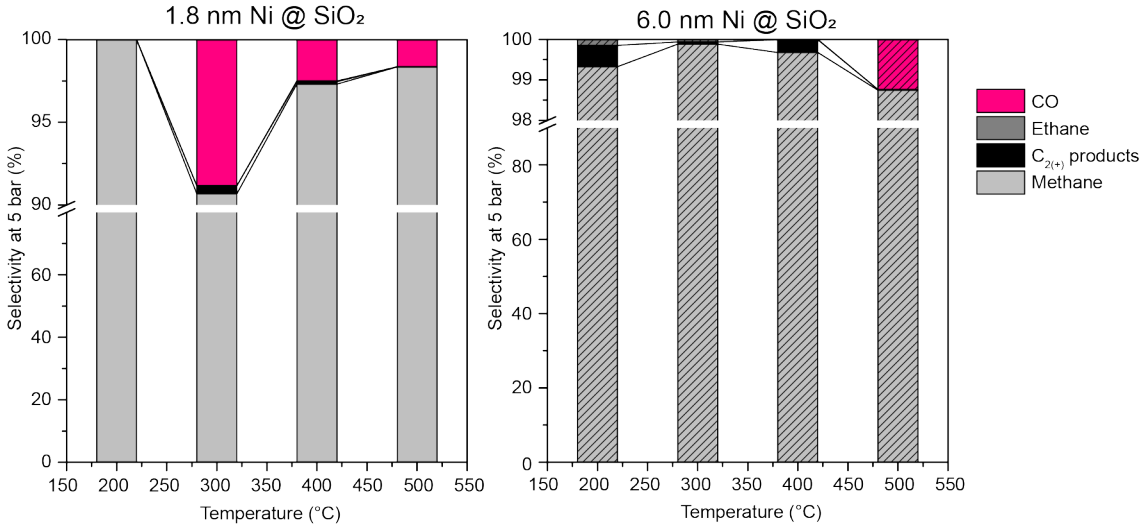

Figure 2.2: Product selectivity of CO_2 hydrogenation.

Thus, from experiments we learned that CO_2 hydrogenation is a structure sensitive reaction and that at least two reaction mechanisms are actively taking place. The rate determining step is most likely based on the ease in which CO* is hydrogenated and on the amount of available H* on adjacent sites. Finally with CO_2 hydrogenation over nickel catalyst the main product is methane, however gaseous CO, ethane and other C_{2+} products are formed as well. The ratio of different products that are formed depend on catalyst size, which means that the product selectivity is also

structure sensitive phenomenon.

To gain a more thorough insight in the underlying mechanisms of the structure sensitive CO_2 hydrogenation reaction over nickel catalysts, we use DFT calculations to address the following questions:

1. Can the formation of the reaction intermediates $HCOO^*$ and CO^* as well as the formation of gaseous CO be explained?

2. What is the predominant reaction mechanism and which surface facet is the most ideal in CO_2 hydrogenation towards methane?

3. How is this reaction structure sensitive? Which reaction steps are energetically most demanding?

4. Which reaction path is responsible for the formation of the C-C coupled species like ethanol and ethane?

5. What is the reason that ethanol might be formed, but no methanol was detected?

2.2 Possible Reaction Pathways

Before proceeding with DFT calculations, we need to have an overview of possible reaction pathways to convert CO_2 into CH_4. This overview is depicted in Figure 2.3, where the lines in color represents the main reaction paths while the gray and black lines represent possible interlinks between these main paths. H_2 dissociation and intermediates associated to H_2O evolution are not included in this picture. Based on the experimental results discussed in Section 2.1 ($HCOO^*$ and CO^* detected in FT-IR), we know that there are at least two reaction pathways to be active in CO_2 hydrogenation over nickel catalysts. The middle path, shown in pale pink in Figure 2.3, represents the direct, carbide mechanism. Here the oxygen atoms are dissociated first from $CO_2{}^*$, after which C^* is hydrogenated towards methane. For CO_2 dissociation, H-assisted pathways need to be taken into account, because studies [36], [37] have shown that the activation energy for direct CO dissociation be reduced by co-adsorption of hydrogen. The supposed reason for this is that the insertion of

hydrogen in CO* reduces the electron density in the CO π-bond, thereby weakening this bond. Two possible H-assisted mechanisms for CO_2 hydrogenation towards methane can be perceived. The first is shown in the bottom-path in Figure 2.3. This represents the hydrogen-assisted dissociation via formate species, which we term here the formate pathway. In this mechanism CO_2* is first hydrogenated to HCOO* after which an oxygen is removed. Subsequently HCO* can be either hydrogenated to H_xCO* or the second oxygen dissociates. When the second oxygen is removed, the hydrogenation steps for H_xC* are identical to the direct carbide mechanism. The second hydrogen-assisted reaction mechanism proceeds via alcohol intermediates shown as the top pathway, the alcohol pathway, in Figure 2.3. In this mechanism CO_2* is hydrogenated to COOH*, then the first oxygen is removed, after which COH* remains. In the subsequent steps COH* can either be hydrogenated toward H_xCOH* or the OH* group dissociates after which the remaining intermediate H_xC* can then further be hydrogenated via the carbide mechanism.

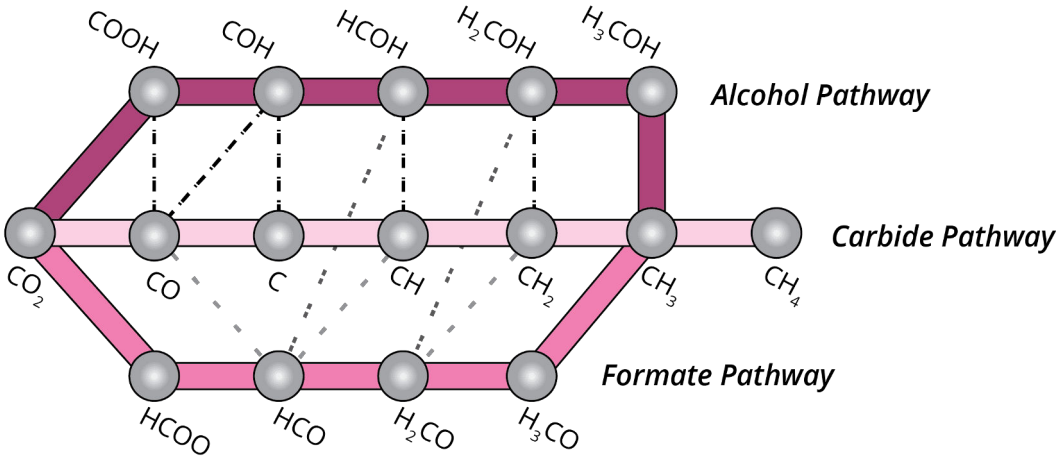

Figure 2.3: Overview of possible reaction paths in CO_2 hydrogenation over nickel catalysts. Direct dissociation (carbide pathway) in pale pink, hydrogen assisted dissociation via formate species (formate pathway) in violet and via alcohol intermediates (alcohol pathway) in dark purple. Interlinks between the three reaction paths are given in gray and black.

The fact that alcohol intermediates were not detected with IR-spectroscopy does not necessarily mean that these species are not formed. It is possible that these intermediates are more reactive and therefore do not take part of the rate determining steps and are thus not detected on the surface. The calculation of this reaction path can potentially provide insights in the formation of ethanol.

2.3 Simulation Approach

As discussed in Section 1.5 metal particles (on various supports) are composed of flat terraces, edges, corners, kinks and stepped surfaces. The topology of such a catalytic metal surface depends on many factors like particle size and reaction conditions, such as temperature, pressure, surface coverage and reaction species.

In order to study the structure sensitivity of CO_2 hydrogenation over nickel catalysts, four periodic slab models, two terraces and two stepped surfaces, were chosen to be representative for the catalytic surface of nanoparticles in the size range of 1 to 10 nm. A schematic representation of the four facets is given in Figure 2.4. The upper two facets are terraces, which were modeled using the Ni(111) and the Ni(100) termination of fcc Ni in a 7 layer 3x3 super-cell with periodic boundary conditions. The coordination number (CN) of the surface nickel atoms are 9 and 8 for Ni(111) and Ni(100) respectively. Adsorption sites on Ni(111) are bridge (B), threefold fcc (T_f), threefold hcp (T_h) and top (Ni) sites. Ni(100) has bridge (B), fourfold (F) and top (Ni) adsorption sites. The two lowest facets in Figure 2.4 are the stepped surfaces. These are modeled with a Ni(110) and Ni(211) termination of fcc Ni in a 4 layer 4x4 super-cell and a 4 layer 3x6 super-cell respectively. Periodic boundary conditions were applied. For Ni(110) the termination generates two top adsorption sites, one on the step edge (T_1), the other on the lower edge (T_2), a bridge (B) site, a fcc (T_f) and a hcp (T_h) threefold site. The CN's are 7 and 11 for the step- and lower edge respectively. The adsorption sites on Ni(211) include one fourfold (F) site, three top sites on the step (T_1), upper (T_2) and lower (T_3) edge, two three-fold fcc sites (T_f^1), (T_f^2), two three-fold hcp sites (T_h^1), (T_h^2) and three bridge sites (B_1), (B_2) and (B_3). The three CN's are 7, 10 and 9 for the step-, lower- and upper edge respectively.

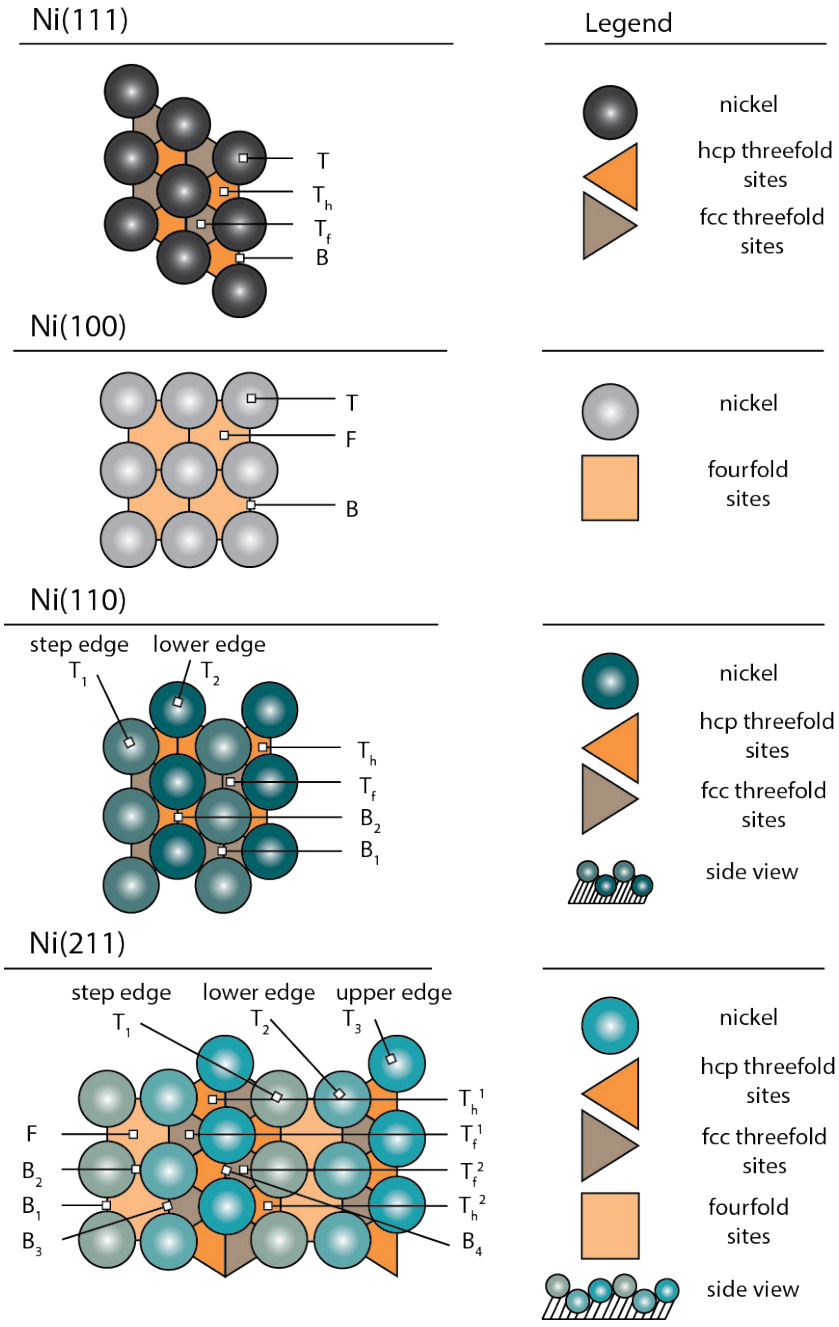

Figure 2.4: Schematic representation of the facets Ni(111), Ni(100), Ni(110) and Ni(211). Adsorption sites on Ni(111) include top (T) sites, bridge (B) sites, three-fold fcc (T_f) and three-fold hcp (T_h) sites. For the surface atoms of Ni(111) the coordination number (CN) is 9. Ni(100) gives top (T), bridge (B) and fourfold (F) adsorption sites, CN=8. Ni(110) has two top sites (T_1), (T_2), two threefold sites (T_h), (T_f) and a bridge site, CN=7 for the step edge, CN=11 for the lower edge. Ni(211) has three top sites (T_1), (T_2), (T_3), two threefold-fcc sites (T_f^1), (T_f^2), two threefold-hcp sites (T_h^1), (T_h^2), fourfold sites (F), four bridge adsorption sites (B_1), (B_2), (B_3), (B_4), for the step edge CN=7, lower edge CN=10, upper edge CN=9.

2.4 Computational details

All DFT calculations in this work were performed using the Vienna Ab-initio Simulation Package (VASP) [38], [39] with the projector-augmented wave (PAW) method [40], [41]. The Perdew-Becke-Ernzerhof (PBE) exchange-correlation functional was used [42]. The bulk lattice constant of nickel in its face-centered cubic crystal structure was optimized, yielding a value of 3.521 Å, which corresponds well to the documented bulk lattice constant of 3.524 Å [43]. The four nickel facets were modeled with this optimized Ni-Ni distance using periodic boundary conditions. The periodic slab models are discussed in Section 2.3. Relaxation was allowed for all atoms. The kinetic energy cutoff for the plane wave basis set was 300 eV. Monkhorst-Pack mesh k-points of (5x5x1) for Ni(111), Ni(100) and Ni(110) and (3x3x1) for Ni(211) was used. Each slab was applied with 10 Å vacuum perpendicular to the surface between the layers, in order to prevent interaction of intermediates due to translation of the super-cell in the z-direction. Dipole-dipole interactions between super-cells are avoided by adsorption on both sides of the exposed surface retaining a center of inversion. An energy criterion was used for the ionic convergence using the conjugate gradient algorithm. Geometries were converged to 10^{-4} eV and electronic convergence was set at 10^{-5} eV. For the gas-phase calculations of CO_2, CO, H_2 and H_2O, a Γ centered grid for k-point sampling was used. The molecules were placed at the center of a 10x10x10 Å unit cell. A Gaussian smearing with a width of 0.00002 eV was used for electron smearing. The reactions paths discussed in Section 2.2 are calculated by the nudged elastic band (NEB) as implemented in VASP [44]. A frequency analysis was performed to confirm that all transition geometries were in a first-order saddle point on the potential energy surface. The Hessian matrix was constructed using a finite displacement approach with a step size of 0.02 Å for displacement of individual atoms along each Cartesian coordinate. These frequencies were used to determine the zero-point energy (ZPE) correction to the energy of the geometries of the initial-, transition- and final-states.

3 VASP - Theory and Application

The following chapter presents a brief introduction in fundamental concepts of quantum chemistry and density functional theory. The simulation program used in this project is also shortly discussed.

3.1 Fundamental Principles in Quantum Chemistry

Computational modeling can be used as an aid in the interpretation of experimental data. The predictive aspect of computational modeling becomes increasingly substantial, as models are becoming increasingly better representations of reality, and computers became faster.

In order to predict interactions between molecules, atoms and electrons quantum mechanics is needed. The basic formula in quantum mechanics to study the dynamics of an atomic system is the time-independent, non-relativistic Schrödinger equation, shown in Equation 3.1:

$$\hat{H}\psi_i(\vec{x_1}, \vec{x_2}, ..., \vec{x_N}, \vec{R_1}, \vec{R_2}, ..., \vec{R_M}) = E_i\psi_i(\vec{x_1}, \vec{x_2}, ..., \vec{x_N}, \vec{R_1}, \vec{R_2}, ..., \vec{R_M}) \tag{3.1}$$

where $\hat{H}$ is the Hamiltonian operator for a molecular system which consists of M nuclei and N electrons which are described by the position vectors $\vec{R_A}$ and $\vec{r_i}$. $\psi_i(\vec{x_1}, \vec{x_2}, ..., \vec{x_N}, \vec{R_1}, \vec{R_2}, ..., \vec{R_M})$ stands for the wavefunction of the i'th state of the system, which depends on the 3N spatial coordinates $\vec{r_i}$, and the N spin coordinates $\{s_i\}$ of the electrons, which are collectively termed $\{x_i\}$ and the 3M spatial coordinates of the nuclei, $\{R_I\}$. The wavefunction contains all information that can possibly be known about the quantum system at hand, so from this wavefunction we can derive properties of the system. Finally, E_i is the numerical value of the energy of the state described by ψ_i [45].

In order to solve the Schrödinger equation for a certain molecular system, first the Hamiltonian operator needs to be specified. In general, $\hat{H}$ consists of two other operators as shown in Equation 3.2 [45]. The first operator represents the kinetic energy, the second represents the potential energy of the system, $\hat{T}$ and $\hat{V}$ respectively.

$$\hat{H} = \hat{T} + \hat{V} \tag{3.2}$$

The Schrödinger equation, Equation 3.1, with the Hamiltonian from Equation 3.2 can be used to

calculate the quantum mechanical energy of a system in order to predict the UV/Vis spectrum of a molecule or the vibrational spectrum of the ground state of a system. Another valuable application is that it can be used to predict the thermodynamics of a certain reaction by calculating the ground state energies of all molecules involved. This means that it is possible to calculate the effect of different catalytic surfaces for a certain reaction or elementary reaction step, which is valuable for this research project.

However, there is a problem unraveling properties of microscopic systems consisting of a large number *interacting* particles (a number somewhere between 2 and infinity), also termed as the many-body problem. This makes it is very difficult to exactly construct the Hamiltonian operator from Equation 3.2.

In order to construct the kinetic energy operator $\hat{T}$ we can pretend that the nuclei and electrons are classical particles, and use the classical formula for kinetic energy. We can also look at at classical mechanics to find an expression for the potential energy operator $\hat{V}$. For two equally charged particles, there is Coulomb repulsion, while a positive and negative charged particle will attract each other. However, because of the many-body problem, it is very hard to construct a full potential energy operator for a system consisting of more than 2 interacting particles.

If we pretend that the electrons do not interact with each other (meaning that attractive and repulsive forces are not mutually correlated), we can reduce the many body problem to a sum of two-body problems. The operators that need to be constructed are shown in Equation 3.3. A full expression for a system with N electrons and M nuclei is given in Equation 3.4.

$$\hat{H} = \hat{T_e} + \hat{T_N} + \hat{V_{eN}} + \hat{V_{ee}} + \hat{V_{NN}} \tag{3.3}$$

$$\hat{H} = -\frac{1}{2}\sum_{i=1}^{N}\nabla_i^2 - \frac{1}{2}\sum_{A=1}^{M}\frac{1}{M_A}\nabla_A^2 - \sum_{i=1}^{N}\sum_{A=1}^{M}\frac{Z_A}{r_{iA}} + \sum_{i=1}^{N}\sum_{j>i}^{N}\frac{1}{r_{ij}} + \sum_{A=1}^{M}\sum_{B>A}^{M}\frac{Z_A Z_B}{R_{AB}} \tag{3.4}$$

M_A from Equation 3.4 is the ratio of the mass of nucleus A to the mass of an electron, Z_A is the atomic number of nucleus A. The laplacian operators ∇_i^2 and ∇_A^2 are defined as a sum of differential operators with respect to the coordinates of the i'th electron and the A'th nucleus [46]. The first

and the second term is the operator for the kinetic energy of the electrons and the nuclei, $\hat{T}_e$ and $\hat{T_N}$ respectively. The third term represents the Coulomb attraction between the electrons and the nuclei, $\hat{V_e}N$, the fourth and the fifth terms are the electrostatic repulsions between electrons and nuclei, $\hat{V_{ee}}$ and $\hat{V_{NN}}$ respectively. However, as mentioned above, this representation does not contain a potential energy operator that covers correlation. This means that the Hamiltonian defined in Equation 3.4 is actually a simplification of the 'real' problem.

Thus, as a consequence of the many-body problem, for all molecules containing more than one electron the Hamiltonian (and therefore the Schrödinger equation) needs to be approximated. This leads to the ultimate goal of most quantum chemical approaches, which is to find the best approximate-solutions of the time-independent, non-relativistic Schrödinger equation.

3.1.1 Basic Approximations

In order to make good approximations of the solutions of the Schrödinger equation, many approximations and mathematical constructions are needed. However, there are three basic approximations that are used in Density Functional Theory (DFT) methods.

The first approximation is called the Born Oppenheimer approximation, which only takes the motion of the electrons into account. The nuclei are much heavier than the electrons, and thus its kinetic energy is significantly smaller than that of the electrons. In the case of a Born Oppenheimer approximation, the electrons move in a constant electrostatic field which is produced by the nuclei. With these conditions the kinetic energy term of the nuclei in the Schrödinger equation is canceled out and the electrostatic repulsion between the nuclei can be treated as a constant. This results in a so-called electronic Hamiltonian [45]:

$$\hat{H} = -\frac{1}{2}\sum_{i=1}^{N}\nabla_i^2 - \sum_{i=1}^{N}\sum_{A=1}^{M}\frac{Z_A}{r_{iA}} + \sum_{i=1}^{N}\sum_{j>i}^{N}\frac{1}{r_{ij}} \tag{3.5}$$

The second approximation is to leave electron-electron interactions out of the equation. This interaction is, as explained in the previous section, not solvable. The result of this approximation is that for every electron in the system a 1-electron Schrödinger equation can be solved, which translates into hydrogen-like wave functions and energies. The Pauli exclusion principle, which

states that two electrons can't ever have the same quantum number, determines the lowest set of energy levels for a set of electrons [45].

The third approximation is the assumption that the real wave function is a linear combination of atomic orbitals, that is a linear combination of known wave-functions. Because of the non-interaction electron model, the many electron wave function is a product of linear atomic orbitals, and because of the anti-symmetry rule in the Pauli exclusion principle, the wave function can be described by a Slater Determinant, shown in Equation 3.6.

$$\Psi_N = \frac{1}{\sqrt{N!}} \begin{vmatrix} \chi_1(\vec{x}_1) & \chi_2(\vec{x}_1) & \cdots & \chi_N(\vec{x}_1) \\ \chi_1(\vec{x}_2) & \chi_2(\vec{x}_2) & \cdots & \chi_N(\vec{x}_2) \\ \vdots & \vdots & \ddots & \vdots \\ \chi_1(\vec{x}_N) & \chi_2(\vec{x}_N) & \cdots & \chi_N(\vec{x}_N) \end{vmatrix} \tag{3.6}$$

N is the total number of electrons, the factor $\frac{1}{\sqrt{N!}}$ ensures that the wavefunction is normalized, the one-electron functions $\chi_i(\vec{x}_i)$, called spin orbitals, are composed of a spatial orbital $\varphi(\vec{r})$ and one of the two spin functions, α or β [47]. Slater Determinants are a very important tool in quantum mechanics, because it satisfies the antisymmetry rule (i.e., change of sign when 2 independent electronic coordinates are interchanged $\Psi(\chi_1,\chi_2) = -\Psi(\chi_2,\chi_1)$) as well as the Pauli exclusion principle (e.g. two electrons with spin α in one orbital; $\chi_1=\chi_2$, then $\Psi(\chi_1,\chi_2) = 0$) [48]. Comprehensive, in depth explanations about Slater Determinants can be found in textbooks on matrix algebra and quantum chemistry [47], [48].

3.2 Ab Initio Methods

The term *ab initio* is Latin for *from the beginning*. This name is given to computational methods that are directly derived from theoretical principles with no inclusion of experimental data. The approximations made in ab initio calculations are usually of a mathematical kind, such as using an approximate solution to a differential equation.

3.2.1 The Hartree-Fock Approximation

One of the first methodologies to solve the Schrödinger equation for a system with more than one electron was calculated using the Hartree-Fock method. The wave function of the ground state is approximated using a Slater Determinant. Subsequently, the best approximate wave function is found using a variational calculation where the spin orbitals, $\chi_i(\vec{x}_i)$, in the Slater Determinant are systematically varied while they remain orthogonal, until the electronic minimum E_0 is reached [49].

The primary approximation in the Hartree-Fock method is the so called central field approximation. With this the electron-electron repulsion term is integrated, which results in an average effect of the repulsion between electrons [50]. This means that the explicit repulsive interaction is not taken into account, which causes the major drawback in the Hartree-Fock method. The problem can be clearly explained using Figure 3.1, where two arrangements of electrons around a nucleus of an atom are depicted. Within the Hartree-Fock method, these two arrangements are considered to have the same probability to exist, because only the distance between the electrons and the nucleus, r_1 and r_2, are taken into account but not the distance between the two electrons, defined by ϑ_1 and ϑ_2. However, this is physically not true, because the movement of one electron does have an electrostatic effect on the other electron. In other words, the Hartree-Fock method does not describe electron correlation well.

To solve this problem different methods were developed which incorporated the electron correlation. In the Møller-Plesset perturbation theory, correlation is added as a perturbation from the Hartree-Fock wave function [50]. An other method is the Configuration Interaction. In this method a multiple-determinant wave function is constructed starting from the Slater Determinant obtained by the Hartree-Fock method. New determinants are made by promoting electrons from the occupied to unoccupied orbitals [50].

Although the post-Hartree-Fock methods provide a very accurate description of the electronic structure, they are computationally very demanding. These methods all rely on the many-body wave function which depends on 3N spatial variables together with a spin variable, where N is the number of electrons. This limits the applicability of these methods to relatively small systems [49].

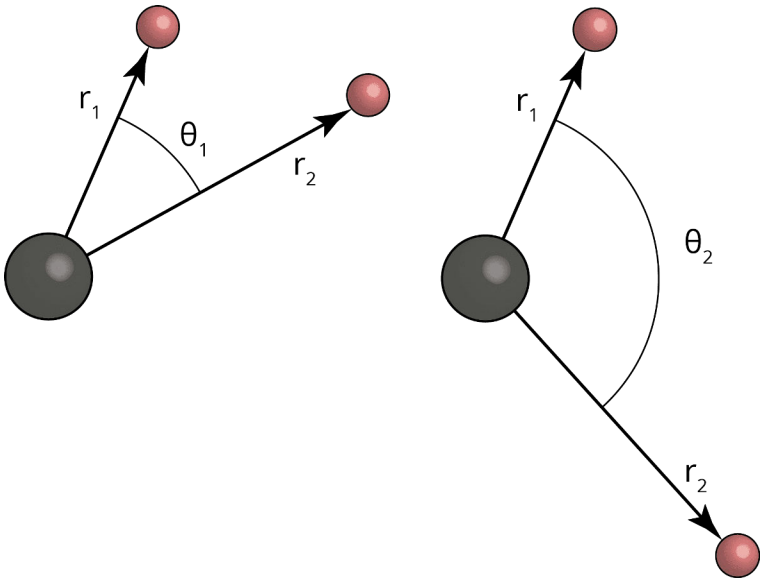

Figure 3.1: Two arrangements of electrons (pink) around the nucleus (gray) of an atom, having the same probability within the Hartree-Fock method.

3.2.2 Density Functional Theory

The central idea in DFT is that there is a relationship between the total electronic energy and the overall electronic density of the system [47]. This was emphasized by Hohenberg and Kohn in 1964, when they showed [51] that the ground-state energy and other properties of a system were uniquely defined by the electron density. In other words, the energy of a system is a unique functional of the electron density.

The usage of electron density instead of the wave function has a great advantage on the dimensionality in calculating large systems. While the many-body wave function depends on 3N+1 variables, where N is the number of electrons, in DFT the dimensions are always 3, because the density is always 3 dimensional regardless the number of electrons. This makes DFT a very useful model for calculations on big molecular systems like catalysts.

In DFT the energy functional is written as a sum of two terms [47]:

$$E[\rho(r)] = \int V_{ext}(r)\rho(r)dr + F[\rho(r)] \tag{3.7}$$

where the first term represents the interaction of the electrons with an external potential, such as

the nuclei of the system. The second term holds the sum of the kinetic energy of the electrons as well as the electron-electron interactions. The problem was that there is not an exact description to obtain $\rho(r)$ and $F[\rho(r)]$, because the electron-electron interaction cannot be solved as discussed in Section 3.1. Kohn and Sham suggested that $F[\rho(r)]$ should be approximated as the sum of three terms [47]:

$$F[\rho(r)] = E_{KE}[\rho(r)] + E_H[\rho(r)] + E_{EX}[\rho(r)] \tag{3.8}$$

where $E_{KE}[\rho(r)]$ is the kinetic energy of non-interacting electrons with the same electron density, $\rho(r)$, as the real system. $E_H[\rho(r)]$ is the electrostatic energy between 2 electrons and $E_{EX}[\rho(r)]$ is the exchange correlation energy term. The idea of the Kohn-Sham approximation is that the non-interacting particle model can be used to calculate the larger part of the total kinetic energy of the system. With this we can formally define the exchange-correlation energy as:

$$E_{EX}[\rho_r] = E_{kin,true}[\rho(r)] - E_{KE}[\rho(r)] + E_{ee}[\rho(r)] - E_H[\rho(r)] \tag{3.9}$$

and total energy using the Kohn-Sham approach can thus be described as follows:

$$E[\rho(r)] = \int V_{ext}(r)\rho(r)dr + E_{KE}[\rho(r)] + E_H[\rho(r)] + E_{EX}[\rho(r)] \tag{3.10}$$

This is still a full formulation of the total energy of the system. However, since the exchange correlation term is not known exactly, approximations are needed to calculate this term.

The simplest approximation is called the Local Density Approximation (LDA), which is based upon a model called the uniform electron gas, in which the electron density is constant throughout all space [47]. Using the LDA, the electron density at each position in the system is pretended to be homogeneous with the corresponding electron density at that point. This means that the non-homogeneous electron density of a chemical system is treated locally as being homogeneous. The LDA therefore oversimplifies the electron density, which causes for example inadequate bond distances and strengths in molecular calculations [50].

A more complex functional in DFT is the gradient-corrected functional, which depend on the

gradient of the density at each point in space and not just on its value. Thus, generalized gradient approximation (GGA) are semi-local and comprised from corrections to the LDA [49]. The PBE-GGA is used for all calculations discussed in this thesis.

3.3 DFT Implementation - VASP

In this work catalytic properties are investigated using large extended periodic surfaces, which are simulated using periodic boundary conditions. The simulated surfaces are constructed from a unit cell that is periodically repeated throughout all space by means of rigid translation along its lattice vectors.

Plane waves are used as a DFT basis-set in order to find an expression for the Kohn-Sham-equation Eq. 3.10, which is considered to be the most obvious basis-set to use for calculations on periodic systems [47]. Using this basis-set, each orbital wave function is expressed as a linear combination of plane waves.

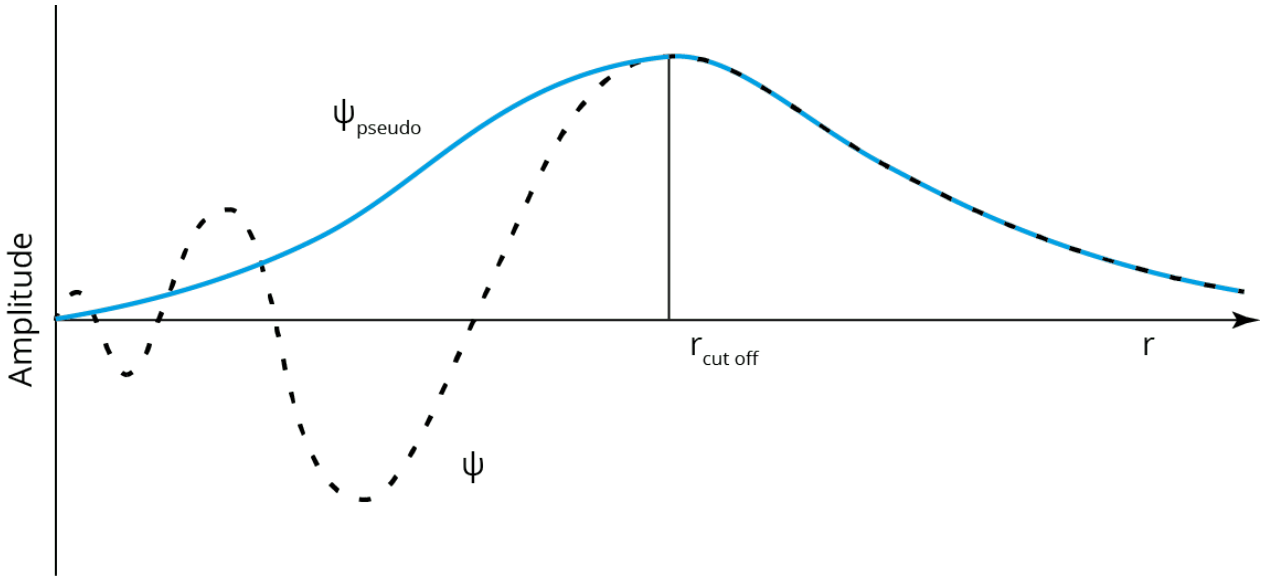

Figure 3.2: Schematic representation of a pseudo-potential in blue. The real and the pseudo wave function match above a certain cutoff radius.

A large amount of plane waves are needed to properly model wave functions that are located close to atomic nuclei [47]. Thus core electrons would require excessive computational effort to

model its properties. However, valance electrons are much more important in typical chemical properties than core electrons. In order to prevent that the least important electrons get the largest part of the computational effort, the potential in the core regions is replaced by a pseudo-potential, which is schematically illustrated in Figure 3.2. A pseudo-potential is a potential that gives wave functions with the same shape as the real wave function outside the core region, but it replaces the wave function inside the core region with a smooth function [47]. This reduces the number of plane waves and computational effort drastically. The pseudo-potential used throughout this work is the Projector Augmented Wave method [40], [41].

In order to perform DFT calculations with the Vienna Ab initio Simulation Package (VASP) four input files are needed. The POTCAR file contains the pseudo-potential of each element while the POSCAR file includes the Cartesian coordinates of the atoms that need to be modeled in a calculation. The KPOINTS file contains k-point coordinates (i.e., sampling points in the reciprocal space) and weights in order to create a k-point grid. This grid is needed because a plane wave basis-set and periodic boundary conditions are used [52]. The INCAR file is a central input file in VASP, where many parameters can be managed and altered. With this file one can determine what will be calculated in which way. A comprehensive explanation of many parameters and tags used in VASP can be found in the online VASP manual [53].

4 Stability of Reaction Intermediates

4.1 Stable Geometries

The first step in the search for the energetically most favorable reaction path of CO_2 hydrogenation towards methane over nickel using DFT is to calculate the stability of any relevant intermediate in different geometries on different adsorption sites on the four nickel facets. The adsorption sites are shown in the schematic representation of the facets in Figure 2.4. Each intermediate found in the carbide, formate and alcohol pathways indicated in Figure 2.2, is 'placed' on the different adsorption sites by adding specific Cartesian coordinates in the POSCAR file of each facet. By varying the Cartesian coordinates of an intermediate, one can vary both the geometry and orientation of the intermediate itself as well as the mutual orientation of the intermediate with respect to the surface. An example of this process is visualized in Figure 4.1 where the intermediate $HCOH^*$ is placed on Ni(110) in two different geometries, on the left the OH-bond is pointing down towards the surface while on the right it is facing upwards. This means that the OH-bond is rotated with respect to the CH-bond, resulting in an altered geometry of $HCOH^*$. The position where $HCOH^*$ is adsorbed on the surface is also changed, from a B_1 site on the left to a T_1T_1 site on the right.

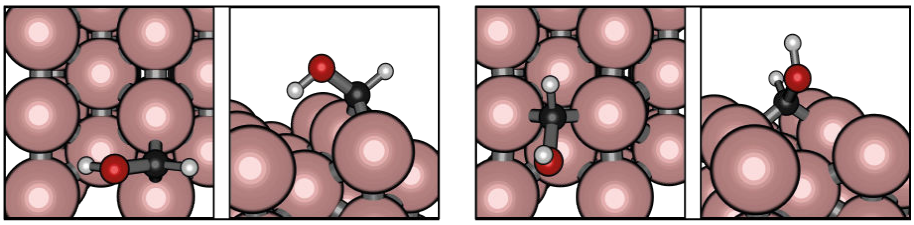

Figure 4.1: Example of a visualized result for the addition of $HCOH^*$ to a Ni(110) slab using different Cartesian coordinates for the intermediate. On the left the intermediate is positioned at a B_1 site and the OH bond is pointing downwards. In the right picture the orientation of $HCOH^*$ with respect to the surface is changed by rotating the complete intermediate with 90° and by a change in position on the plane parallel to the surface. The geometry of $HCOH^*$ itself is altered by a rotation of the CO-bond with 180° so that the OH-bond is now pointing away from the surface.

The generated POSCAR files for each intermediate in various orientations on the four different nickel facets were optimized using a conjugate gradient algorithm, which is implemented in VASP. The pictorial results of the stable geometries of intermediates bound to the facets are depicted

in Appendix A, where the geometries are grouped per nickel facet per intermediate in order of decreasing adsorption energy. Adsorption energy, E_{ads}, is a measure of strength of the adsorbate-substrate interaction. E_{ads} is defined as follows:

$$E_{ads} = E_{xy^*} - E_{facet} - E_{xy} \tag{4.1}$$

where E_{xy^*} is the total energy of XY^* adsorbed on a nickel facet, E_{facet} and E_{xy} are the total energies of the nickel facet and free adsorbate XY, respectively. With this definition, the more negative values for E_{ads} reflect to a stronger interaction of adsorbed species with the surface [54]. Tables 4.1, 4.2, 4.3 and 4.4 list the *most* stable adsorption sites for each surface intermediate on the four different nickel facets. The adsorption energies of *each* stable intermediate depicted in Appendix A are listed in Appendix B. The first column contains the adsorbate, in the second column the adsorption sites of the atoms from the intermediate that are bound to the nickel facet are indicated with the character of the corresponding adsorption site, as shown in Figure 2.4. The geometry of the adsorbate with respect to the surface is further explained in the third column, by indicating which atoms are bound to the adsorption sites. The adsorption energies are given in column four.

Some general trends to be observed considering the sites in which the different intermediates are bound to the nickel surface in the most stable configuration. Highly coordinatively unsaturated adsorbates, like C^*, favor 3- and 4- fold coordination sites, whereas more saturated adsorbates, such as $CH_3{}^*$, are preferentially located in bridge and top positions of the surface. These trends are also observed in other studies [55] and can be explained by the extent to which the valance shell of the atoms that are bound to the surface are filled. An intermediate such as $CH_3{}^*$ is more saturated in terms of coordination compared to C^*. Therefore the valance shell of the carbon atom of $CH_3{}^*$ is more filled, than in the case of C^*, which makes $CH_3{}^*$ more stable than C^*. The more stable the intermediate the less interaction with the nickel surface is needed.

The intermediates from the carbide mechanism all bind to the surface in a monodentate fashion. For both the formate and alcohol intermediates there are cases in which the most stable geometry is bound in a bidentate state. The majority of the intermediates in this study were found to bind

to the surface via the carbon atom. In the case of $HCOO^*$ and H_3CO^*, the intermediates were found most stable when bound to the surface only with their oxygen atoms. H_2O^* was found to be most stable on a top position. Only for Ni(211) one other stable geometry was found, where H_2O^* is attached to a B_1 adsorption site. For CH_3OH^* no stable geometries were found on any nickel facet.

In the search for stable geometries of molecular adsorbed hydrogen many attempts resulted in dissociated hydrogen adatoms, however a few stable configurations for H_2 were found (see Appendix A). The geometries that resulted in a negative E_{ads} value, i.e., a strong interaction between $H_2{}^*$ and the nickel facet, were obtained if the H-H bond was orientated parallel to the nickel surface and positioned on a top site of a nickel atom. These orientations were found to be stable for each nickel facet except for Ni(111). As can be seen in Table 4.2-4.4 the adsorption energies for $H_2{}^*$ parallel to the metal surface and on a top site range from -28.5 to -62.4 kJ/mol, depending on the nickel facet. Other geometries where molecular $H_2{}^*$ was found to be stable in proximity of the nickel facet are the cases in which $H_2{}^*$ is directed perpendicular to the facet. The adsorption energies were significantly higher compared to the parallel orientations, that is 11.3 kJ/mol for Ni(111) and for the other facets E_{ads} ranges from -0.3 to 1.5 kJ/mol. Also the distance of $H_2{}^*$ to the nickel surface is much larger for the perpendicular compared to the parallel orientation. From this we might assume that the perpendicular orientation of $H_2{}^*$ is an intermediate or pre-adsorption state. This means that an energetically favorable adsorption of molecular $H_2{}^*$ has the restrictions of being parallel to the surface and above a nickel top site. However, there are much more possibilities for molecular hydrogen to be in proximity of a nickel surface facet, which means that there is a significant probability that dissociative adsorption of H_2 will take place. This assumption is in agreement with literature, where it was found that H_2 dissociation on Ni(110) has no energetic barrier and on Ni(111) a small barrier of 1.4 kJ/mol was reported [56].

Table 4.1: Energetically most favorable adsorption site for each intermediate on Ni(111).

Ni(111)			
Adsorbate	**Site**	**Geometry**	**E_{Ads} in kJ/mol**
COO	B, T, T	C bridged, O^1 top, O^2 top	24.3
CO	T_h	C threefold hcp	-178.6
CH	T_f	C threefold fcc	-603.3
CH_2	T_f	C threefold fcc	-454.2
CH_3	T_f	C threefold fcc	-238.3
HCOO	T, T	O^1 top, O^2 top	-277.3
HCO	B, T	C bridged, O top	-201.2
		CO bond over T_f	
H_2CO	T_f, T	C threefold fcc, O top	-57.7
H_3CO	T_h	O threefold hcp	-218.0
COOH	B, T	C bridged, O top	-210.9
		CO bond over T_f	
COH	T_h	C threefold hcp	-410.5
HCOH	B	C bridged	-270.8
H_2COH	B, T	C bridged, O top	-146.7
		CO bond over T_f	
C	T_h	C threefold hcp	-773.8
O	T_f	O threefold fcc	-692.4
H	T_f	H threefold fcc	-360.9
H_2O	T	O top	-22.5
OH	T_f	O threefold fcc	-364.9
H_2	B	H_2 vertical above bridge	11.3

Table 4.2: Energetically most favorable adsorption site for each intermediate on Ni(100).

Ni(100)			
Adsorbate	**Site**	**Geometry**	**E_{Ads} in kJ/mol**
COO	B, T, T	C bridged, O^1 top, O^2 top	-16.3
		span a corner	
CO	F	C fourfold	-174.8
CH	F	C fourfold	-667.6
CH_2	B	C bridged	-436.8
CH_3	B	C bridged	-233.8
HCOO	T, T	O^1 top, O^2 top	-293.8
		diagonal over fourfold	
HCO	B, B	C bridged, O bridged	-264.6
		over fourfold	
H_2CO	B, B	C bridged, O bridged	-127.9
		over fourfold	
H_3CO	F	O fourfold	-251.9
COOH	T, T	C top, O top	-232.9
		above bridge	
COH	F	C fourfold	-447.5
HCOH	B	C bridged	-285.2
H_2COH	B	C bridged	-159.4
C	F	C fourfold	-909.35
O	F	C fourfold	-724.18
H	F	C fourfold	-364.5
H_2O	T	O top	-31.1
OH	F	O fourfold	-388.4
H_2	T	H_2 horizontal above top	-28.5

Table 4.3: Energetically most favorable adsorption site for each intermediate on Ni(110).

Ni(110)			
Adsorbate	**Site**	**Geometry**	**E_{Ads} in kJ/mol**
COO	T_1, T_1, T_1	C top, O^1 top, O^2 top	-41.9
		step edge; span a corner	
CO	B_1	C bridged	-174.5
CH	$T_1 - T_1$	C top top	-613.7
		above lower edge	
CH_2	T_2	C top	-452.9
		lower edge	
CH_3	B_1	C bridged	-252.2
HCOO	T_1, T_1	O^1 top, O^2 top	-327.8
		above lower edge	
HCO	B_1, B_1	C bridged, O bridged	-239.6
		CO bond over lower edge	
H_2CO	B_1, B_1	C bridged, O bridged	-190.3
		CO bond over lower edge	
H_3CO	B_1	O bridged	-259.5
COOH	T_1, T_1	C top, O top	-248.1
		CO bond over lower edge	
COH	B_2	C bridged	-378.9
HCOH	B_1	C bridged	-317.3
H_2COH	T_1, T_1	C top, O top	-173.6
		CO bond over B_1	
C	B_2	C bridged	-836.1
O	T_f	O threefold fcc	-676.4
H	B_2	H bridged	-351.6
H_2O	T_1	O top	-38.5
OH	B_1	O bridged	-398.6
H_2	T_1	H_2 horizontal above top	-62.4

Table 4.4: Energetically most favorable adsorption site for each intermediate on Ni(211).

Ni(211)			
Adsorbate	**Site**	**Geometry**	**E_{Ads} in kJ/mol**
COO	B_1, T_1, T_1	C bridged, O^1 top, O^2 top	-39.1
		step edge	
CO	T_h^2	C threefold hcp	-186.7
CH	F	C fourfold	-634.2
CH_2	T_h^2	C threefold hcp	-467.8
CH_3	T_h^2	C threefold hcp	-265.6
HCOO	T_1, T_1	O^1 top, O^2 top	-340.6
		step edge	
HCO	T_f^1, B_1	C threefold fcc, O bridged	-248.2
H_2CO	T_f^{1*}, B_1	C threefold, O bridged	-90.3
		* C double bonded to the surface	
H_3CO	B_1	O bridged	-269.1
COOH	B_1, T_1	C bridged, O top	-257.0
		step edge	
COH	F	C fourfold	-415.6
HCOH	B_1	C bridged	-314.4
H_2COH	B_1	C bridged	-192.6
C	F	C fourfold	-874.1
O	T_h^2	O threefold hcp	-711.4
H	T_f^2	H threefold fcc	-363.7
H_2O	T_1	O top	-48.5
OH	B_1	O bridged	-415.0
H_2	T_1	H_2 horizontal above top	-38.9

Calculated adsorption energies were compared with values known from literature in order to facilitate comparison and to verify the validity of our model. To our best knowledge CO_2 hydrogenation towards methane has not yet been fully calculated for the nickel facets Ni(111), Ni(100), Ni(110) and Ni(211). However, several adsorption energies calculated with DFT have been found. In Table 4.5 the adsorption energies of several intermediates in CO_2 hydrogenation on different nickel facets are compared with values found in literature using various calculation codes and functionals (VASP & STATE & CASTEP and GGA-PBE & GGA-PW91). In spite of the different calculation methods, which makes quantitative comparison arbitrary, it does make qualitative comparison possible. Our calculated adsorption energies listed in Table 4.5 are in good agreement with values found in literature.

Table 4.5: Adsorption energies (E_{ads}, eV) of adsorption species involved in CO_2 methanation on Ni(111), Ni(100), Ni(110) and Ni(211) compared to values found in literature. Compared values correspond to same adsorption sites on the nickel facets.

	Ni(111)	Literature	**Ni(100)**	Literature	**Ni(110)**	Literature	**Ni(211)**	Literature
CO_2	0.25	0.26 [57]	-0.17	-0.14 [57]	-0.43	-0.42 [57]	-0.41	-0.42 [58]
CO	-1.85	-1.92 [59], -1.91 [57]	-1.81	-2.04 [57]	-1.81	-1.94 [57]	-1.93	
HCO	-2.09	-2.26 [59]	-2.74	-3.14 [60]	-2.48		-2.57	
COH	-4.25	-4.42 [61], 4.39 [59]	-4.64		-3.93		-4.31	
HCOO	-2.87	-3.02 [61]	-2.74		-3.40		-3.12	-3.07 [61]
H_2O	-0.23	-0.20 [62]	-0.32	-0.27 [62]	-0.40	-0.39 [62]	-0.50	

4.2 Chemisorption Energies

In the search for an energetic favorable reaction mechanism of CO_2 hydrogenation over nickel, comparison of energetic quantities between reaction intermediates and corresponding nickel facets is necessary. In this Section the stability of adsorbates which are stable both in gas phase as well as on the nickel facets are evaluated for CO_2 and CO. For this the chemisorption energy (the energy needed to adsorb an adsorbate from the gas phase onto the metal surface) was calculated using Equation 4.2. Notice that this equation is almost the same as Equation 4.1, however here it has been applied to our calculation methods.

$$\Delta E_{chem} = \frac{E_{2A-B^*} - E_{bare\,slab} - 2 \cdot E_{A-B(g)}}{2} \tag{4.2}$$

The first term, E_{2A-B^*}, is the total energy for the slab with the twofold chemisorbed adsorbate AB^* on the surface. Twofold adsorption was used to prevent dipole-dipole interaction between super-cells, see Section 2.4, consequently 2 chemisorption events are taking place in one calculation therefore the energy should be divided by 2. The second term, $E_{bare\,slab}$, is the total energy of the bare slab of the surface facet and the third term, $E_{A-B(g)}$, is the total energy of the adsorbate AB in gas phase. Therefore, a negative ΔE_{chem} corresponds to an exothermic chemisorption and a positive ΔE_{chem} refers to an endothermic chemisorption.

An adsorption event, in this case for $CO_{2(g)}$ and $H_{2(g)}$, is imperative for subsequent catalytic reactions. Here we will not zoom in onto the chemisorption energy of molecular $H_2{}^*$. The cases in which molecular hydrogen is adsorbed, are not representative as a pre-state for $H_2{}^*$ dissociation, since the greater part of the adsorption of $H_{2(g)}$ takes place via dissociative adsorption, as discussed in Section 4.1.

The results of $CO_{2(g)}$ chemisorption energies for each facet and different adsorption sites are shown in Figure 4.2. The geometries corresponding to the different chemisorption energies are depicted in Appendix A. For Ni(111) each stable geometry of $CO_2{}^*$ has an endothermic chemisorption energy, ranging from 24.3 to 35.5 kJ/mol. This is in accordance with values found in literature, 28.8 to 42.2 kJ/mol [63]. The stable geometries that were found for Ni(100) and Ni(110) all corresponded to an exothermic chemisorption energy; -16.3 and -38.9 kJ/mol respectively, which is close to the literature values of -13.44 [57] and -37.44 kJ/mol [63]. Depending on the position and geometry of $CO_2{}^*$ with respect to the surface, Ni(211) gave both exothermic and endothermic chemisorption values with the most endothermic and exothermic values of 10.3 and -39.1 kJ/mol respectively. From these results we conclude that $CO_{2(g)}$ chemisorption on nickel is a structure sensitive event and that Ni(111) is most likely not active in the chemisorption of $CO_{2(g)}$. This means that already

at the very first step in the catalytic hydrogenation of $CO_{2(g)}$, structure sensitivity plays a role as the interaction between $CO_2{}^*$ and the four different nickel facets vary significantly.

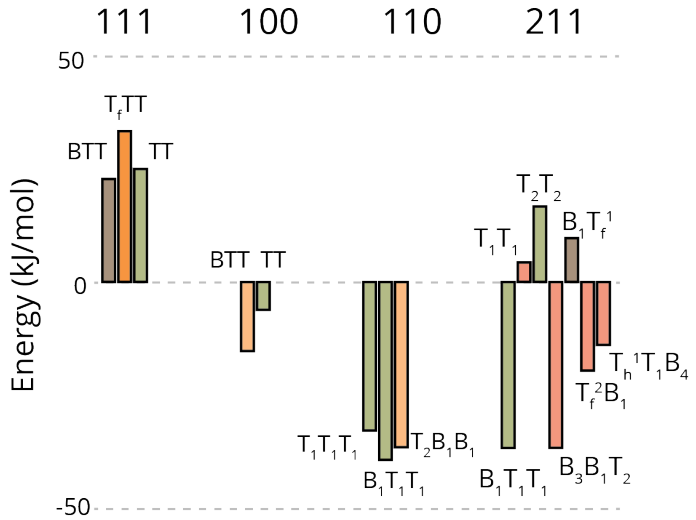

Figure 4.2: Chemisorption energies of $CO_2{}^*$ on Ni(111), Ni(100), Ni(110) and Ni(211). The characters next to the bars correspond to the adsorption site of the atoms C-O-O respectively. Corresponding geometries are depicted in Appendix A.

The chemisorption energy for CO^* was found to be exothermic for each nickel facet ranging from -145 to -180 kJ/mol, see Appendix B. From experimental studies it is known that gaseous CO is released during CO_2 hydrogenation over nickel catalysts, as discussed in Section 2.1. Depending on the thermal energy in the system, there are several prospects for CO^* adsorbed on the metal surface. There are several prospects for CO^* adsorbed on the metal surface if the thermal energy in the system is high enough. The first option is that CO^* may decompose into O^* and C^*. Secondly, CO^* may react with other surface species like H^* to form HCO^* for example. An other option is that CO^* can desorb from the surface by which it enters the gas phase.

In the latter case there will be an appreciable increase in kinetic energy, because $CO_{(g)}$ has besides vibrational degrees of freedom also rotational and translational degrees of freedom. An adsorbate in a stable geometry only has vibrational degrees of freedom. As a consequence, desorption of CO^* is entropically favorable. The rate constant for the desorption process can be assessed with the Arrhenius equation in Equation 4.3,

$$k_{des} = Ae^{\frac{-E_a^{des}}{RT}} \tag{4.3}$$

where k_{des} is the rate constant of the desorption, E_a^{des} is the activation energy for desorption, A is a frequency factor which includes the frequency of collisions and their orientation.

The average adsorption energy of the stable geometries of CO* on the various nickel facets given in Appendix B is -165.7 kJ/mol. This indicates that an energy of 165.7 kJ/mol needs to be surmounted in order for CO* to go into the gas-phase. As a side note, it is important to realize that the activation barrier for CO* desorption does not necessarily have to be equal to the adsorption energy of CO*. To get a rough estimate of the reaction rate for CO desorption under reaction conditions we use the Arrhenius equation (Equation 4.3) with T = 673 K, E_{act} = 165700 J/mol, R = 8.314 J/mol*K and A $\approx \frac{k_b * T}{h} \approx 1.4*10^{13}$. This results in a calculated reaction constant of 1.9 s^{-1}. This means that CO* can indeed be desorbed from the surface. However, it does not fully explain that up to 10 % $CO_{(g)}$ was detected. If we would use activation energies (instead of the adsorption energy of CO*) of 126 to 155 kJ/mol, which were found in literature for CO desorption from Ni(111) [27], the reaction rate would range from 13 to 2325 s^{-1}, which makes CO* desorption more significant then calculated above. From this we can conclude that gaseous CO formed during the reaction originates from CO* desorption.

4.3 Relative Stability

In Section 4.2 chemisorption energies of a few adsorbates were discussed. In the search for a favorable reaction path in CO_2 hydrogenation it is not useful to calculate the chemisorption energies for each reaction intermediate by which the stability of the intermediates are related to their stability in gas-phase. With chemical intuition alone it can be rationalized that both atomic carbon (C*) and an alkyl intermediate, CH_2* for example, are much less stable in gas-phase than CO_2. Consequently these intermediates would have a significantly higher chemisorption energy. However, we are interested in the stability of each intermediate with respect to the different surface facets. Therefore relative stability, defined in Equation 4.4, can be used in order to analyze the relative stabilities of each surface intermediate [55].

$$\Delta E_{stab,rel} = \frac{E_{ads^*} - x(E_{C^*}) - y(E_{H^*}) - z(E_{O^*}) + (x + y + z - 1) \times E_{facet}}{2} \tag{4.4}$$

The first term in Equation 4.4, $E_{stab,rel}$, is the relative stability of the adsorbate, E_{ads^*} is the electronic energy of the adsorbate on the surface, E_{C^*}, E_{H^*} and E_{O^*} are the electronic energies for C^*, H^* and O^* in their most stable configurations on the nickel facet, E_{facet} is the electronic energy of an empty nickel slab and x, y, z represent the number of atoms of C, H or O to construct the adsorbate. This value needs to be divided by 2, because again, for each calculation twofold adsorption was applied to prevent dipole-dipole interactions between super-cells, see Section 2.4. Lateral interactions between adsorbates were ignored.

Stability plots (also known as Ivonian plots), were constructed for each nickel facet in order to analyze the relative stabilities of the reaction intermediates. In Figure 4.3 and 4.4 the stability plots for terraces and stepped nickel facets respectively are shown. In these plots the mutual stability can be read out for all surface reaction intermediates that are able to be formed based on the three reaction pathways shown in Figure 2.3. Different colors are used for adsorbates originating from the different reaction pathways. Intermediates located closer to the center of the plot are more stable on the surface than those located more to the outside.

Looking at the stability plots for the four facets, it is remarkable that for Ni(100) a much larger energy scale is needed than for the three other facets. The reason for this is the significant difference in adsorption energy for the atomic species C^* and O^*, E_{ads} listed in Table 4.1-4.4. Both atomic carbon and oxygen are most stable on the 100 nickel facet in a fourfold site. In order to form an intermediate consisting out of more than one atom, an energetically very stable adsorption is canceled out which can not be compensated by bond formation. Consequently the recombination of atomic adsorbates to form CO^* for example is not favorable with respect to the atomic species since the formed adsorbate only occupies one instead of two fourfold sites. This explains why all intermediates on Ni(100) are located above the zero-energy line and also illustrates that these plots should mainly be used to interpret intra-facet.

The intermediates for the alcohol pathway, depicted on in the quadrant on the right side of the

plots, are least stable on each nickel facet. While the formation of both $COOH^*$ and COH^* are within the energy range of the other two pathways, progression via this mechanism towards more hydrogenated alcohol intermediates are increasingly endothermic and therefore not likely to occur. This can indicate that the alcohol mechanism is not likely to be most active in CO_2 hydrogenation over nickel.

The energy range of the stability for intermediates corresponding to the formate and the carbide pathway are comparable on Ni(111), Ni(100) and Ni(110). For Ni(211) the intermediates of the carbide pathway are significantly more stable than the intermediates of the higher hydrogenated species of the formate pathway. Therefore we can hypothesize that the formation of CH_4 might go via the formate as well as the carbide pathway. However, for Ni(211) the intermediates needed towards the formation of $CH_3{}^*$ are more stable using the carbide pathway only.

Looking at the plots for Ni(111) and Ni(110) both CO^* and $HCOO^*$ are located more to the center, which indicates that they are very stable on these facets. Because of this stability it can be explained that both of these intermediates were detected with IR-spectroscopy under reaction conditions (see Section 2.1). For each nickel facet both C^* and CH^* are much more stable than $CH_2{}^*$ and $CH_3{}^*$. This is most pronounced on Ni(100) where the energy difference is approximately 100 kJ/mol. From this we can assume that C^* and CH^* are the dominant CH_x^* adsorbates under reaction conditions, which was also seen for Rh(211) [55].

In short, based on the stability plots it can be hypothesized that the alcohol pathway is not very likely to be active in the CO_2 hydrogenation over nickel. The intermediates with a high surface coverage under reaction conditions are expected to be CO^*, C^* and CH^*, which also are components that are necessary for the formation of ethane and ethanol by C-C coupling and CO-insertion respectively.

Thus, it is interesting to look at the stabilities of C-C coupled intermediates, which will be covered in Section 4.4. The unfavorable alcohol pathway also indicates that the formation of ethanol probably originates form a CO insertion mechanism with the most predominant CH_x^* species: C^* and/or CH^*. From this we can explain the detection of ethanol and the absence of methanol during the reaction (see Section 2.1). The production of methanol via the alcohol pathway does not occur,

because the corresponding intermediates are not stable enough.

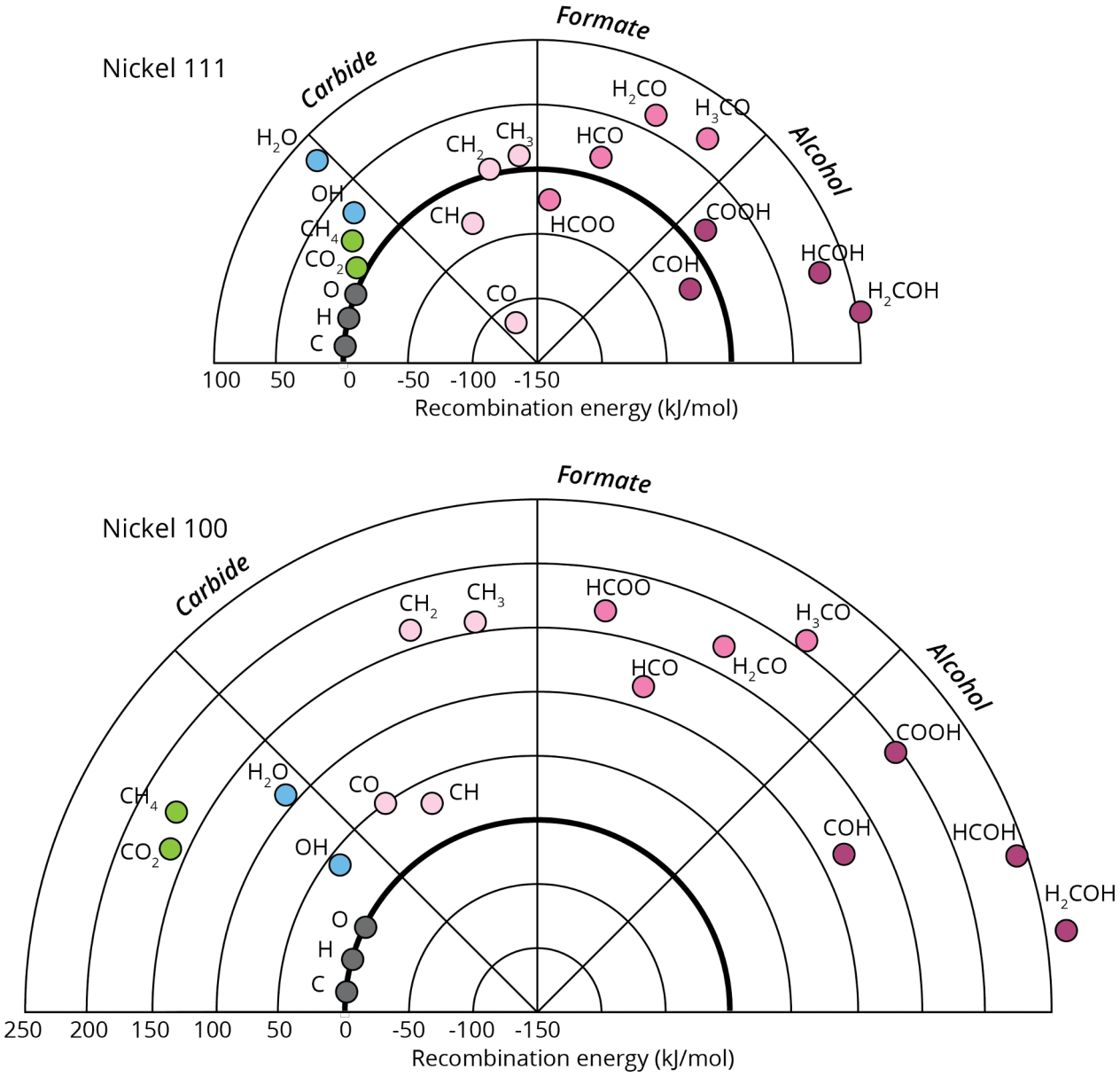

Figure 4.3: Stability plots of all surface reaction intermediates relevant to CO_2 hydrogenation on Ni(111), upper, and Ni(100), lowest, terraces. The energy (kJ/mol) of each compound is calculated using the reference energy of atomic carbon, oxygen and hydrogen adsorbed on the surface in their most stable configuration. Intermediates located closer to the center are more stable. The different colors indicate the type of component (i.e., pale pink for carbide-, violet for formate- and dark purple for alcohol-intermediates (see Fig.2.3), gray for atomic species, blue for intermediates that involve formation of H_2O and green for CO_2).

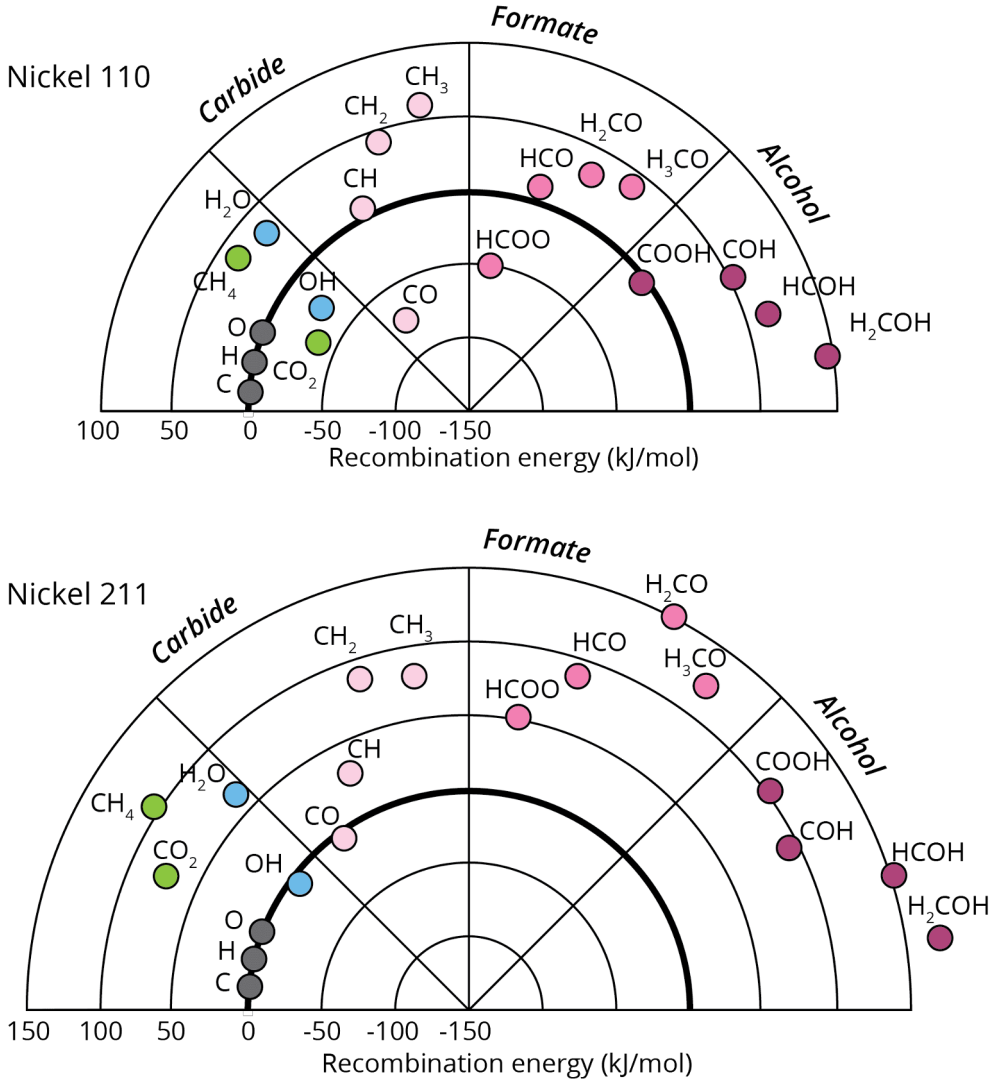

Figure 4.4: Stability plots of all surface reaction intermediates relevant to CO_2 hydrogenation on Ni(110), upper, and Ni(211), lowest, stepped facets. The energy (kJ/mol) of each compound is calculated using the reference energy of atomic carbon, oxygen and hydrogen adsorbed on the surface in their most stable configuration. Intermediates located closer to the center are more stable. The different colors indicate the type of component (i.e., pale pink for carbide-, violet for formate- and dark purple for alcohol-intermediates (see Fig.2.3), gray for atomic species, blue for intermediates that involve formation of H_2O and green for CO_2).

4.4 Relative Stability of C-C Coupled Species

The main product formed during CO_2 hydrogenation over nickel is methane, however also ethane and other C_{2+} products are formed (see Section 2.1). Based on the stability plots for the interme-

diates of the three main reaction pathways (carbide, formate and alcohol pathway), we concluded that there is most likely a relatively high surface coverage of CO^*, C^* and CH^* during the progression of the reaction. As a consequence, there is a possibility that these surface intermediates combine to form a C-C bond. In order to verify if this is energetically favorable, a stability plot of various C-C coupled intermediates was constructed, which is shown in Figure 4.5. The stability of the intermediates are related to the two components needed to form a C-C bond, that is atomic carbon, CO^* and CH_x^*.

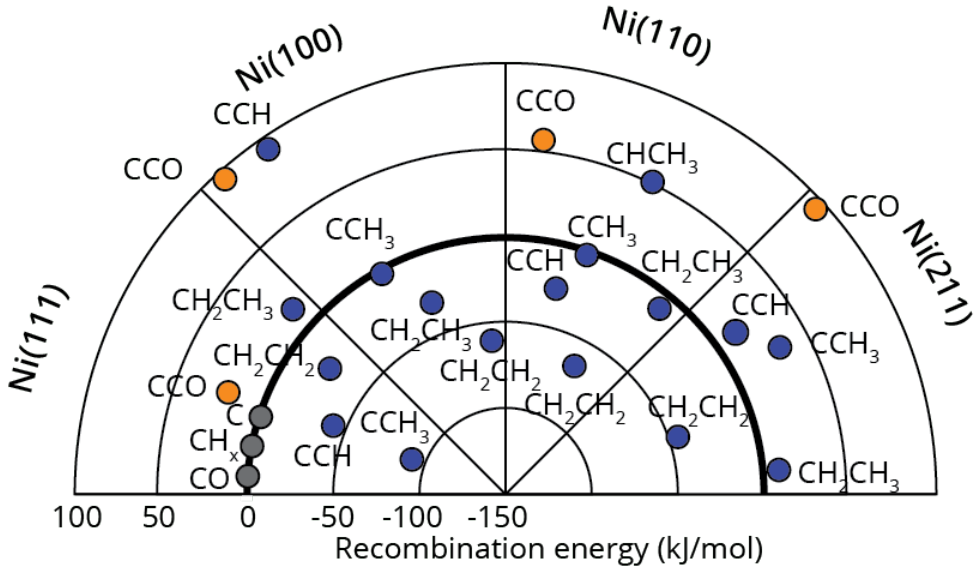

Figure 4.5: Stability plots of CH_x-CH_y^* and C-CO^* coupled adsorbates in blue and orange respectively on Ni(111), Ni(100), Ni(110) and Ni(211). The energy (kJ/mol) of each compound is calculated using the reference energy of the two intermediates needed to form a C-C coupled intermediate, that is C^*, CH_x^* and CO^* adsorbed on the surface in their most stable configuration. The reference species are indicated in gray. Intermediates located closer to the center are more stable.

From this plot it is immediately clear that on each nickel facet roughly each CH_x-CH_y^* intermediate is located towards the center of the plot. This indicates that these species are stable on each nickel facet and therefore the formation of ethane may be independent of the surface facet.

The CO-inserted intermediate CCO^* is located more to the outside of the plot, especially on Ni(100) and Ni(211). Therefore the formation of C_{2+} hydrocarbons seem to be more facile than the formation of higher alcoholic species. This can explain that ethane was detected in a somewhat

larger amount, while a smaller fraction of alcohol and/or hydrocarbon C_{2+} products was detected.

Now we can explain that no methanol, but possibly a small amount of alcoholic C_{2+} products was detected (see Section 2.1). The formation of ethanol likely originates via a CO^* insertion mechanism with an available CH_x^* intermediate. The production of methanol via the alcohol pathway does not occur because the corresponding intermediates are not stable enough. Another route for the formation of methanol could be the hydrogenation of H_3CO^* from the formate pathway. Based on the stability plots it seems to be possible that H_3CO^* is formed and as a consequence the hydrogenation to methanol as well. In order explain the absence of methanol, information about the energy barriers are necessary, which is provided in Chapter 5.

5 Energy Barriers

In the previous Chapter we used relative stabilities to analyze the stability of relevant intermediates in CO_2 hydrogenation towards methane over nickel catalysts. Based on these analysis we tentatively concluded that both the carbide as well as the formate pathway are likely to be favorable during the reaction. The alcohol pathway would not be likely to be active in the reaction of interest, because these intermediates are the least stable compared to the intermediates of the two other mechanisms. However, no energy barriers were taken into account. The hight of these barriers are very important in the course of a catalytic reaction. For example, using the Arrhenius Equation 4.3, it can be calculated that the reaction rate will be approximately 6x as fast when the activation barrier is lowered with 10 kJ/mol at 673 K. Therefore, in order to unravel the most favorable reaction mechanism it is extremely important to calculate the energy barriers as well. For this reason the alcohol pathway should not be discarded at this point in research.

5.1 NEB Calculations

The three reaction pathways all consist of multiple elementary reaction steps, that is a reaction in which one or more intermediates react to form a product in a single reaction step and a single transition state. In order to gain a more detailed overview of the three reaction pathways the transition state of each elementary reaction was calculated using the Nudged Elastic Band (NEB) Method [44]. The principle of this method is depicted in Figure 5.1. Starting with the NEB method equidistant geometry files (also called images) along the reaction coordinate are obtained via linear interpolation between the geometry files of the initial and final state of the elementary reaction. This interpolation is indicated with the dashed line, where the blue points represent the initial and the final state and each white point represents one image. With linear interpolation the images will not necessarily follow the route with the lowest energy. Therefore, for each geometry of the obtained images a relaxation is performed using a tangential spring to keep the images equidistant [44]. This force along the reaction path due to the applied spring is indicated with $F^k \parallel$. If this spring is not applied, the relaxations of the images would end up in either the initial or in the final state. Of the true forces that apply to the intermediate states between the initial and final state, only

the component normal to the reaction path is used, indicated with $F^r \perp$ [64]. After the relaxation the intermediate states are positioned on an energy profile going through a saddle point. The intermediate state located on this point (indicated in green) is the so-called transition state.

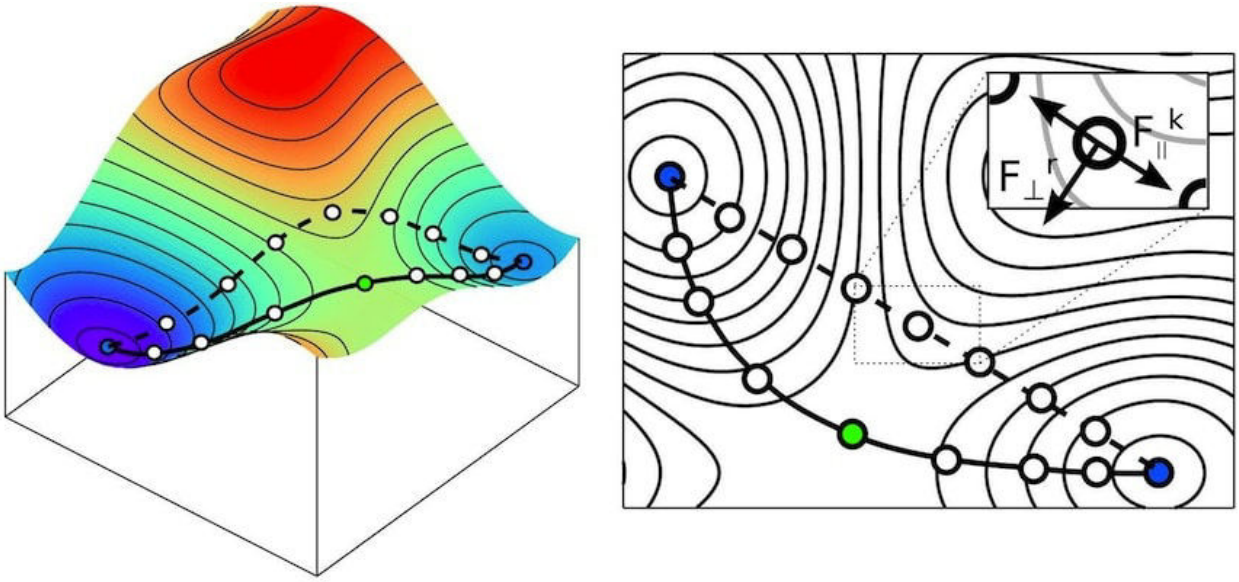

Figure 5.1: Principle of the NEB method. The blue dots represent the initial and final state, the white dots are the intermediate states and the dashed line shows the path corresponding to the linear interpolation. After applying the NEB method, the configurations are located along the minimum energy path, indicated with the continuous line. The green dot corresponds to the transition state, which is located at the saddle point. (From [64].)

The calculations were performed first with an interpolation of the initial and final state generating a somewhat broad density of images. This resulted in an approximation of the energy of the transition state. Subsequently, a finer resolution around the saddle point was obtained using a more dense image spacing. Next, a transition state optimization for the image closest to the saddle point was performed. Finally it was checked if the geometry of the transition state corresponded to a first-order saddle point on the potential energy surface using finite displacement method for a frequency analysis. If there are two imaginary frequencies (twofold adsorption, Section 2.4) on the reaction coordinate, the obtained transition state was considered valid. The calculated energy from the frequency analysis was used to perform a zero-point energy correction to the electronic energy of the transition state in order to obtain its ground state energy.

5.2 Energy Profiles

5.2.1 Main Pathways

The forward and backward energy barriers calculated for the elementary reaction steps are given in the form of a reaction network depicted in Figure 5.2. The first number, going from one intermediate to the next, is the forward activation energy (Ea_F). For example, the activation energy of the hydrogenation of C* on Ni(111) is 70 kJ/mol, and the backward activation energy (Ea_B) is 108 kJ/mol which is listed as the second number. The energy barriers are given with respect to the most stable adsorbed state for each intermediate. As a consequence, Ea_F contains the energy of the translation and/or rotation of the reactant intermediate from the most stable geometry toward the geometry of the initial state plus the energy to go from the initial to the transition state. Ea_B contains the energy needed to go from the most stable geometry of the intermediate formed to the geometry of the final state and the activation energy to go from the final to the transition state. The geometries of the initial, transition and final state of each elementary reaction step over the four different nickel facets are depicted in Appendix C. With the use of both the energy of intermediates in their most stable configuration and the hight of the energy barriers, potential energy diagrams were constructed for the three reaction pathways, see Figure 5.3.

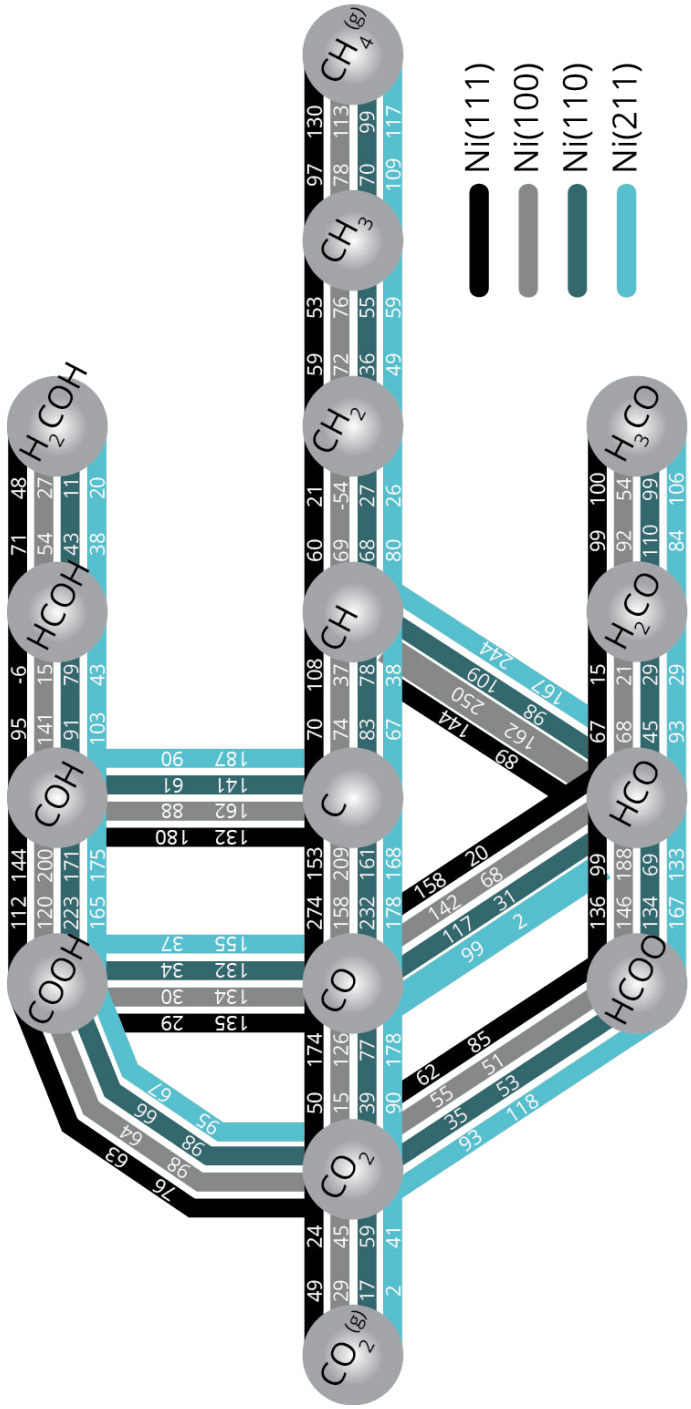

Figure 5.2: Reaction network of three main pathways in CO_2 hydrogenation over nickel. Forward and backward activation energies (kJ/mol) for the conversion of CO_2 to CH_4 on Ni(111), Ni(100), Ni(110) and Ni(211). The first number going from one intermediate to the next is the forward activation energy. For example, the activation energy of the hydrogenation of C* on Ni(111) is 70 kJ/mol, the backward activation energy is 108 kJ/mol.

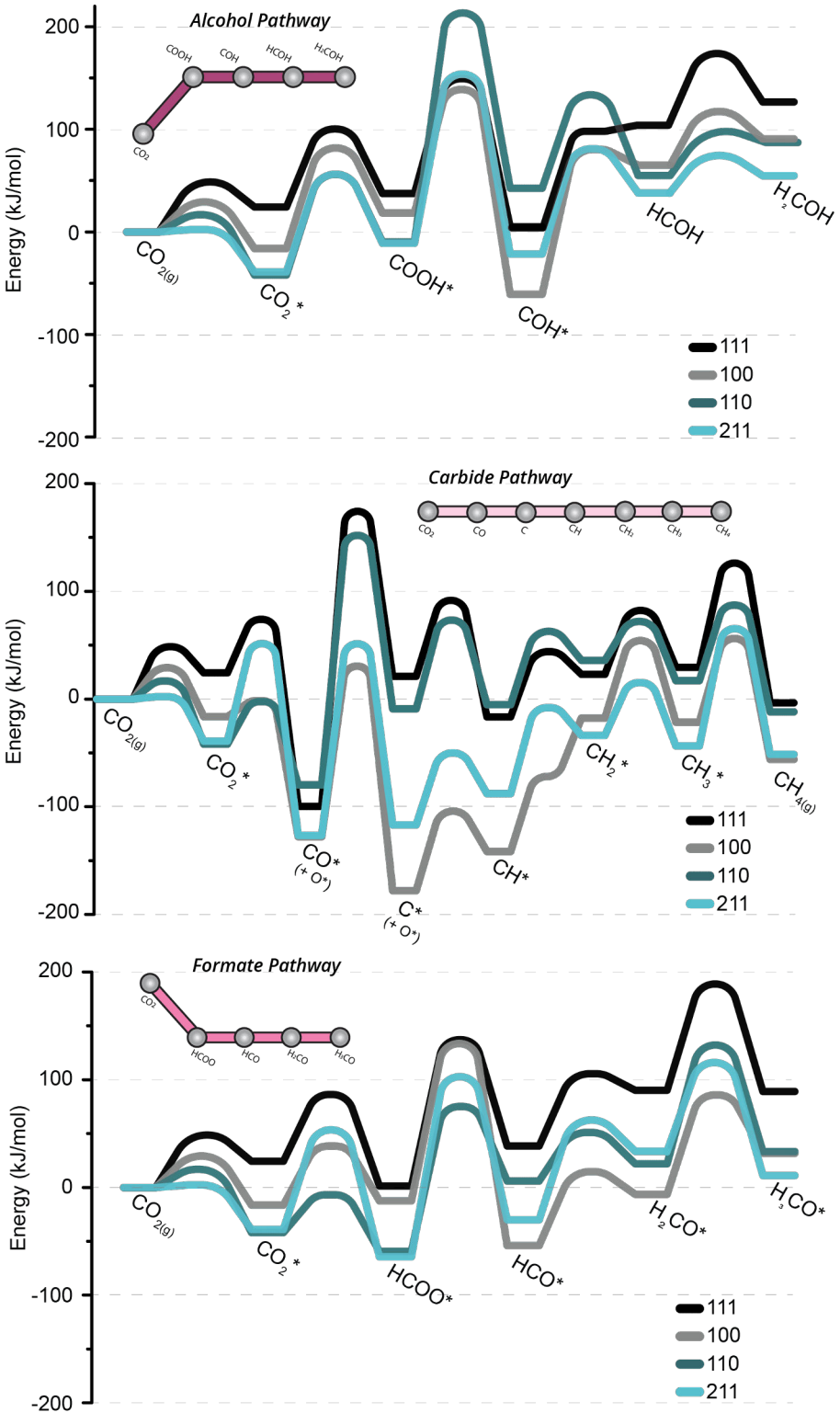

Figure 5.3: Energy profiles of the three main reaction pathways.

The calculated chemisorption energy for $CO_2{}^{(g)}$ was found to be most favorable for the stepped facets, as discussed in Section 4.2. Looking at the energy barriers shown in Figure 5.2 it is noticeable that the activation barrier to adsorb gaseous CO_2 on the nickel surface is the smallest on Ni(211) with 2 kJ/mol. This indicates that for the energetically lowest reaction path the first elementary reaction step is most favorable on Ni(211).

The energy profiles in Figure 5.3 show some aspects noteworthy to point out. Firstly, $CO_2{}^*$ is best activated when the carbide mechanism is used. A potential well, or liberation of energy, is necessary for a reaction to proceed and for the first elementary reaction in the carbide mechanism approximately 120 kJ/mol is released using Ni(111) or Ni(100), while on Ni(110) 40 kJ/mol is released and 90 kJ/mol on Ni(211). Via the formate mechanism 20 kJ/mol is released for the $CO_2{}^*$ activation using Ni(110) and Ni(211). The formation of the first alcohol intermediate is an endothermic reaction, which indicates that the reaction is not likely to start easily via this route.

The second thing to notice is the significant hight of the activation barrier to go from CO^* toward atomic carbon. We already know from the Fischer Tropsch reaction that CO^* dissociation is a rather difficult process [37]. For example on flat Ru(0001) the CO dissociation barrier was found to be up to 227 kJ/mol [37]. The energy barriers in our system range from 178 kJ/mol for Ni(211) to 273 kJ/mol for Ni(111), as can be read out from Figure 5.2. These energy barriers are comparable to the energy range for the activation barrier of CO^* desorption, see Section 4.2. To be specific, on Ni(111) and Ni(110) the activation energy for CO^* dissociation is higher than its desorption, while on Ni(100) and Ni(211) the inverse is true. This means that there is a competition between CO^* dissociation and desorption, which is not beneficial for the formation of methane.

For both the formate as well as the alcohol pathway the hydrogenation steps are endothermic. There is one exception, that is the hydrogenation of H_2CO^* on Ni(211). However, the formation of H_2CO is most likely not very facile, because the forward activation energy from HCO^* to H_2CO^* is 2-3 times higher than for its backward reaction. With this it is very likely that if H_2CO^* is formed it will be converted back to HCO^* really fast. Also the formation of H_2CO is an endothermic process. With this we can invalidate the suggestion made in Section 4.4, because also the formation of methanol via hydrogenation of H_3CO is not likely to occur. Thus any ethanol formed is formed via

CO-insertion. The hydrogenation steps in the carbide pathway are mainly endothermic, however the hydrogenation of C^* on Ni(111), $CH_2{}^*$ on Ni(110) and Ni(211) are exothermic. The final hydrogenation step of $CH_3{}^*$ to form methane is exothermic for each nickel facet.

Based on the energy profiles and the activation barriers of the elementary reaction steps, the rate limiting step in the carbide pathway is the CO^* dissociation. The hight of the activation barriers to convert CO^* either back to $CO_2{}^*$, further toward $COOH^*$ or HCO^* are 2 to 10 times higher than the barriers to form CO^* from $CO_2{}^*$. This means that it would take relatively longer to convert CO^* on the surface than to form it, which result in a relatively longer lifetime of CO^* on the surface. This is in accordance with IR-spectroscopy, where CO^* was detected (Section 2.1). For both the formate and the alcohol pathway the rate limiting step would be the removal of the first oxygen, from $HCOO^*$ and $COOH^*$ respectively. The forward activation barrier of $CO_2{}^*$ toward $HCOO^*$ is roughly 20 kJ/mol lower than its backward reaction. Adding to that the fact that in order to continue the formate mechanism the forward barrier is approximately 3 times higher than the barrier for the backward reaction to form $CO_2{}^*$ again, which means that also for the intermediate $HCOO^*$ the formation will be faster than the reaction that converts $HCOO^*$ again. With this we can explain that also $HCOO^*$ was detected with IR-spectroscopy (Section 2.1). Although the highest activation barrier in the alcohol mechanism is the formation COH^* from $COOH^*$, $COOH^*$ is not detected with IR-spectroscopy. The reason for this is that the forward activation barrier going from $CO_2{}^*$ to $COOH^*$ is higher than its backward barrier. Also the barrier for the intermediate route $COOH^*$ to CO^* is approximately 30 kJ/mol, which is very low. Therefore, if $COOH^*$ is formed, it will react further very fast either to form CO^* or $CO_2{}^*$.

Based on the energy profiles of the three main reaction pathways, the carbide pathway shows the highest activation of $CO_2{}^*$. Therefore it is assumed that the reaction proceeds most favorably via this mechanism. Nevertheless, the carbide pathway has an extremely high activation barrier for the dissociation of CO^*, which is a big drawback in the hydrogenation of $CO_2{}^*$ to form methane. Consequently it is interesting to look for a reaction mechanism to circumvent the formation of CO^*.

5.2.2 Hydrogen-Assisted Versus Direct CO Dissociation

In order to decrease the energy barrier for CO* dissociation, co-adsorption of hydrogen was reported to be effective on Ru and Co in Fischer Tropsch reactions [37]. In this section we look into the energy barriers of the direct CO* dissociation, the dissociation of COH* to C* and OH* and the dissociation of the formate HCO* into CH* and O* to see whether the same holds for Ni. The energy profiles and barriers for the elementary reaction steps for each nickel facet are depicted in Figure 5.4, these energy barriers can also be read out from Figure 5.2. The geometries of the initial, transition and final states from the elementary reactions are shown in Appendix C.

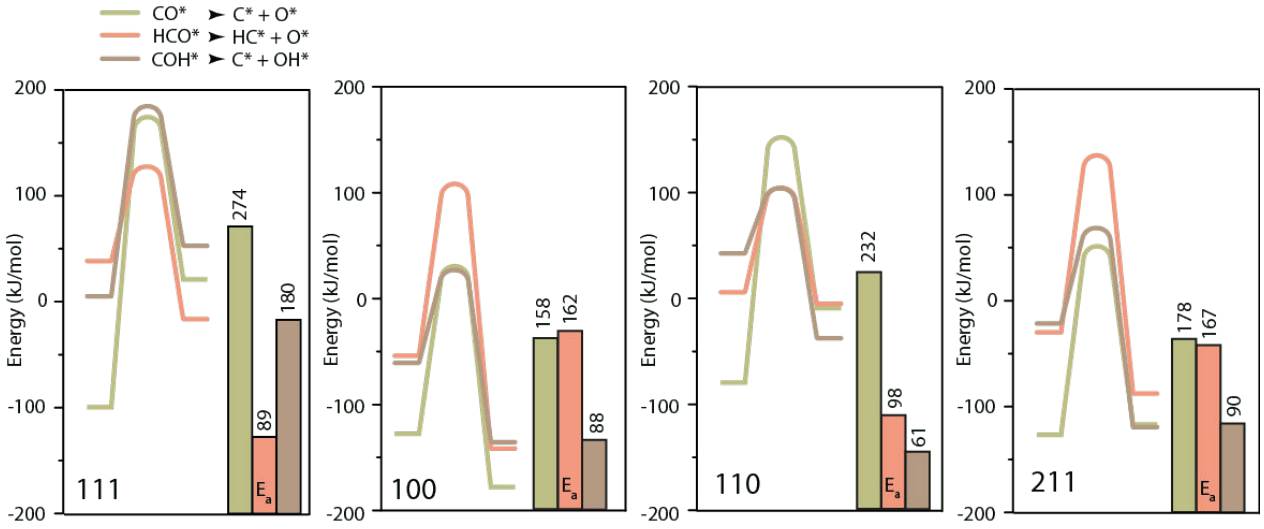

Figure 5.4: Reaction barriers in kJ/mol and potential energy diagrams of the elementary reactions direct CO* dissociation in green, C-O bond cleavage of COH* and HCO* in brown and in red respectively.

From Figure 5.4 it can be seen that for Ni(111), Ni(110) and Ni(211) the direct CO* dissociation is an endothermic process and gives the highest energy barrier. For Ni(100) direct CO* dissociation is exothermic and the energy barrier from HCO* to CH* is slightly higher. On the contrary, both hydrogen assisted CO* dissociations are exothermic elementary reactions on each nickel facet. For each nickel facet the high energy barrier of the direct CO* dissociation can be reduced by hydrogen assistance, with 185 kJ/mol, 70 kJ/mol, 171 kJ/mol and 88 kJ/mol on Ni(111), Ni(100), Ni(110) and Ni(211) respectively. However, this decrease in energy does not represent the complete reduction

of the energy barrier for direct CO* dissociation. In order to circumvent direct CO* dissociation, CO* needs to be hydrogenated first. For example in the case of Ni(111), the energy barrier to form HCO* is 158 kJ/mol and the C-O bond cleavage is 89 kJ/mol. This means that the energy barrier for CO* dissociation is reduced overall with 274-158=115 kJ/mol instead of 184 kJ/mol.

Based on the energy barriers depicted in Figure 5.4, on Ni(100), Ni(110) and Ni(211) CO* dissociation is energetically least demanding via COH*. For Ni(111) this is true for dissociation via HCO*. Unfortunately the activation barriers to form COH* by hydrogenation of CO* have not been calculated and therefore can not be compared with the formation of HCO*. Given that for the majority of the nickel facets the lowest energy barrier for C-O is found to go via COH* and in literature [65] it was found that CO dissociation on nickel was proposed to proceed through a COH* intermediate, it is highly recommended that these energy barriers are calculated on the four nickel facets in the nearby future.

Nevertheless, based on obtained reaction barriers we can conclude that H-assisted CO* dissociation is likely to be an active mechanism in C-O* bond breaking.

5.2.3 Energy Barriers for C-C Coupling

In Section 4.4 the stability of CH_xCH_y and CCO intermediates relative to the stability of C*, CH* and CO* were evaluated to assess the formation of higher hydrocarbons and alcohols over methane. It was found that the ethane intermediates, CH_xCH_y, were stable on each nickel facet and therefore it was hypothesized that the formation of ethane is most likely not structure sensitive. The relative stability of CCO was higher in energy, by which the formation of CCO from C* and CO* would be endothermic. In order to gain a better understanding of the formation of ethane and in a smaller amount the formation of other $C_{(2+)}$ products energy barriers should be taken into account. With the NEB-method the transition states were calculated for the formation of both CCH* and CCO* on each nickel facet. Images of the initial, transition and final state are depicted in Appendix C. Ea_F and Ea_B in kJ/mol are given in Figure 5.5.

The forward energy barriers for the formation of CCO* range approximately from 100 to 140 kJ/mol, which should be able to overcome under reaction condition as discussed in Section 4.2.

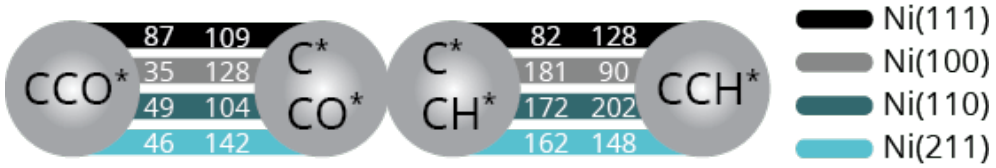

Figure 5.5: Energy barriers in kJ/mol for four nickel facets for the formation of CCO* and CCH* by C-C coupling of atomic carbon with CO* or CH* respectively.

However, the energy barrier for the backward reaction is significantly lower, which means that the decomposition of CCO* back into C* and CO* is much easier that its formation. So, based on the endothermic reaction of the formation of CCO* and the lower energy barrier for the decomposition of CCO* it is unlikely that alcoholic $C_{(2+)}$ products are formed via CO* insertion in C* during the reaction. In order to verify if there is a reasonable possibility that ethanol is formed during CO_2 hydrogenation it may be interesting to calculate the activation barriers for the coupling of C* or CH* with COH*, since COH* was found to be relatively stable on the four nickel facets as well (see Section 4.3).

The coupling of CH* to atomic carbon has an energy barrier of approximately 170 kJ/mol for Ni(100), Ni(110) and Ni(211). For Ni(111) the barrier is 82 kJ/mol, which is significantly lower. So, even though CCH* is stable on each nickel facet, the formation of CCH* is more facile on Ni(111).

The reason that only a small amount of ethane or other $C_{(2+)}$ products are formed, is most likely caused by the fact that nickel is such a good hydrogenation catalyst, which we already know from industrial processes in which fats and oils are hydrogenated over nickel catalysts [66]. This means that the coupling of two alkyl intermediates need to compete with the rate of the hydrogenation of these intermediates. It might be interesting if the product selectivity of CO_2 hydrogenation can be tuned a bit more toward ethane if the hydrogenation reaction is subdued by for example a lower CO_2/H_2 ratio or by selective poisoning of the catalyst. If the alkyl intermediates would get more time to recombine and, as a consequence, hypothetically more ethane could be formed.

5.3 Ultimate Reaction Mechanism

Using the calculated energy barriers, depicted in Figure 5.2, it is possible to extract an energetically most facile reaction pathway for CO_2 hydrogenation for the four nickel facets. This can be done as follows. Starting at $CO_{2(g)}$ in Figure 5.2, for each nickel facet there is one option to go to $CO_2{}^*$. Then, for $CO_2{}^*$, there are four elementary reaction steps to go to another intermediate. The first option is a C=O dissociation to form CO^*, there are two possibilities to hydrogenate $CO_2{}^*$ and finally it is also possible for $CO_2{}^*$ to desorb again from the metal surface. For example, for Ni(110) the lowest barrier is to hydrogenate $CO_2{}^*$ to $HCOO^*$ with 35 kJ/mol. However, the backward reaction is less difficult with 53 kJ/mol, which brings us back at $CO_2{}^*$. Looking for the second lowest activation barrier, $CO_2{}^*$ could be dissociated to CO^* and O^*. From this point, again the route with the lowest activation barrier is taken. This can be done for each nickel facet all the way towards the formation of methane, which results in four sequences of energy barriers, listed in Table 5.1.

Table 5.1: Energy barriers in kJ/mol for the most facile reaction mechanism for CO_2 hydrogenation over Ni(111), Ni(100), Ni(110) and Ni(211). In red the highest energy barrier per nickel facet.

	$CO_2{}^{(g)} \rightarrow CO_2{}^*$	$CO_2{}^* \rightarrow CO^*$	$CO^* \rightarrow HCO^*$	$HCO^* \rightarrow CH^*$
Ni(111)	49	50	158	89
Ni(100)	29	15	142	162
Ni(110)	17	39	117	98
Ni(211)	2	90	99	167
	$CH^* \rightarrow CH_2{}^*$	$CH_2{}^* \rightarrow CH_3{}^*$	$CH_3{}^* \rightarrow CH_4{}^{(g)}$	
Ni(111)	60	59	97	
Ni(100)	69	72	78	
Ni(110)	68	36	70	
Ni(211)	80	49	109	

For each facet the most facile reaction mechanism for CO_2 hydrogenation proceeds via the carbide mechanism with a side step to the intermediate HCO^*. Notice, energy barriers for the formation of COH^* from CO^* are not taken into account. The highest energy barrier is either the formation of HCO^* on Ni(111) and Ni(110) or the C-O bond cleavage from HCO^* on Ni(100) and Ni(211), which is indicated in red in Table 5.1. If one needs to make nickel nanoparticles consisting out of one facet, Ni(110) would perform best in CO_2 hydrogenation to methane with

a rate limiting step of 117 kJ/mol for the formation of HCO*. However, if all facets of a nickel nanoparticle consisting of Ni(111), Ni(100), Ni(110) and Ni(211) participate during the reaction and each reaction step occurs on the facet for which the energy barrier of the elementary reaction is the lowest, the rate limiting step would be the formation of HCO* on Ni(211) with 99 kJ/mol. This means that an ideal interplay of the four facets can increase the reaction rate approximately 25x compared to the reaction rate using Ni(110) exclusively. The energetically easiest reaction mechanism with an ideal interplay between the four nickel facets is depicted in yellow in Figure 5.6. On the path of each elementary reaction two numbers are shown, that is the forward activation barrier in kJ/mol and the corresponding nickel facet in brackets.

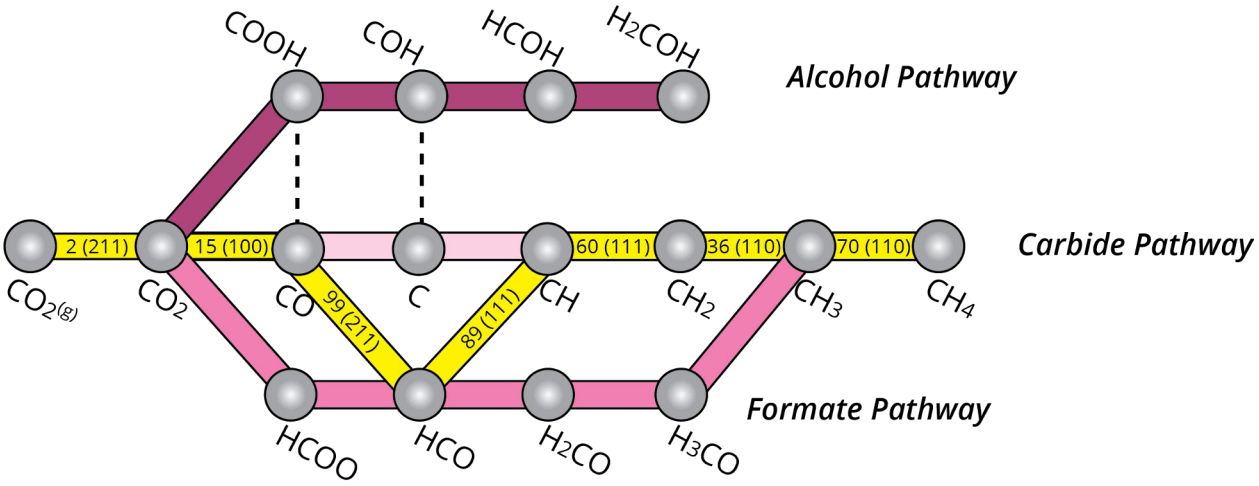

Figure 5.6: In yellow the energetically most facile reaction mechanism. For each elementary reaction the forward activation barrier in kJ/mol and the corresponding nickel facet are given.

6 Visualizing the Electron Density of CO_2* and CO_2‡

As discussed in Section 5.2 CO_2 hydrogenation over nickel falls into a potential well when CO_2* dissociates toward CO* and O*. This means that the reaction will proceed and that CO_2* is activated for further reactions. However, the energy barriers for this activation process are not the same for the four nickel facets, which is imperative for structure sensitivity as discussed in Section 1.5. The potential energy diagram for direct CO_2* dissociation as well as the forward and backward activation energies are depicted in Figure 6.1. Ranking the four nickel facets based on the hight of the forward activation energy gives the following sequence: Ni(100) < Ni(110) < Ni(111) < Ni(211), indicating that this elementary reaction step is most favorable over Ni(100) and least favorable over Ni(211). It is notable that this trend does not depend on the fact that the surface is either a terrace or a stepped surface, since these alternates within this sequence. In order to gain a deeper understanding of the fundamentals of the activation of CO_2* on the nickel surface, properties based on the density of states as well as geometrical features were examined.

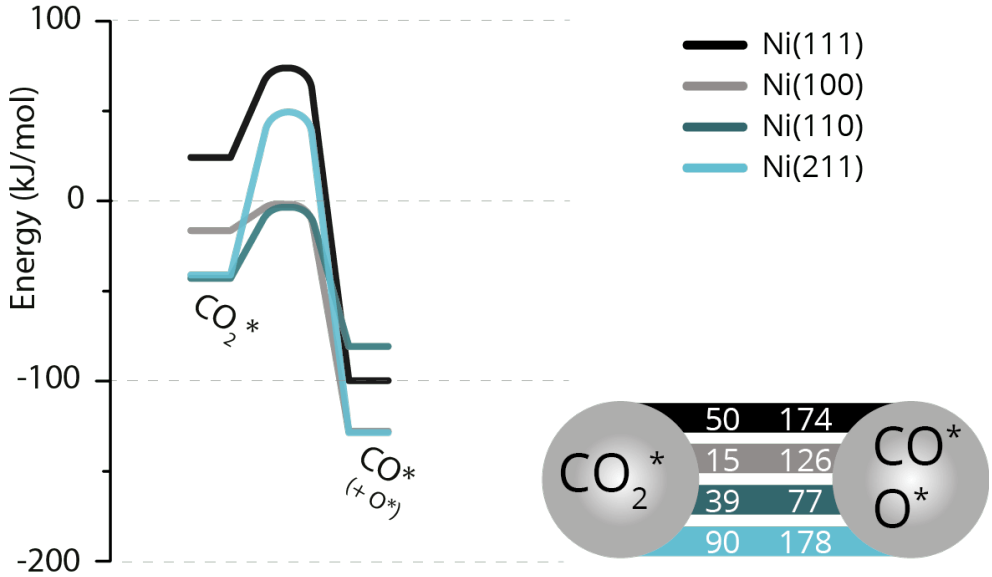

Figure 6.1: Potential energy diagram and corresponding forward and backward energy barriers for CO_2* dissociation toward CO* and O* on four nickel facets.

6.1 Density of States

In order to analyze the density of states from the optimized geometries of $CO_{2(g)}$ and $CO_2^{\ddagger}$, first the total density of states were calculated in the energy range -30 eV to 15 eV over 4500 grid points. With this calculation each point in the unit cell is assigned with the corresponding charge density. After this, the partial charge density corresponding to the energy interval of each molecular orbital was calculated. The contour plots of the electron density from these energy intervals were constructed using EPD software.

From these calculations the molecular orbital diagram of $CO_{2(g)}$ could be constructed, which is given in Figure 6.2b. Information from the CO_2 point group $D_{\infty h}$ was used for the labeling of the molecular orbitals. From this diagram we can learn that the HOMO is the non-bonding orbital $1\Pi_u$, which originates form the two oxygen atoms. The LUMO $4\Sigma_g^*$ is formed by a combination of both oxygen and carbon atoms. The orbitals on the left-hand side in the plot of the density of states, given in Figure 6.2c, are located more towards the nuclei of the CO_2 atoms. The density of states above the indicated Fermi level can be seen as virtual orbitals which could be filled either by excitation of core- or valance-electrons or by electron donation from the nickel surface in our case. The Fermi level is defined as the highest occupied energy level at T=0. These electrons are least well bound to the nuclei and therefore can be more easily promoted to nearby energy levels [18]. The contour plots of the molecular orbitals are visualized in Figure 6.2d-h, from which the orientation corresponds tot the orientation of CO_2 depicted in Figure 6.2a. According to Figure 6.2d,e,h, the electron density is located mainly on the oxygen atoms. This is in accordance with the molecular orbital diagram where $3\Sigma_g$, $2\Sigma_u$ and $1\Pi_u$ are formed from the atomic orbitals of oxygen. The molecular orbital $4\Sigma_g$ is clearly a combination of the three atoms, since its electron density, which is shown in Figure 6.2f, is located on both oxygen atoms as well as the carbon atom.

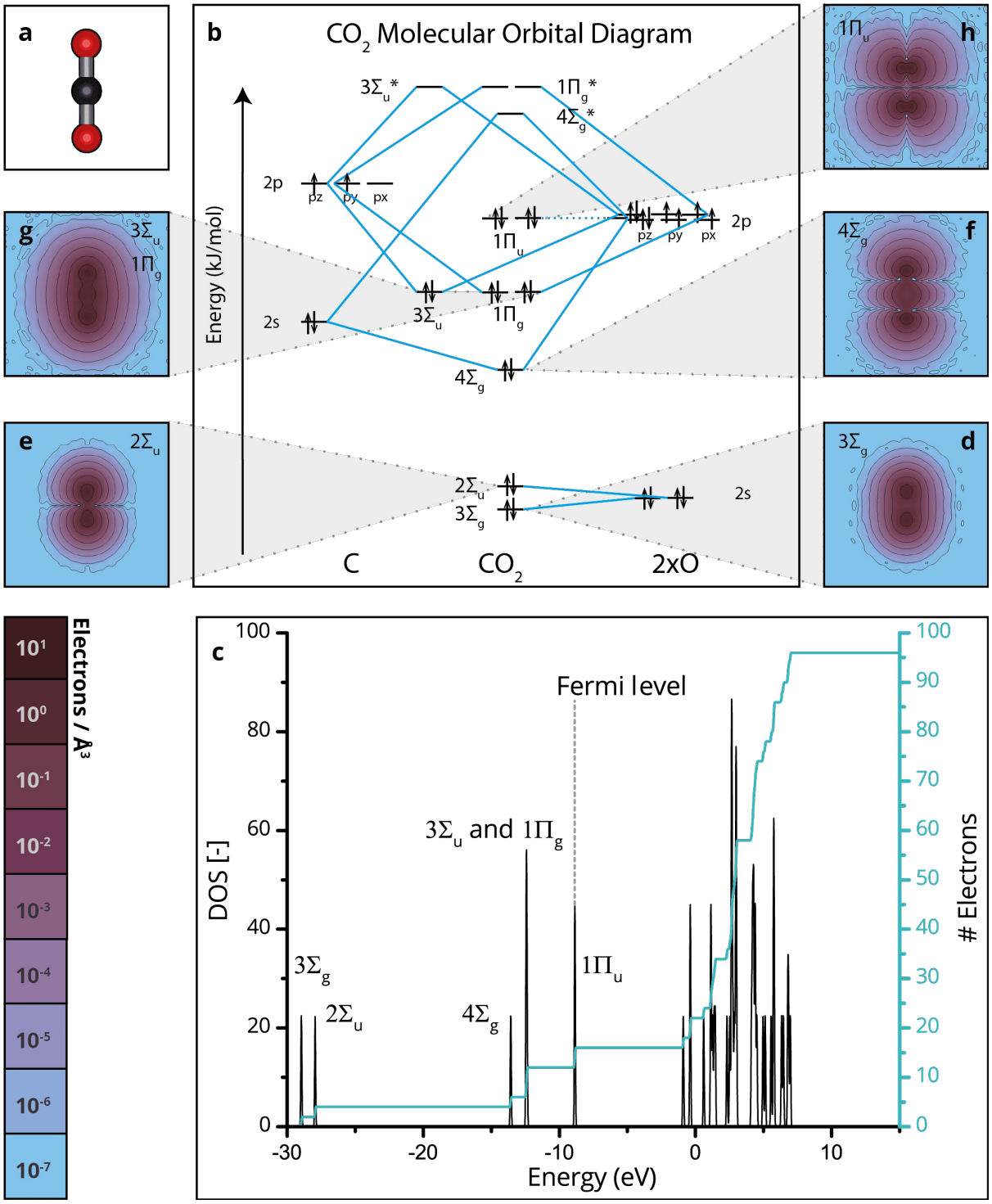

Figure 6.2: a) Orientation of $CO_{2(g)}$ corresponding to the orientation of the contour plots d-h. b) Molecular orbital diagram of $CO_{2(g)}$ constructed by its valance electrons. c) The density of states (DOS) and integrated DOS of $CO_{2(g)}$. Each peak corresponds to a molecular orbital. d-h) Electron density of each molecular orbitals plotted on a cutting plane running parallel through CO_2.

In order to break a C–O bond, the bond should be weakened by the metal surface by decreasing the bond order of CO_2. This can be achieved either by π-back-donation in which the LUMO will be filled with electrons from the metal or by σ-donation where the electron density in the HOMO is depleted towards the metal. In the case of CO_2, σ-donation would not result in a lower bond order, because the HOMO, $1\Pi_u$, is a non-bonding molecular orbital. Hence π-back-donation into $4\Sigma_g^*$ will be focused on.

The density of states diagram for the transition state $CO_2^{\ddagger}$, on the four nickel facets in the elementary reaction where one C–O bond is broken, is shown in Figure 6.3, the corresponding contour plots of the electron density are shown in Appendix E. The metal D-band is located roughly between -10 and 10 eV. The maximum value of the integrated density of states for Ni(110), the number of valance electrons indicated in blue, is approximately 200 electrons lower than for the other facets. The reason for this is that the construction of the Ni(110) slab 42 nickel atoms were used, while for Ni(111) and Ni(100) 63 and for Ni(211) 66 nickel atoms were used (see Section 2.3). Therefore the total amount of valance electrons on Ni(110) is significantly lower.

In all cases the energy of the bonding molecular orbitals $3\Sigma_u$, $1\Pi_g$ and $1\Pi_u$, but also the energy of the LUMO $4\Sigma_g^*$ and other anti-bonding orbitals from $CO_2^{\ddagger}$ are within the energy range of the metal D-band. This means that each nickel facet has a proper overlap between the anti-bonding orbitals of the adsorbate with the d-orbitals from the metal in order to facilitate π-back-donation from the metal to the adsorbate. From this it seems that the decrease in bond-order of CO_2^* is equally facile on each nickel facet.

The three deeper lying orbitals $3\Sigma_g$, $2\Sigma_u$ and $4\Sigma_g$, are located below the D-band and therefore these orbitals can be differentiated from the metal orbitals. However, compared to free CO_2, the

Table 6.1: Energy (eV) of the bonding molecular orbitals $3\Sigma_g$, $2\Sigma_u$ and $4\Sigma_g$ and the LUMO $4\Sigma_g^*$ of $CO_2\ddagger$ on four nickel facets.

Molecular Orbital	**111**	**100**	**110**	**211**
$3\Sigma_g$	-22.64	-22.58	-22.64	-23.01
$2\Sigma_u$	-20.02	-19.31	-19.58	-19.34
$4\Sigma_g$	-10.02	-9.70	-9.93	-9.50
$4\Sigma_g^*$ LUMO	-6.29	-6.12	-5.77	-6.13

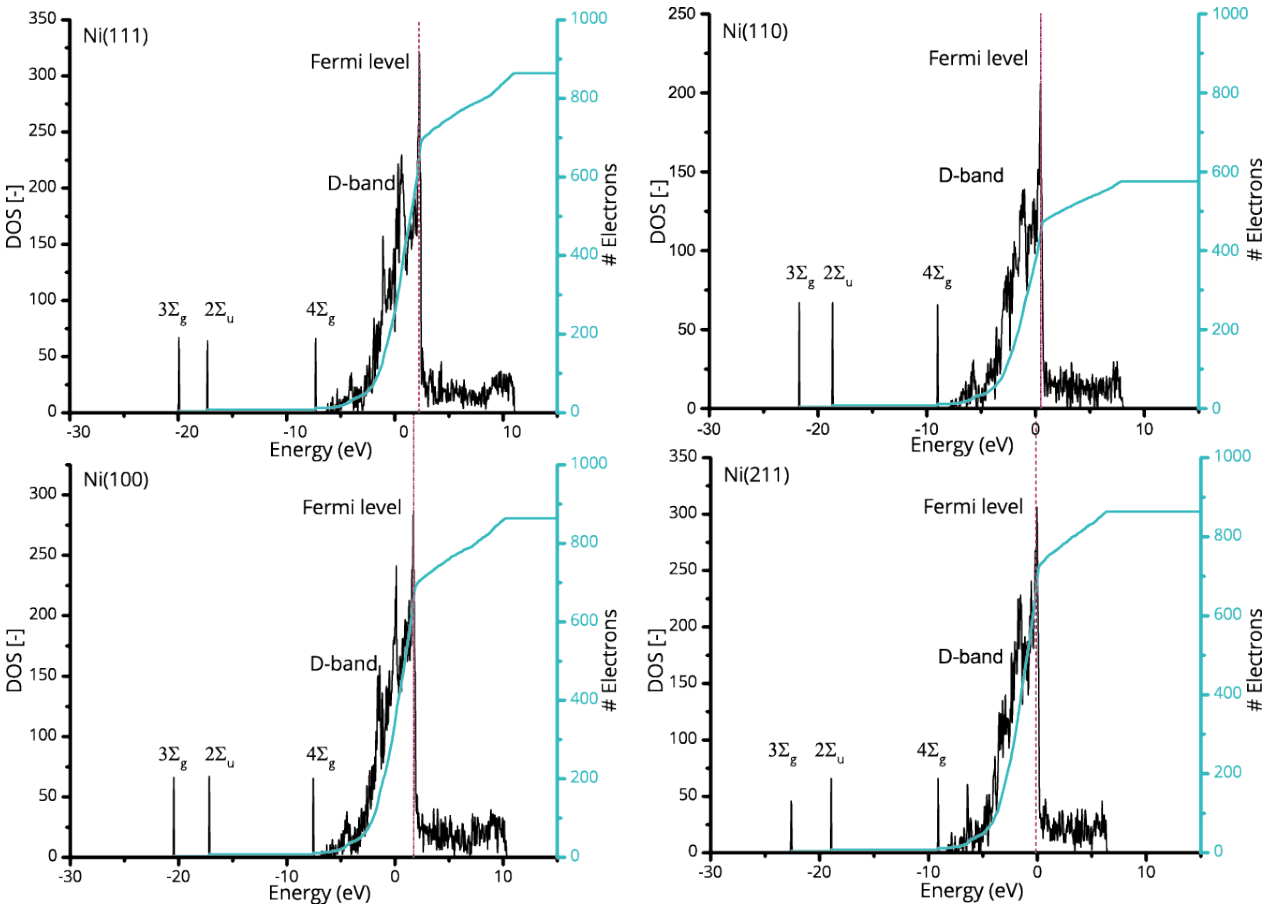

Figure 6.3: Density of states analysis of $CO_2^{\ddagger}$ on four nickel facets.

position of these orbitals are shifted towards higher energy values. This indicates already that the adsorbate CO_2^* indeed is activated by the metal surface, as discussed in Section 5.2.

The position of the three deeper lying orbitals, corrected for the corresponding Fermi level, are shown in Table 6.1. Here we can see that the energy of the orbitals differ for different nickel facets. This means that the activating effect is not based solely on the identity of the metal surface (i.e., nickel) but also on the mutual orientation of the surface with respect to the adsorbate. This is in line with the characteristics of a structure sensitive reaction. The electrons in the molecular orbitals that are 'pulled' more towards the metal D-band, become less tightly bound to the C and O nuclei, which results in an activation of the adsorbate by the metal surface. Therefore, by comparing the position of the Fermi-level corrected molecular orbitals of $CO_2^{\ddagger}$ on the different nickel facets, we now have a tool to rank the nickel facets in order of activating effect per molecular orbital. This

results in the following sequences:

- $3\Sigma_g$: 211 < 111 = 110 < 100
- $2\Sigma_u$: 111 < 110 < 211 < 100
- $4\Sigma_g$: 111 < 110 < 100 < 211

By analyzing the DOS (depicted in Appendix D) of both CO* and O* (the final state of the dissociation of CO_2*) we can verify that the molecular orbital $2\Sigma_u$ from CO_2* will be separated from $3\Sigma_g$ and $4\Sigma_g$ in order to form O* and CO* respectively. This indicates that the activation of the molecular orbital $2\Sigma_u$ is very important in direct CO_2 dissociation. Ni(100) activates molecular orbital $2\Sigma_u$ best, which is in accordance with the fact that the lowest energy barrier was found for Ni(100) in direct CO_2* dissociation. However, Ni(111) facilitates the lowest activation of the molecular orbital $2\Sigma_u$, but does not have the highest energy barrier (Fig.6.1). This indicates that other factors also need to be taken into account, in order to fully explain the difference in energy barriers for CO_2* dissociation on the different facets.

6.2 Coordination of $CO_2^{\ddagger}$ to the Nickel Facet

As explained above, the results of the activating effect of the molecular orbital $2\Sigma_u$ do not completely match the results of the activation barriers. This indicates that other factors play a role as well. Thus the specific coordination of $CO_2^{\ddagger}$ with respect to the metal atoms of the different nickel facets should also be taken into account.

The optimized geometries that result in the lowest energy barrier for direct CO_2 dissociation towards CO* and O* are presented in Figure 6.4. For the initial state, the most stable geometry for CO_2* on each facet was used. Subsequently, different possibilities for the final state were evaluated in order to calculate the corresponding transition state using the NEB-method as discussed in Section 5.1. Only the transition- and final state that gave the lowest energy barrier are depicted in Figure 6.4. Bond lengths, bond angles, adsorption sites and coordination numbers corresponding to the initial- transition- and final states depicted in Figure 6.4 are listed in Table 6.2.

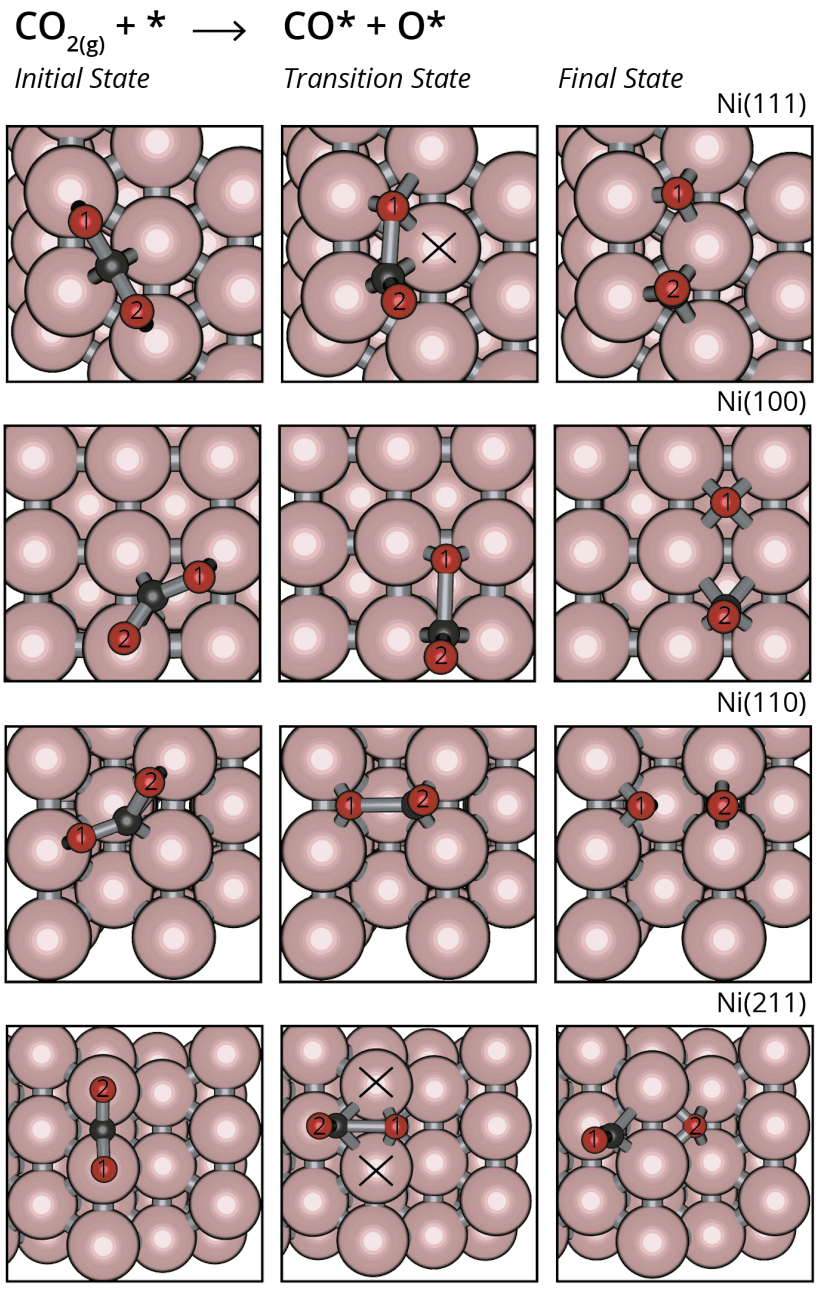

Figure 6.4: Geometries of CO_2^* on four nickel facets in the initial-, transition- and final state for direct CO_2 dissociation. The nickel atoms that are shared by the adsorbate in the transition state are indicated with a cross.

Table 6.2: The preferred adsorption site, bond distances [Å] and bond angle [ϑ] of the adsorbates in the Initial- Transition- and Final-State, Coordination Number (CN) in the Transition State for direct CO_2 dissociation on the four nickel facets.

	Ni(111)	**Ni(100)**	**Ni(110)**	**Ni(211)**
Initial State				
Adsorption site OCO	T, B, T	T, B, T	T_1, T_1, T_1	T_1, B_1, T_1
d_{C-O_1}	1.28	1.28	1.28	1.24
d_{C-O_2}	1.28	1.27	1.28	1.24
ϑ_{OCO}	132.15	129.17	125.65	139.88
Transition State				
Adsorption site OCO	T_h, B	B, B	T_f, B_1	B_1, T_{h2}
CN	5	4	5	5
d_{C-O_1}	1.68	1.82	1.78	1.83
d_{C-O_2}	1.20	1.19	1.20	1.19
ϑ_{OCO}	117.20	111.03	110.51	112.45
Final State				
Adsorption site CO and O	T_h, T_h	F, F	B_1, T_f	T_{h2}, F
d_{C-O}	1.19	1.21	1.18	1.20

The C-O_1 bond length in the transition state $CO_2^{\ddagger}$ is enlarged compared to the initial state, which is necessary for C-O_1 bond breaking. The longest C-O_1 bond in the transition state are found for Ni(211) and Ni(100). It might seem counter-intuitive that the highest activation barrier was found on Ni(211) and the lowest on Ni(100). However, this can be rationalized with the Bond Order Conservation (BOC) principle, which states that adsorbates bonded to the same surface metal atom are weakened by the presence of one another as a result of the competition for electron density from the same metal atom [67]. If an adsorbate in the transition state shares the least amount of same metal atoms, the transition state is more stable, which results in a lower activation barrier. This is true for both Ni(100) and Ni(110) where no nickel atoms are shared during the dissociation of CO_2*. The nickel atoms shared during the C-O_1 dissociation are indicated with a cross in Figure 6.4. Ni(111) shares one and Ni(211) shares two nickel atoms, which corresponds well to the second highest and highest energy barrier respectively. According to the BOC-principle,

Ni(110) and Ni(100) should have the lowest energy barriers in $CO_2{}^*$ dissociation, which corresponds to the found values (Fig.6.1).

6.3 Conclusions

Through the combination of DOS analysis and the specific geometries of $CO_2{}^{\ddagger}$, we found fundamental reasons for the structure sensitivity of the elementary reaction step of direct $CO_2{}^*$ dissociation.

With the analysis of the density of states of $CO_{2(g)}$ compared to $CO_2{}^{\ddagger}$ on four nickel facets, we found that the molecular orbitals from $CO_2{}^{\ddagger}$ are shifted toward the metal D-band. This explains that $CO_2{}^{\ddagger}$ is activated for further reactions compared to $CO_{2(g)}$. The extent to which the molecular orbitals are shifted varies over the four nickel facets, indicating that the direct $CO_2{}^*$ dissociation is a structure sensitive reaction.

With the DOS analysis of the final state of $CO_2{}^*$ dissociation, it was shown that the molecular orbital $2\Sigma_u$ will be separated from $3\Sigma_g$ and $4\Sigma_g$ in order to form CO^* and O^*. Therefore the activation of $2\Sigma_u$ in $CO_2{}^{\ddagger}$ is very important for direct $CO_2{}^*$ dissociation. The highest energy shift of $2\Sigma_u$ toward the metal D-band was found on Ni(100). Therefore it can be explained that on Ni(100) the lowest energy barrier was found for this elementary reaction step.

The sequence from lowest to highest activation barrier of the direct $CO_2{}^*$ dissociation corresponds to the increase in shared metal atoms in the transition state, which is in accordance with the BOC-principle.

The transition states were studied starting from $CO_2{}^*$ in its most stable configuration. This, of course, limits the amount of possibilities for the specific configuration of the transition state. Based on the BOC-principle we found that the geometry of $CO_2{}^{\ddagger}$ on Ni(211) shared 2 nickel atoms, which results in the highest activation barrier compared to other facets. However, other transition states for example where C–O_1 is located on the fourfold side can be considered as well. Such a coordination would potentially decrease the activation barrier of the elementary reaction step on Ni(211).

7 Conclusions and Discussion

In this work CO_2 hydrogenation over four nickel facets has been investigated by means of DFT quantum chemical calculations. In Chapter 4, stable geometries of possible intermediates were calculated. Elementary reaction steps in direct and hydrogen-assisted CO dissociation as well as hydrogenation of carbide- formate- and alcohol- intermediates were calculated in Chapter 5. In Chapter 6 the electron density of $CO_2{}^*$ and $CO_2{}^‡$ were evaluated. With these calculations we are able to answer the research questions stated in Section 2.1:

1. Can the formation of the reaction intermediates $HCOO^*$ and CO^* as well as the formation of gaseous CO be explained?
2. What is the predominant reaction mechanism and which surface facet is the most ideal in CO_2 hydrogenation towards methane?
3. How is this reaction structure sensitive? Which reaction steps are energetically most demanding?
4. Which reaction path is responsible for the formation of the C-C coupled species like ethanol and ethane?
5. What is the reason that ethanol might be formed, but no methanol was detected?

7.1 Explanation Experimental Observations

The following conclusions account for several observations using FT-IR-spectroscopy during CO_2 hydrogenation over supported nickel catalysts. Firstly, the reason that the surface intermediate CO^* was detected is that this intermediate is very stable on each nickel facet. We also found that the formation of CO^* from $CO_2{}^*$ has a relatively low energy barrier for each nickel facet. However, a subsequent reaction step with CO^* is much more difficult, due to the significant higher energy barriers. Also, the rate limiting step in the energetically most favorable reaction mechanism that was calculated for CO_2 hydrogenation over nickel was found to be the hydrogenation of CO^* toward HCO^*. With these findings we can conclude that there will be a high surface coverage of the highly infrared active CO^* intermediate on the nickel nanoparticles during the reaction.

Secondly, $HCOO^*$ was also detected with FT-IR-spectroscopy, even tough this intermediate does not form part of the reaction mechanism that is likely to be most active during CO_2 hydrogenation. However, the formation of $HCOO^*$ by hydrogenation of $CO_2{}^*$ is energetically feasible, but the conversion of $HCOO^*$ either back to $CO_2{}^*$ or further to HCO^* is energetically more demanding due to the higher energy barriers. Therefore the formation of $HCOO^*$ will be relatively fast compared to any further reaction with this intermediate, which results in a somewhat longer lifetime of $HCOO^*$ on the nickel surface.

Next, the formation of gaseous CO was explained by the desorption of CO^* from any nickel surface. Although adsorbed CO^* was found to be very stable on each nickel facet, desorption of CO^* is entropically very favorable due to the increase in degrees of freedom. The reaction rate for CO^* desorption was calculated using the Arrhenius equation with the CO^* adsorption energy as the activation barrier. With this we found that under reaction conditions it is indeed possible for CO^* to desorb.

During FT-IR-spectroscopy also ethane and other $C_{(2+)}$ products were detected. Therefore the stability of $CH_x - CH_y$ coupled intermediates were evaluated and found to be stable on each nickel facet. Energy barriers for the coupling of C^* and CH^* only were calculated, because these alkyl intermediates are most stable and therefore there will be a relatively higher surface coverage of C^* and CH^* than the less stable $CH_2{}^*$ and $CH_3{}^*$. The most facile $C^* + CH^*$ coupling reaction was found on Ni(111) with an activation barrier of 82 kJ/mol. The barriers on the other nickel facets were twice as high. Therefore the formation of ethane is most likely to take place on Ni(111).

It is possible that the small amount of $C_{(2+)}$ products are (partially) alcohol species. Therefore the elementary reaction in which CO^* inserts into C^* was calculated. The formation of CCO^* by coupling of C^* and CO^* was found to be endothermic. Also the backward energy barrier was found to be significantly lower than the formation of CCO^*, which makes the formation of alcohol $C_{(2+)}$ intermediates and products less favorable compared to $C_{(2+)}$ hydrocarbons. However, it might still be possible that alcohol $C_{(2+)}$ products are formed via the coupling of CO^* with higher hydrogenated alkyl intermediates. In order to evaluate the chemical identity of the $C_{(2+)}$ products, more elementary reaction steps need to be calculated in which H_zCO^* or COH^* and CH_x^* couples

with alkyl intermediates CH_y^*.

The fact that no methanol was detected with FR-IR-spectroscopy, but higher alcohols like ethanol are possibly formed via CO-insertion, can be explained by the fact that the alcohol mechanism is endothermic. The alcohol intermediates are less stable compared to the intermediates formed during the carbide as well as the formate mechanism. Therefore H_2COH^* will not be formed and consequently its hydrogenation toward methanol won't occur. The formation of the higher hydrogenated intermediates in the formate mechanism is not likely, because this would be an endothermic process. This means that also the formation of methanol by hydrogenation of H_3CO^* does not occur. The underlying reaction mechanism in the formation of alcohol products are only based on CO-insertion mechanisms and not by hydrogenation of alcohol- or formate intermediates.

7.2 Predominant Reaction Mechanism

Based on calculations of the stability of reaction intermediates and NEB calculations performed on the four nickel facets, an energetically favorable reaction mechanism could be deduced. To be clear, we do not claim to have found the *most favorable* reaction mechanism. In order to find the most favorable mechanism, each elementary reaction step needs to be optimized in order to find the lowest energy barrier possible on each facet. However, the work described in this thesis is extended and complete, thus general conclusions can be drawn about an energetically favorable reaction mechanism for CO_2 hydrogenation over nickel.

CO_2 hydrogenation is most facile via the carbide mechanism, with a H-assisted C–O dissociation via the HCO^* intermediate. Intermediates formed via both the alcohol- and the formate- mechanism are too high in energy, causing the overall reaction to be endothermic. Therefore these mechanisms are not likely to occur to a large extent in CO_2 hydrogenation over nickel.

We found that C–O dissociation on each nickel facet is very difficult due to a very high activation energy. The energy barrier is significant lower when co-adsorbed hydrogen is used in order to facilitate a hydrogen-assisted C–O dissociation. For Ni(100), Ni(110) and Ni(211) the lowest energy barrier was found if the hydrogen assisted C–O dissociation would proceed via COH^*. For Ni(111) the C–O dissociation is most facile via HCO^*. It is highly recommended that the energy barriers

for the formation of COH* from CO* and H* are calculated and compared with the activation barriers to form HCO*. If these barriers appears to be lower than those to form HCO*, the easiest pathway to hydrogenate CO_2 over nickel would go via the carbide mechanism, with a H-assisted C–O dissociation via the COH* intermediate.

Examining the results for the four nickel facet separately, one could conclude that CO_2 hydrogenation toward methane is energetically least demanding on Ni(110). The rate limiting step is 117 kJ/mol in the formation of HCO* by hydrogenation of CO*. However, in catalysis the reaction intermediates are (to a variable extent) mobile on the nickel surface. If all facets of a nickel nanoparticle consisting out of Ni(111), Ni(100), Ni(110) and Ni(211) participate during the reaction with an ideal interplay in such a manner that each reaction step occurs on the facet on which the lowest energy barrier was found, then the highest energy barrier would be 99 kJ/mol for the formation of HCO* on Ni(211). The reaction mechanism would also proceed via the carbide mechanism except for the second C–O bond cleavage, this would proceed via a hydrogen-assisted mechanism, via a HCO* intermediate. Each nickel facet is necessary in this ideal interplay in order to hydrogenate CO_2 via the lowest energy demanding pathway.

The question is of course to which extent such an ideal interplay is feasible during a reaction. For this the intermediates should be able to migrate via lateral displacements, so the surface must not be completely saturated. This means that the surface coverage is an important parameter. Also the different facets need to be in proximity of each other in order for the intermediates to migrate to the appropriate facet. This will limit the size of the facets and the size of the nanoparticle.

7.3 Structure Sensitivity

The final question that needs to be answered is during which reaction steps CO_2 hydrogenation over nickel is a structure sensitive reaction. The most important findings are described below.

The four nickel facets have different surface structures and therefore, different interactions with the adsorbates are possible. As a result different adsorption energies were found for each intermediate on different facets even tough comparable adsorption sites were used, see Appendix B. For example the adsorption energy of CO* in a fourfold site (F) on Ni(100) and Ni(211) are -174.8 and

-159.2 kJ/mol respectively.

We found that the adsorption of $CO_{2(g)}$, the very first step in the reaction, already is structure sensitive. This elementary reaction step would be most facile on Ni(211), because on this facet the reaction would be exothermic and on this facet the lowest energy barrier was found. Ni(111) would be least eligible for this elementary reaction, because each calculated $CO_2{}^*$ was found to be endothermic. Also the highest energy barrier was found on Ni(111).

Based on the density of states and the BOC-principle we found that the dissociation of $CO_2{}^*$ to CO^* was energetically most favorable on Ni(100). The reason for this is that the molecular orbital $2\Sigma_u$ from $CO_2{}^*$ was most shifted toward the metal D-band on Ni(100). Also the transition state $CO_2{}^{\ddagger}$ was most stabilized on Ni(100) and Ni(110), because no nickel atoms are shared in the transition state.

8 Outlook

In order to build further on this project, several recommendations can be made. As mentioned before, it is important to calculate the transition states and the activation barriers on the four nickel facets for the formation of COH^* from CO^* and H^*. This elementary reaction step can potentially be part of the energetically most favorable reaction mechanism, since the hydrogen assisted C–O dissociation was found to be the most facile on Ni(100), Ni(110) and Ni(211) via COH^*.

Aiming at a better approximation in modeling of the real catalytic system used for CO_2 hydrogenation over supported nickel catalysts, both micro-kinetic modeling and a study on support effects on nickel are valuable. With this current work a detailed understanding of most elementary reaction steps in CO_2 hydrogenation over various nickel facets is obtained. From this the most active reaction mechanism and rate determining steps were derived. However, in catalysis macroscopic parameters such as temperature, pressure and concentration are very determining factors with respect to the progress of the reaction. By use of micro-kinetic modeling, the behavior of our system can be evaluated as a function of these macroscopic parameters that describes the system. A deeper insight in the catalytic system can be obtained by studying support induced effects on the hydrogenation reaction. It can be examined if there are support-induced differences in electronic properties like chemisorption energies and activation barriers or if there is an effect on the interaction between an adsorbate and a nickel nanoparticle that is supported on for example SiO_2.

9 Acknowledgements

First I would like to thank prof. dr. ir. Bert Weckhuysen for letting me work in your research group at Inorganic Chemistry and Catalysis.

A lot of thanks to dr. ir. Ivo Filot, who helped and learned me a lot about computational chemistry. I enjoyed our meetings, which were always interesting and helpful in putting me (back) on track. Your calm way and visual manner of explaining complex matter really suits me and I think you are a great teacher. I also learned a lot from you by reading and rereading your clearly written and very nicely illustrated dissertation.

I would like to express my special thanks to my daily supervisor Charlotte Vogt. Thank you for the great opportunities you gave me. Letting me work on this interesting research project and you outsourcing the computational part of your project to me. Going on a beam-trip, twice!, was an awesome experience. Your critical view, enthusiasm, clear and constructive feedback made it very pleasant working for you. I also appreciate you being kind, understanding and supportive when I went through a very shitty period. Thanks for the time and effort you put in helping me to become a better presenter. Not only by telling me how I come across and where the difficulties where, but also by showing me and practicing with me on how I could improve this. It has born fruit already, in my successful final masters presentation. I wish you the very best of luck for the future.

Bart Zijlstra who shared his office with me one day a week. Thank you for sometimes being a source of information by helping me to work with VASP, debugging my system in the beginnings and letting me use some of your very useful scrips.

I also want to acknowledge Jelle Boereboom for taking care of the first 'set' of computational time on cartesius and showing me how to work in a linux environment. Thanks for being a backup daily supervisor at the UU when Charlotte was out of the country.

Finally BASF and NWO are acknowledged for the funding of this project. The work described in this thesis was carried out on the Dutch national e-infrastructure with the support of SURF Foundation and carried out at both the University of Utrecht and the Eindhoven University of Technology.

References

[1] *Kuhn, T. S., 2012. The Structure of Scientific Revolutions. The University of Chicago Press, Chicago and London, 4th Ed., p.XI.*

[2] *Young, H.D., Freedman, R.A., 2008. Sears and Zemansky's University Physics. Pearson Addison-Wesley. p.1122, p.1307.*

[3] *Rozema, L. A., Darabi, A., Mahler, D. H., Hayat, A., Soudagar, Y., & Steinberg, A. M., 2012. Violation of Heisenberg's Measurement-Disturbance Relationship by Weak Measurements. Physical Review Letters, 109(10), p.100404-1-100404-5.*

[4] *Harris, D.C., & Bertolucci, M.D., 1978. Symmetry and Spectroscopy An Introduction to Vibrational and Electronic Spectroscopy. Dover Publications, New York, p.86, p.104.*

[5] *Ball, D.W., 2003. Physical Chemistry. Brooks/Cole-Thomson Learning, USA, p.485.*

[6] *Earth Observatory NASA, 2016. Global Warming: Feature Articles. http://earthobservatory.nasa.gov/Features/GlobalWarming/page2.php [Accessed 18 Oct. 2016].*

[7] *Union of Concerned Scientists, 2016. Global Warming Science. http://www.ucsusa.org/global_warming/science_and_impacts/science/CO2-and-global-warming-faq.html [Accessed 27 Nov. 2016].*

[8] *Earth Observatory NASA, 2016. World of Change: Global Temperatures: Feature Articles. http://earthobservatory.nasa.gov/Features/WorldOfChange/decadaltemp.php [Accessed 18 Oct. 2016].*

[9] *Environmental History Resources, 2016. Timeline Middle Ages and Early Modern Period - Environmental History Resources. https://www.eh-resources.org/timeline-middle-ages/ [Accessed 20 Oct. 2016].*

[10] *EPA, 2016. Climate Change: Basic Information. https://www.epa.gov/climatechange/climate-change-basic-information [Accessed 20 Oct. 2016].*

[11] *Fuss, S., Canadell, J. G., Peters, G. P., Tavoni, M., Andrew, R. M., Ciais, P., Jackson, R.B., Jons, C.D., Kraxner, F., Nakicenovic, N., Le Quéré, C., Raupach, M.R., Sharifi, A., Smith, P., & Yamagat, Y., 2014. Betting on Negative Emissions. Nature Climate Change, 4(10), p.850-853.*

[12] *Hoffert, M.I., Caldeira, K., Benford, G., Criswell, D.R., Green, C., Herzog, H., Jain, A.K., Kheshgi, H.S., Lackner, K.S., Lewis, J.S., & Lightfoot, H.D., 2002. Advanced Technology Paths to Global Climate Stability: Energy for a Greenhouse Planet. Science, 298(5595), p.981-987.*

[13] *Mahasenan, N., Smith, S., & Humphreys, K., 2003. The Cement Industry and Global Climate Change: Current and Potential Future Cement Industry CO_2 Emissions. Greenhouse Gas Control Technologies - 6th International Conference, Vol(II), p.995-1000.*

[14] *Brooks, K.P., Hu, J., Zhu, H., & Kee, R.J., 2007. Methanation of Carbon Dioxide by Hydrogen Reduction Using the Sabatier Process in Microchannel Reactors. Chemical Engineering Science, 62(4), p.1161-1170.*

[15] *Wang, W., Wang, S., Ma, X., & Gong, J., 2011. Recent Advances in Catalytic Hydrogenation of Carbon Dioxide. Chemical Society Reviews, 40(7), p.3703-3727.*

[16] *Kopyscinski, J., Schildhauer, T.J., & Biollaz, S.M., 2010. Production of Synthetic Natural Gas (SNG) From Coal and Dry Biomass–A Technology Review from 1950 to 2009. Fuel, 89(8), p.1763-1783.*

[17] *Neutrium, 2016. Properties Specific energy and energy of fuels. https://neutrium.net/properties/specific-energy-and-energy-density-of-fuels [Accessed 29 Nov. 2016].*

[18] *Atkins, P., Overton, T., Rourke, J., Weller, M., & Armstrong, F., 2010. Shriver and Atkins' Inorganic Chemistry, 5th Ed, Oxford University Press, USA, p.103, p.277, p.694.*

[19] *Verkerk, G., Broens, J.B., Bouwen, T.E.A., de Groot, P.A.M., Kranendonk, W., Vogelezang, M.J., Westra, J.J., & Wevers-Prijs, I.M., 2004. BINAS, 5th Ed, Wolters-Noordhoff, Groningen, table 12.*

[20] *Robertson, A.J.B., 1975. The Early History of Catalysis. Platinum Metals Review, 19(2), p.64-69.*

[21] *Sill, G. T., 1983. The Clouds of Venus: Sulfuric Acid by the Lead Chamber Process. Icarus, 53(1), p.10-17.*

[22] *Davy, H., 1816. On the Fire-damp of Coal Mines, and on Methods of Lighting the Mines so as to Prevent its Explosion. Philosophical Transactions of the Royal Society of London, 106, p.1-22.*

[23] *Davy, H., 1817. Some New Experiments and Observations on the Combustion of Gaseous Mixtures, With an Account of a Method of Preserving a Continued Light in Mixtures of Inflammable Gases and Air Without Flame. Philosophical Transactions of the Royal Society of London, 107, p.77-85.*

[24] *Berzelius, J.J., 1836. Quelques Idées Sur une Nouvelle Force Agissant Dans les Combinaisons des Corps Organiques. Ann. Chim, 61, p.146-151.*

[25] *Wilkinson, A.D.M.A., & McNaught, A.D., 1997. IUPAC Compendium of Chemical Terminology, 2nd Ed, International Union of Pure and Applied Chemistry, RSC Publishing, Cambridge, UK.*

[26] *Rothenberg, G., 2015. Catalysis: Concepts and Green Applications. John Wiley & Sons, Weinheim, p.65, p.130-131.*

[27] *Chorkendorff, I., & Niemantsverdriet, J. W., 2017. Concepts of Modern Catalysis and Kinetics. John Wiley & Sons, Weinheim, p.56-57, p.126.*

[28] *Yang, Y., Evans, J., Rodriguez, J.A., White, M.G., & Liu, P., 2010. Fundamental Studies of Methanol Synthesis from CO_2 Hydrogenation on Cu (111), Cu Clusters, and Cu/ZnO(0001). Physical Chemistry Chemical Physics, 12(33), p.9909-9917.*

[29] *Weatherbee, G.D., & Bartholomew, C.H., 1982. Hydrogenation of CO_2 on Group VIII Metals: II. Kinetics and Mechanism of CO_2 Hydrogenation on Nickel. Journal of Catalysis, 77(2), p.460-472.*

[30] *Roduner, E., 2006. Nanoscopic Materials Size-Dependent Phenomena. RSC Publishing, Cambridge, UK, p.140, p.239.*

[31] *Román-Martínez, M.C., Cazorla-Amorós, D., Salinas-Martínez de Lecea, C., & Linares-Solano, A., 1996. Structure Sensitivity of CO_2 Hydrogenation Reaction Catalyzed by Pt/Carbon Catalysts. Langmuir, 12(2), p.379-385.*

[32] *Van Santen, R.A., 2008. Complementary Structure Sensitive and Insensitive Catalytic Relationships. Accounts of Chemical Research, 42(1), p.57-66.*

[33] *Ligthart, D.A.J.M., Van Santen, R.A., & Hensen, E.J.M., 2011. Influence of Particle Size on the Activity and Stability in Steam Methane Reforming of Supported Rh Nanoparticles. Journal of Catalysis, 280(2), p.206-220.*

[34] *Van Hardeveld, R., & Van Montfoort, A., 1966. The Influence of Crystallite Size on the Adsorption of Molecular Nitrogen on Nickel, Palladium and Platinum: An Infrared and Electron-Microscopic Study. Surface Science, 4(4), p.396-430.*

[35] *Vogt, C., Groeneveld, E., Kamsma, G., Nachtegaal, M., Lu, L., Kiely, C. J., Berben, P.H., Meirer, F., & Weckhuysen, B. M., 2018. Unravelling Structure Sensitivity in CO_2 Hydrogenation over Nickel. Nature Catalysis, 1, p.127-134.*

[36] *Kattel, S., Liu, P., & Chen, J. G., 2017. Tuning Selectivity of CO_2 Hydrogenation Reactions at the Metal/Oxide Interface. Journal of the American Chemical Society, 139(29), p.9739-9754.*

[37] *Shetty, S., & van Santen, R. A., 2011. CO Dissociation on Ru and Co Surfaces: the Initial Step in the Fischer–Tropsch Synthesis. Catalysis Today, 171(1), p.168-173.*

[38] *Kresse, G. & Furthmüller, J., 1996. Efficiency of Ab-Initio Total Energy Calculations for Metals and Semiconductors Using a Plane-Wave Basis Set. Computational Materials Science, 6(1), p.15-50.*

[39] *Kresse, G., & Hafner, J., 1994. Ab-Initio Molecular-Dynamics Simulation of the Liquid-Metal–Amorphous-Semiconductor Transition in Germanium. Physical Review B, 49(20), p.14251-14269.*

[40] *Blöchl, P E., 1994. Projector Augmented-Wave Method. Physical Review B, 50(24), p.17953-17979.*

[41] *Kresse, G., & Joubert, D., 1999. From Ultrasoft Pseudopotentials to the Projector Augmented-Wave Method. Physical Review B, 59(3), p.1758-1775.*

[42] *Perdew, J.P., Burke, K., & Ernzerhof, M., 1996. Generalized Gradient Approximation Made Simple. Physical Review Letters, 77(18), p.3865.*

[43] *Element Collection, 2017. Technical Data for Nickel. http://periodictable.com/Elements/028/data.html [Accessed 3 Feb. 2018].*

[44] *Sheppard, D., Xiao, P., Chemelewski, W., Johnson, D. D., & Henkelman, G., 2012. A Generalized Solid-State Nudged Elastic Band Method. The Journal of Chemical Physics, 136(7), p.074103-1-074103-8.*

[45] *Koch, W., & Holthausen, M.C., 2015. A Chemist's Guide to Density Functional Theory. John Wiley & Sons, Weinheim, p.3-5*

[46] *Szabo, A., & Ostlund, N.S., 1989. Modern Quantum Chemistry: Introduction to Advanced Electronic Structure Theory. Courier Corporation, p.40-41*

[47] *Leach, A.R., 2001. Molecular Modeling Principles and Applications. Pearson Education Limited, UK, p.9, 127-130, 134, 155, 156.*

[48] *Steiner, E., 1996. The Chemistry Maths Book. Oxford University Press, USA, p.392, 393.*

[49] *Filot, I. A. W., 2015. Quantum Chemical and Microkinetic Modeling of the Fischer-Tropsch Reaction, Eindhoven University of Technology, p.31.*

[50] *Young, D., 2004. Computational Chemistry: a Practical Guide for Applying Techniques to Real World Problems. John Wiley & Sons, Weinheim, p.19, p.22-23.*

[51] *Hohenberg, P., & Kohn, W., 1964. Inhomogeneous Electron Gas. Physical Review, 136(3B), p. B864.*

[52] *Van Santen, R. A., & Sautet, P., 2009. Computational Methods in Catalysis and Materials Science: An Introduction for Scientists and Engineers. John Wiley & Sons, p.61.*

[53] *Kresse, G., Marsman, M., & Furthmüller, J., 2016. Computational Materials Physics, Faculty of Physics, Universität Wien. https://cms.mpi.univie.ac.at/vasp/vasp/vasp.html.*

[54] *Zhi, C., Wang, Q., Wang, B., Li, D., & Zhang, R., 2015. Insight Into the Mechanism of Methane Synthesis from Syngas on a Ni(111) Surface: a Theoretical Study. RSC Advances, 5(82), p.66742-66756.*

[55] *Filot, I. A., Broos, R. J., van Rijn, J. P., van Heugten, G. J., van Santen, R. A., & Hensen, E. J., 2015. First-Principles-Based Microkinetics Simulations of Synthesis Gas Conversion on a Stepped Rhodium Surface. ACS Catalysis, 5(9), p5453-5467.*

[56] *Kresse, G., 2000. Dissociation and Sticking of H_2 on the Ni(111),(100), and (110) Substrate. Physical Review B, 62(12), p.8295.*

[57] *Wang, S.G., et al., 2005. Chemisorption of CO_2 on Nickel Surfaces. The Journal of Physical Chemistry B, 109(40) p.18956-18963.*

[58] *Silaghi, M. C., Comas-Vives, A., & Coperet, C., 2016. CO_2 Activation on $Ni/\gamma Al_2O_3$ Catalysts by First-Principles Calculations: From Ideal Surfaces to Supported Nanoparticles. ACS Catalysis, 6(7), p.4501-4505.*

[59] *Zhu, Y. A., Chen, D., Zhou, X. G., & Yuan, W. K., 2009. DFT Studies of Dry Reforming of Methane on Ni Catalyst. Catalysis Today, 148(3-4), p.260-267.*

[60] *Zhou, Y. H., Lv, P. H., & Wang, G. C., 2006. DFT Studies of Methanol Decomposition on Ni(100) Surface: Compared with Ni(111) Surface. Journal of Molecular Catalysis A: Chemical, 258(1-2), p.203-215.*

[61] *Catapan, R. C., Oliveira, A. A., Chen, Y., & Vlachos, D. G., 2012. DFT Study of the Water–Gas Shift Reaction and Coke Formation on Ni(111) and Ni(211) Surfaces. The Journal of Physical Chemistry C, 116(38), p.20281-20291.*

[62] *Mohsenzadeh, A., Bolton, K., & Richards, T., 2014. DFT Study of the Adsorption and Dissociation of Water on Ni(111), Ni(110) and Ni(100) Surfaces. Surface Science, 627, p.1-10.*

[63] *Wang, S.G., et al., 2007. Factors Controlling the Interaction of CO_2 With Transition Metal Surfaces. The Journal of Physical Chemistry C, 111(45), p.16934-16940.*

[64] *UMET Université Lille, 2018. RheoMan - Nudged Elastic Band. http://umet.univ-lille1.fr/Projets/RheoMan/en/to-learn-more-about/nudged-elastic-band.php [Accessed 17 Apr. 2018].*

[65] *Andersson, M. P., et al., 2008. Structure Sensitivity of the Methanation Reaction: H_2-Induced CO Dissociation on Nickel Surfaces. Journal of Catalysis, 255(1), p.6-19.*

[66] *Jovanovic, D., Radovic, R., Mares, L., Stankovic, M., & Markovic, B., 1998. Nickel Hydrogenation Catalyst for Tallow Hydrogenation and for the Selective Hydrogenation of Sunflower Seed Oil and Soybean Oil. Catalysis Today, 43(1-2), p.21-28.*

[67] *Santen, R. A. V., Neurock, M., & Shetty, S. G., 2009. Reactivity Theory of Transition-Metal Surfaces: a Bronsted Evans Polanyi Linear Activation Energy, Free Energy Analysis. Chemical Reviews, 110(4), p.2005-2048.*

Appendices

Appendices

A Stable Geometries of Reaction Intermediates

The stable geometries of reaction intermediates are depicted in this Appendix. For clarity the stable geometry is given first in top-view and second in side-view. The order of the geometries is ranked from most stable to least stable geometry found.

Ni(111)

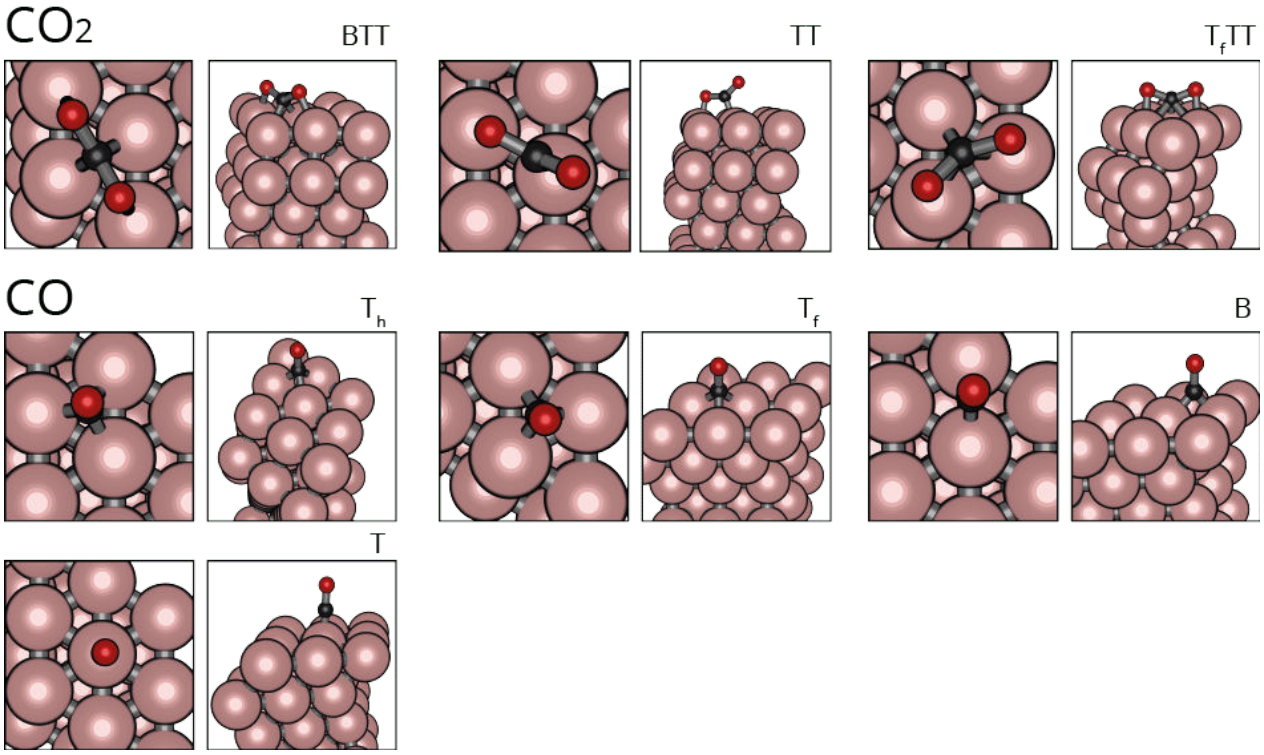

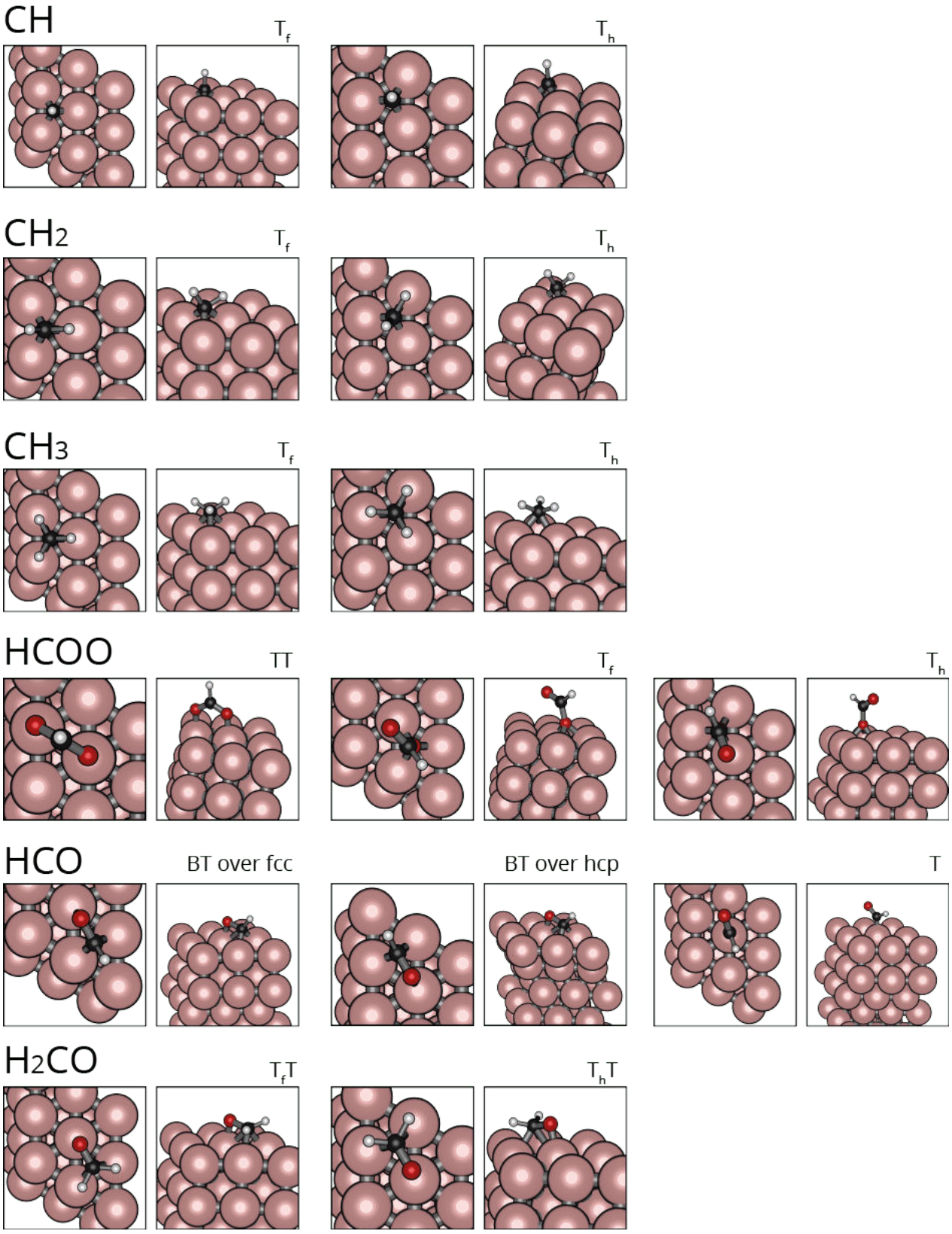
CH
T_f
T_h
CH2
T_f
T_h
CH3
T_f
T_h
HCOO
TT
T_f
T_h
HCO
BT over fcc
BT over hcp
T
H2CO
T_fT
T_hT

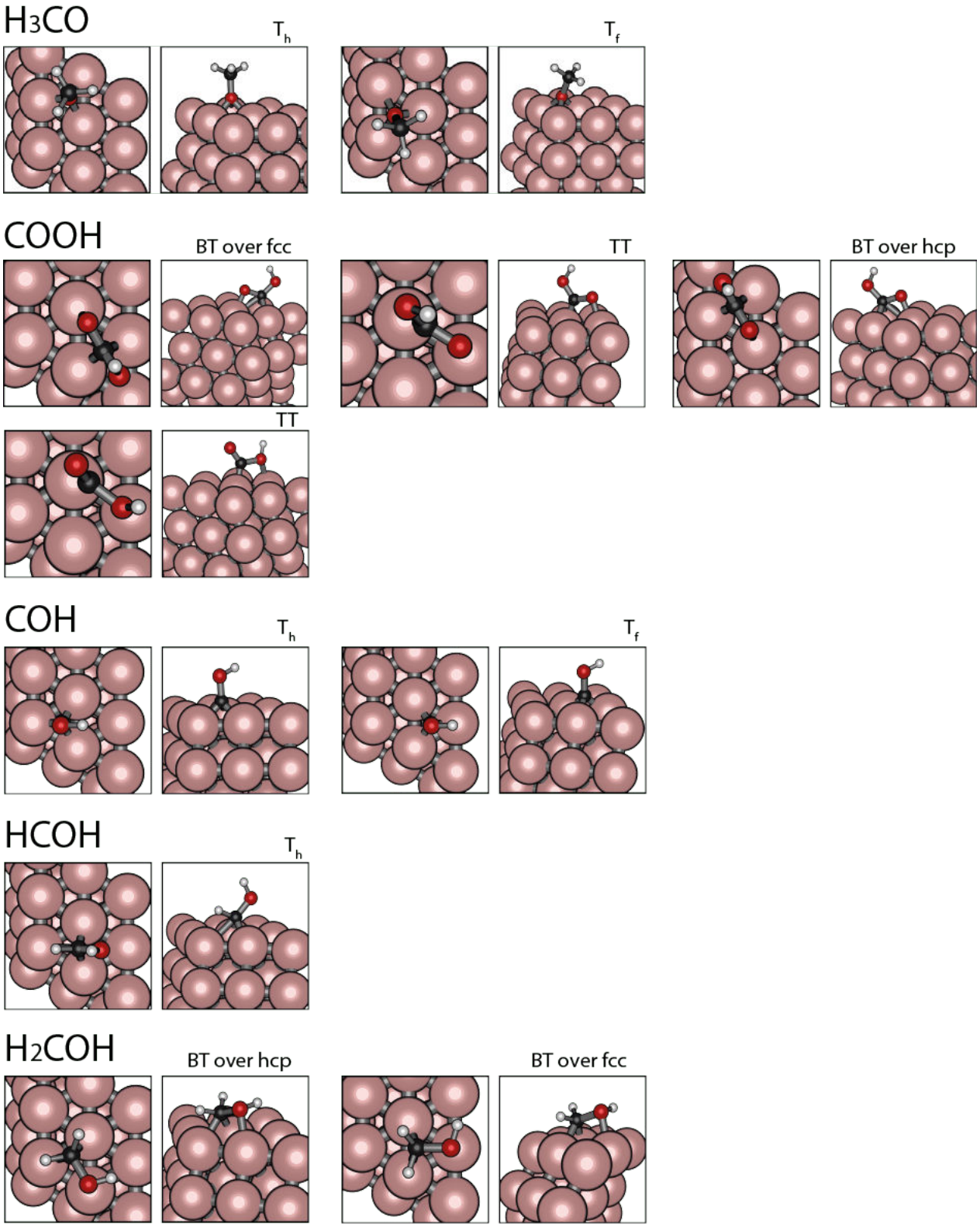
H3CO
Th
Tf
COOH
BT over fcc
TT
BT over hcp
TT
COH
Th
Tf
HCOH
Th
H2COH
BT over hcp
BT over fcc

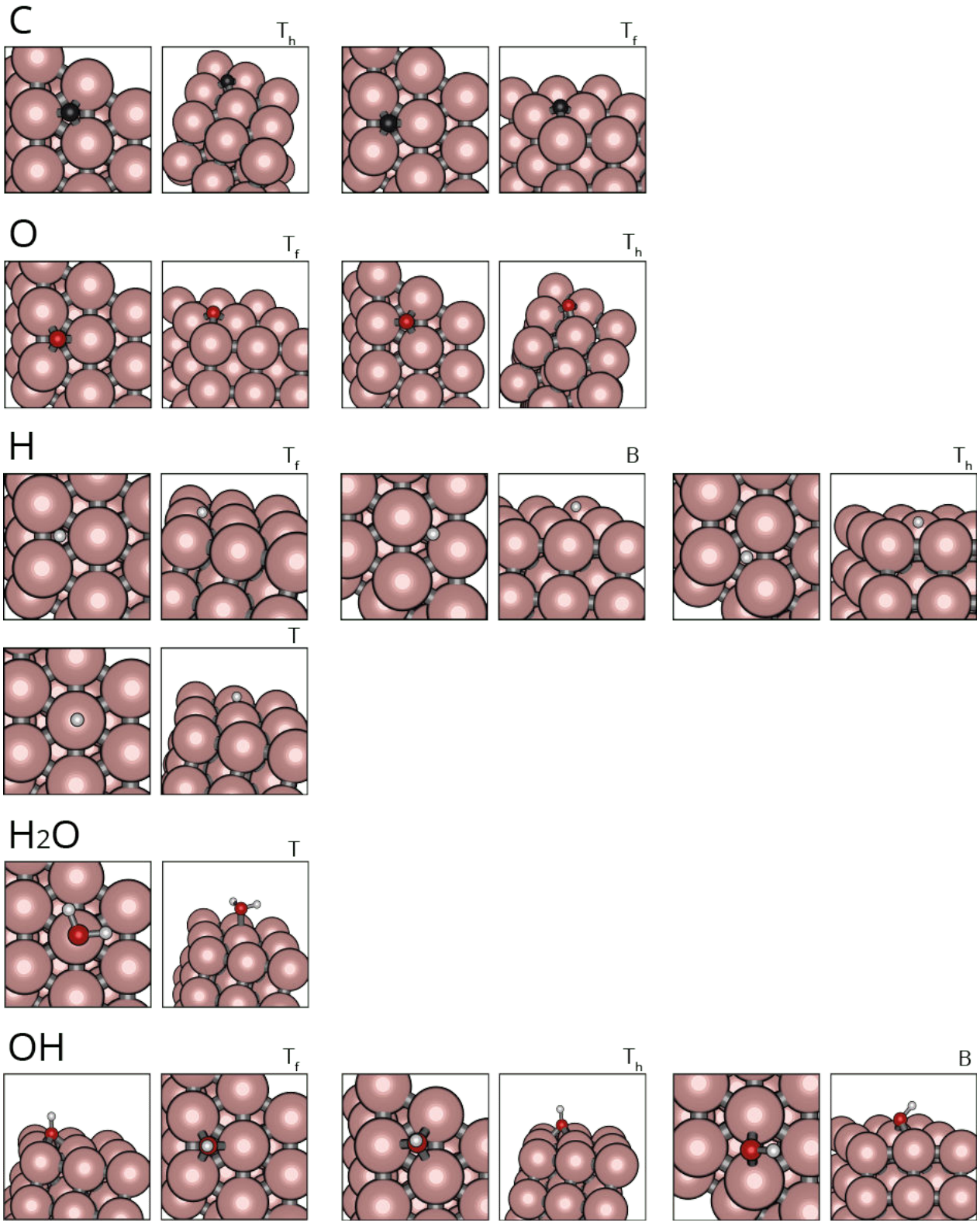
C
T_h
T_f
O
T_f
T_h
H
T_f
B
T_h
T
H2O
T
OH
T_f
T_h
B

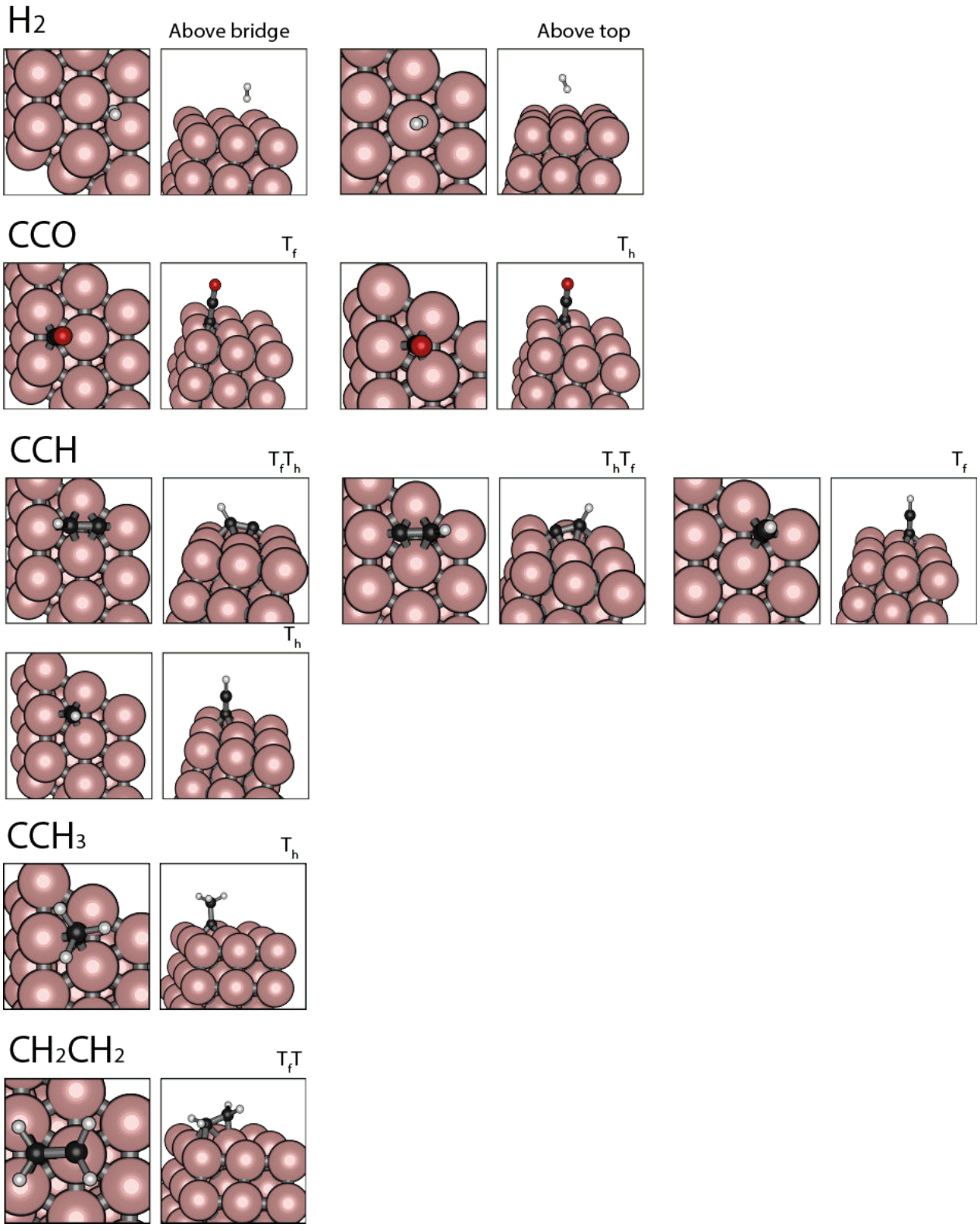
H2
Above bridge
Above top
CCO
Tf
Th
CCH
TfTh
ThTf
Tf
Th
CCH3
Th
CH2CH2
TfT

CH_2CH_3

B

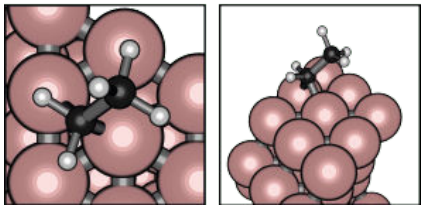

Ni(100)

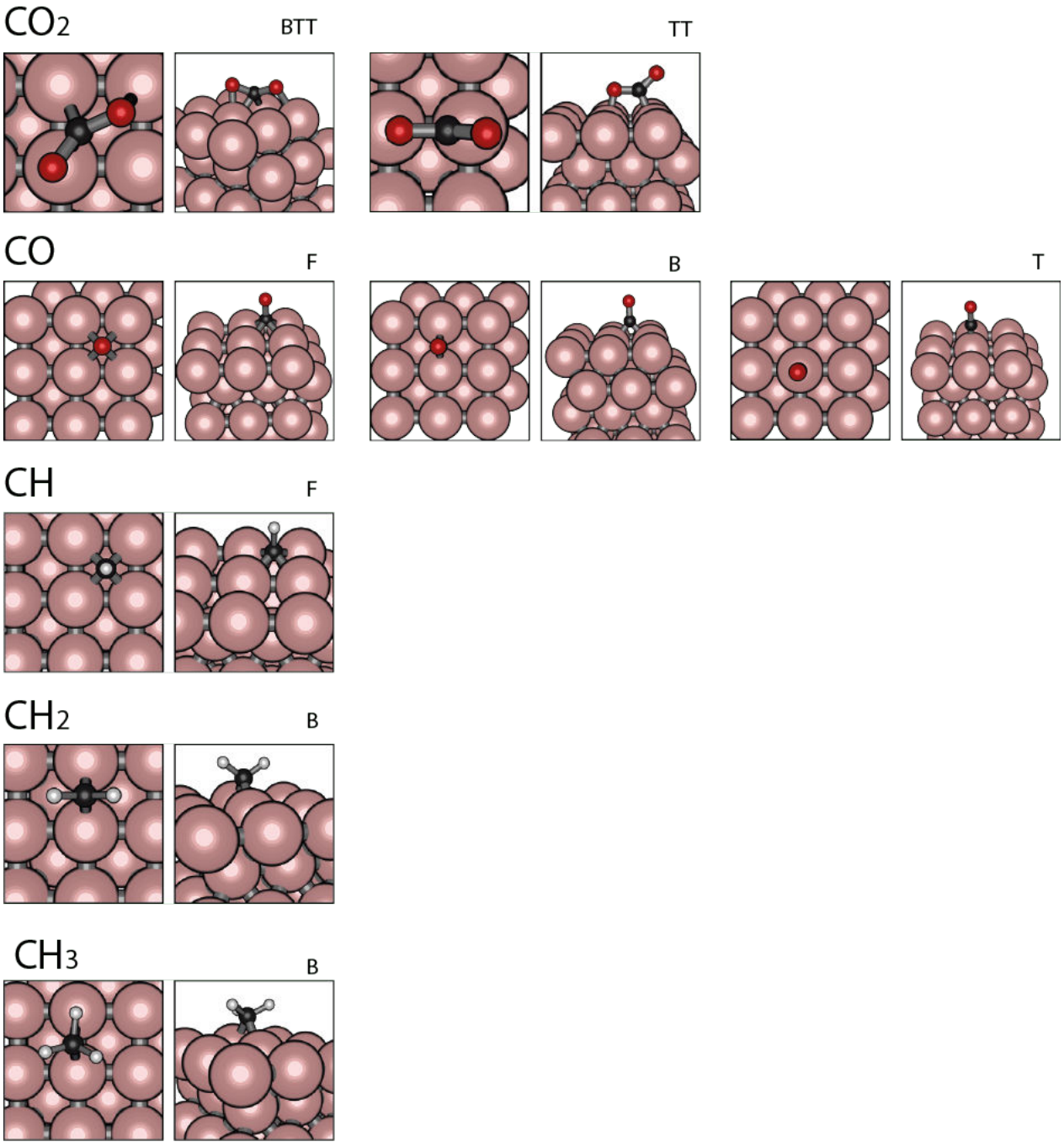

HCOO

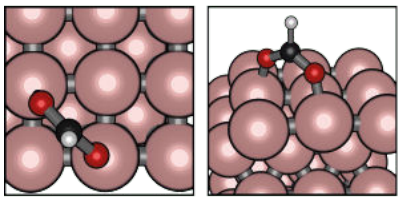

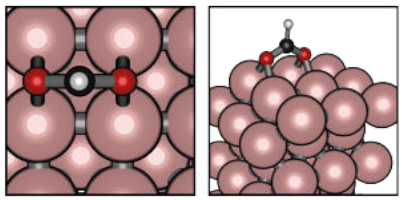

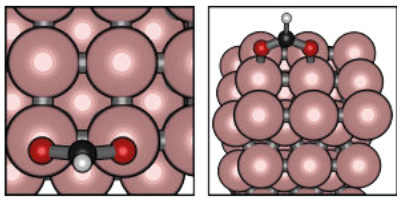

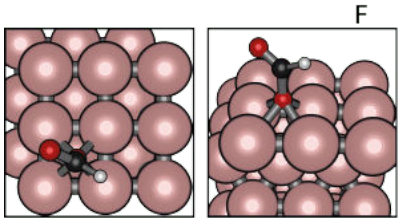

HCO

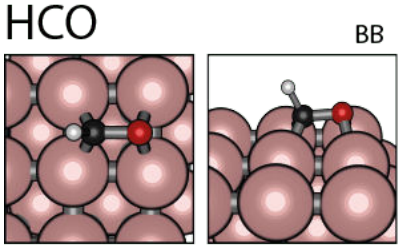

H_2CO

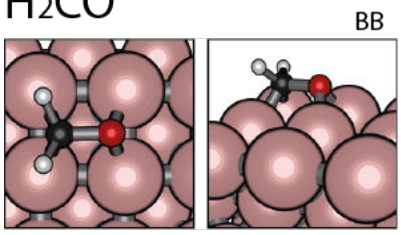

H_3CO

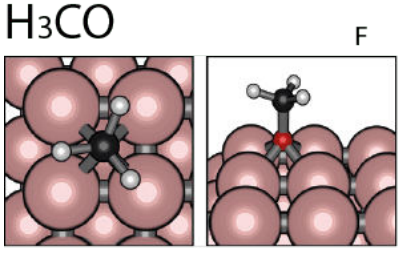

COOH

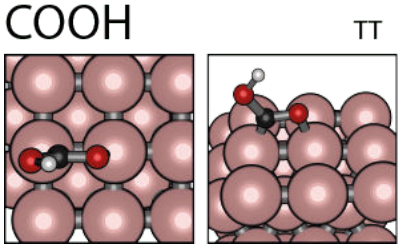

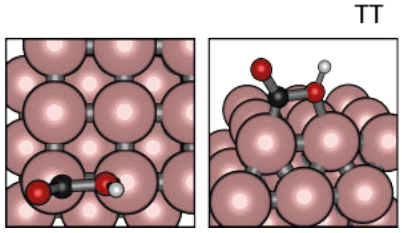

COH

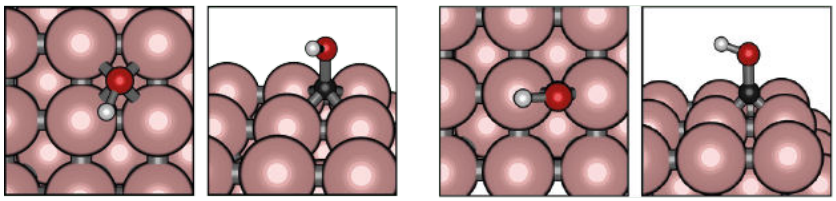

HCOH

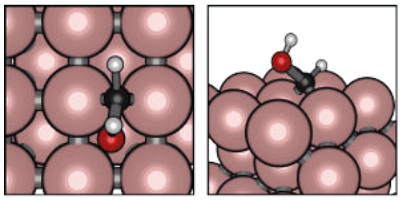

H_2COH

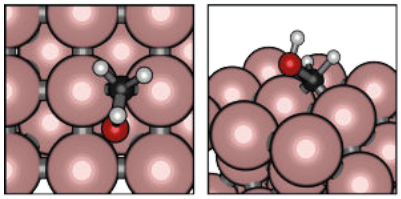

C

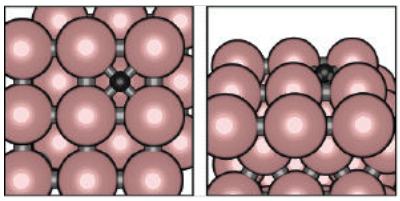

O

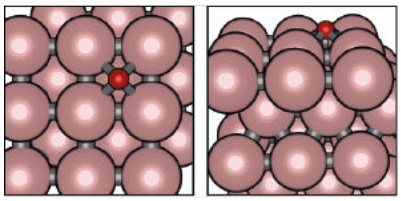

H

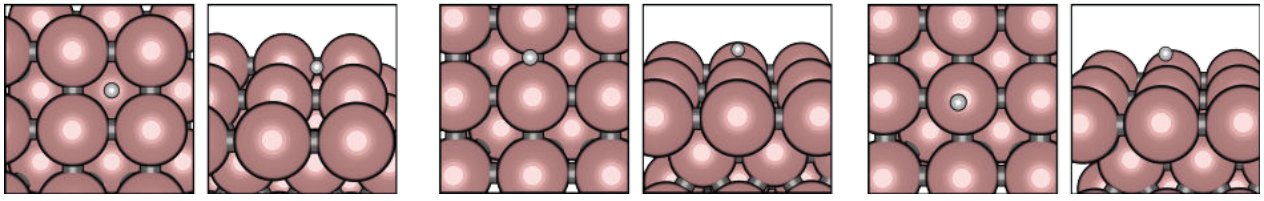

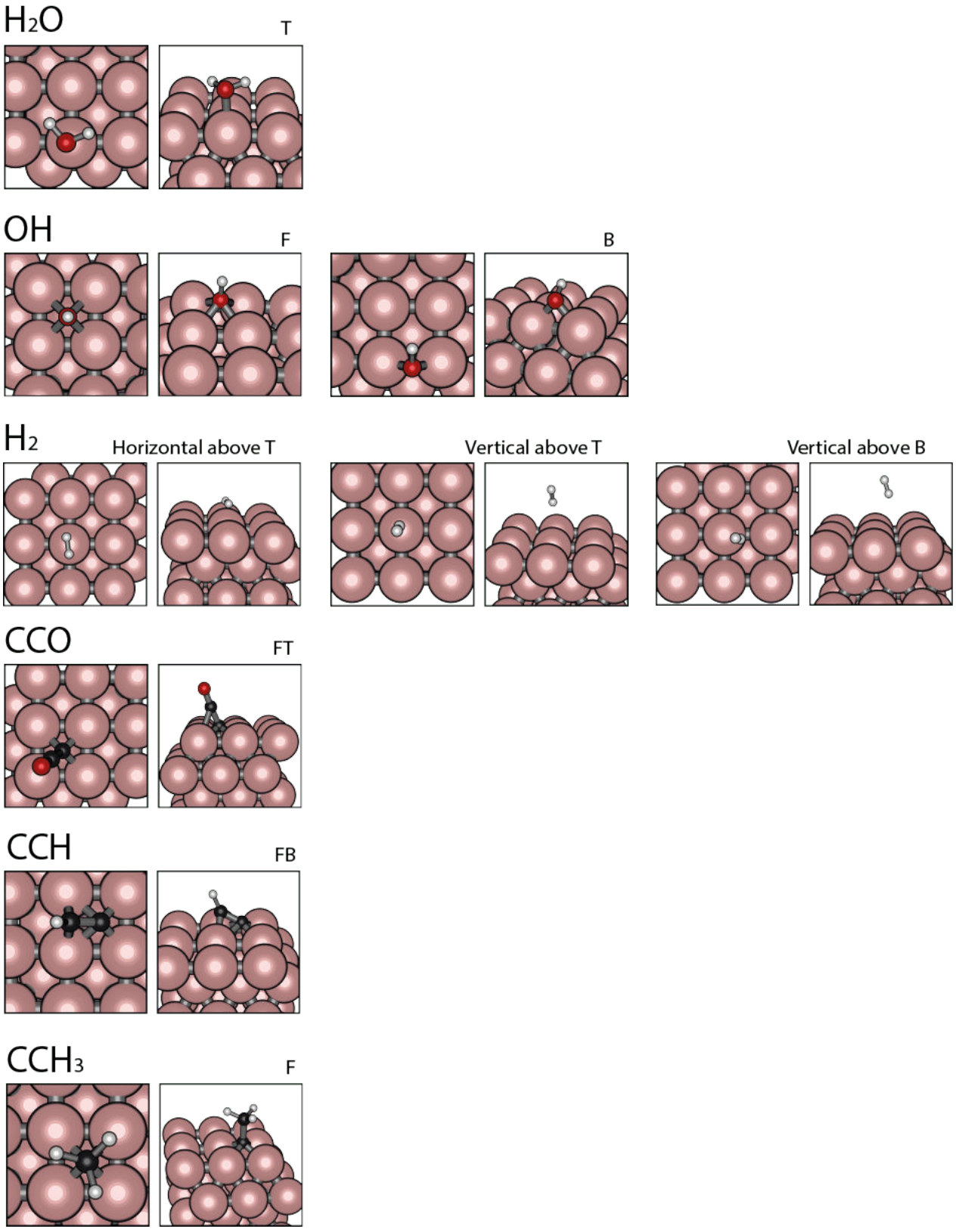
H2O
T
OH
F
B
H2
Horizontal above T
Vertical above T
Vertical above B
CCO
FT
CCH
FB
CCH3
F

CH_2CH_2 BT

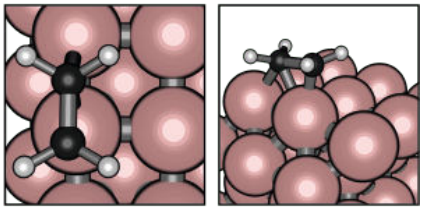

CH_2CH_3 B

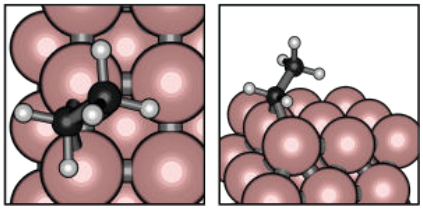

Ni(110)

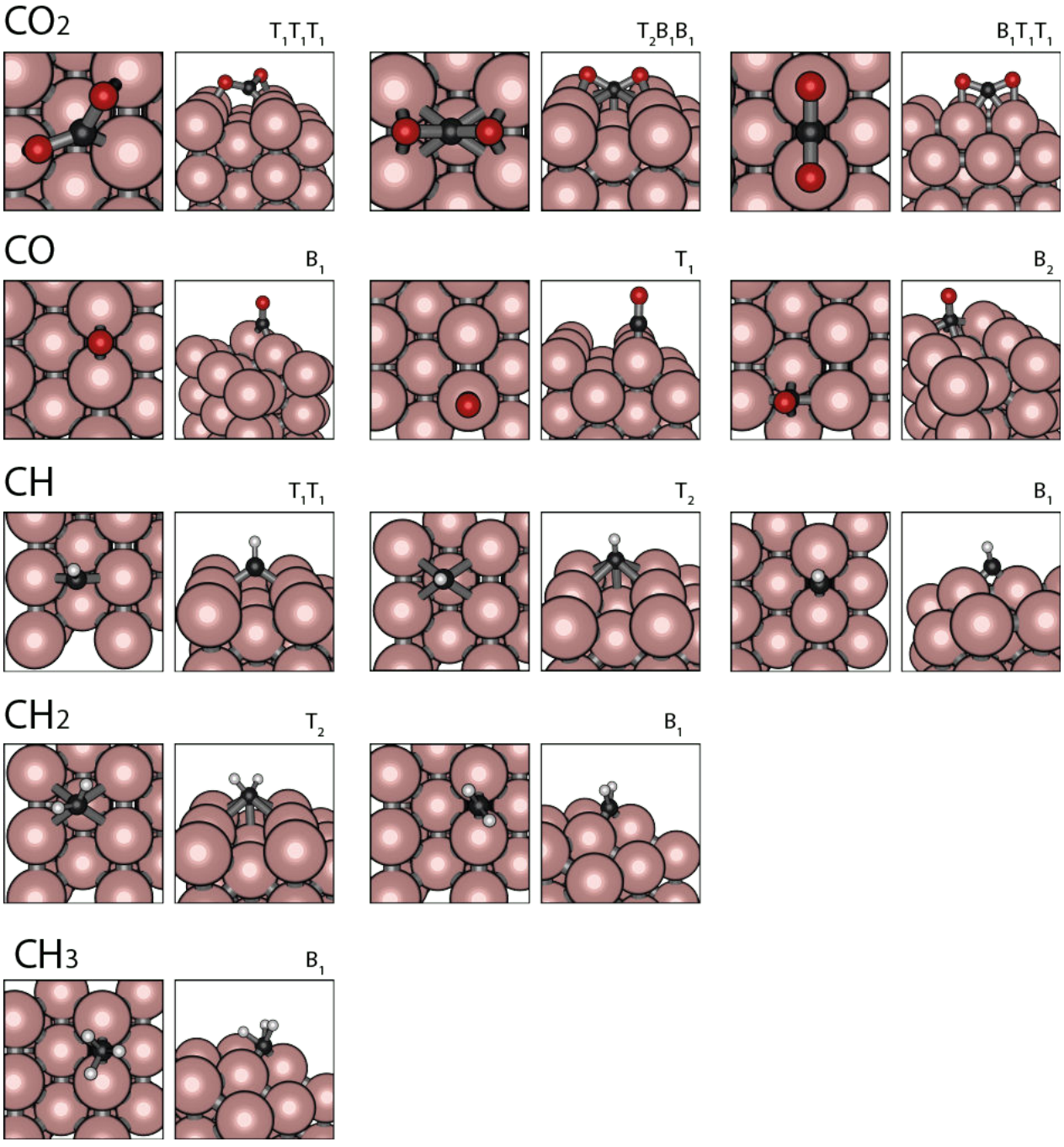
CO2
T1T1T1
T2B1B1
B1T1T1
CO
B1
T1
B2
CH
T1T1
T2
B1
CH2
T2
B1
CH3
B1

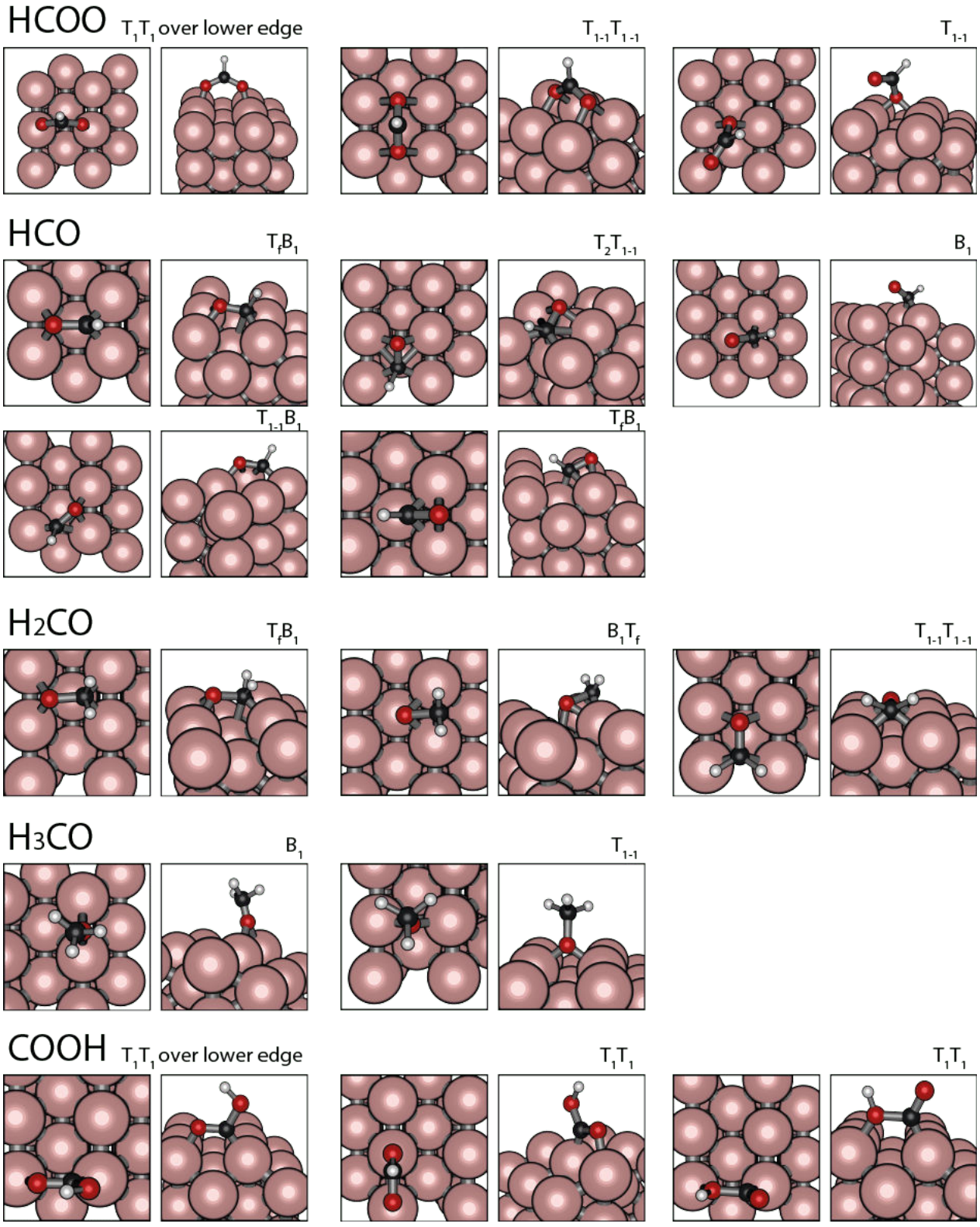
HCOO
T1T1 over lower edge
T1-1T1-1
T1-1
HCO
TfB1
T2T1-1
B1
T1-1B1
TfB1
H2CO
TfB1
B1Tf
T1-1T1-1
H3CO
B1
T1-1
COOH
T1T1 over lower edge
T1T1
T1T1

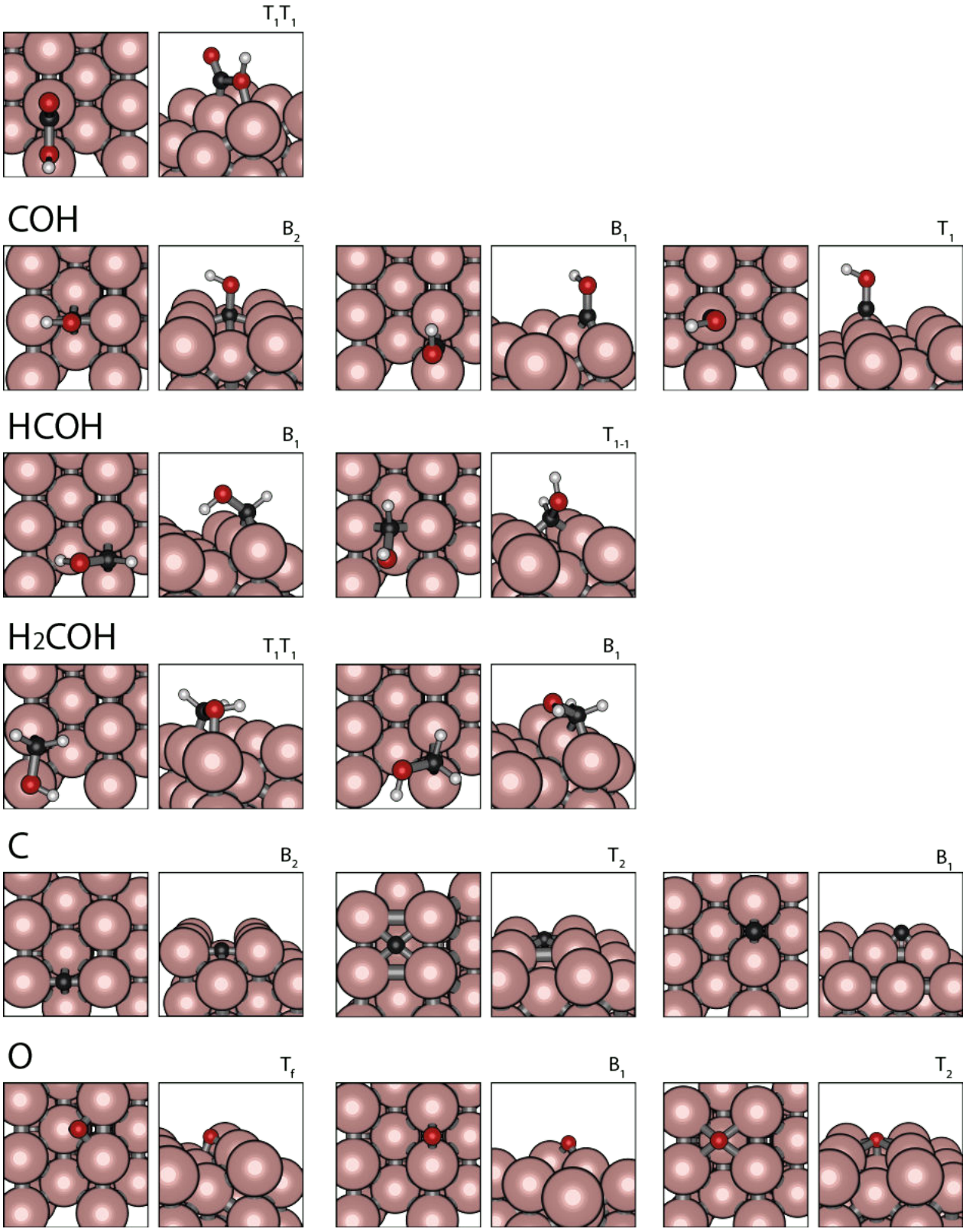
T1T1
COH
B2
B1
T1
HCOH
B1
T1-1
H2COH
T1T1
B1
C
B2
T2
B1
O
Tf
B1
T2

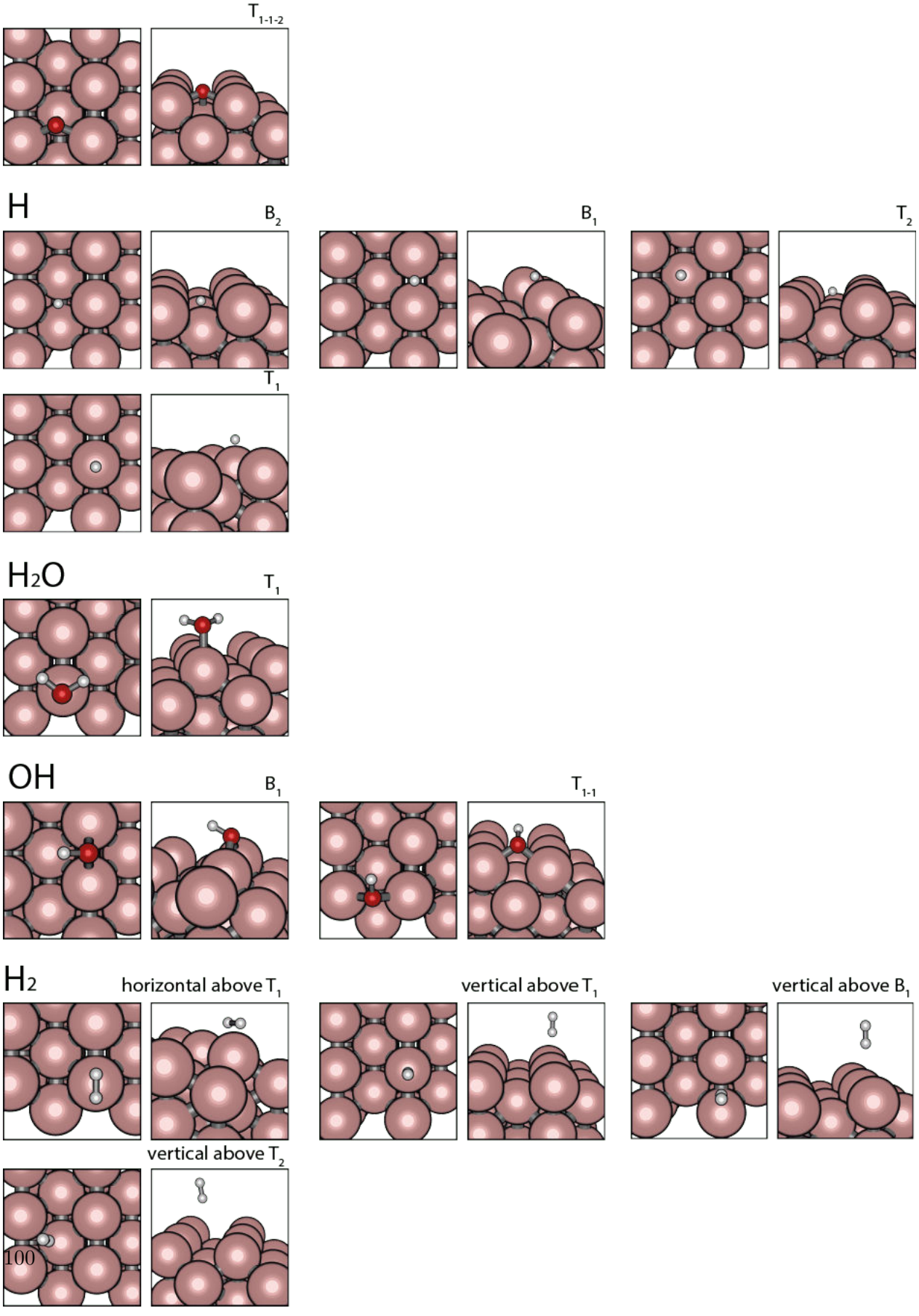
T1-1-2
H
B2
B1
T2
T1
H2O
T1
OH
B1
T1-1
H2
horizontal above T1
vertical above T1
vertical above B1
vertical above T2

CCO

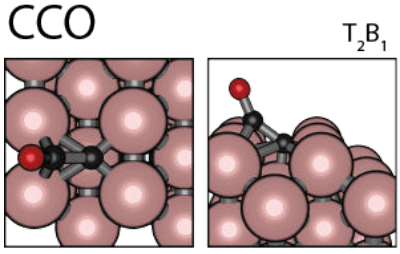

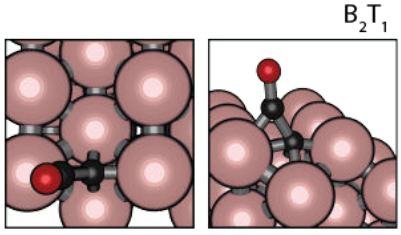

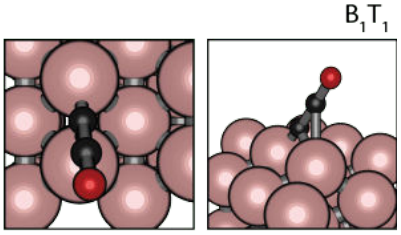

CCH

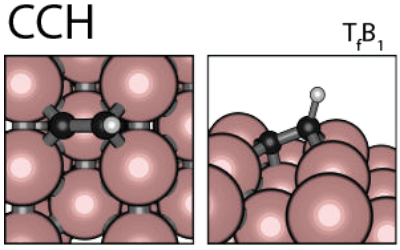

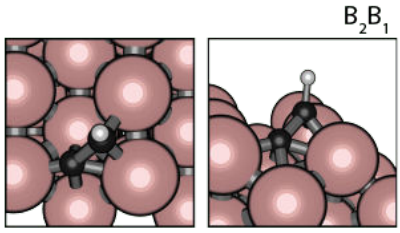

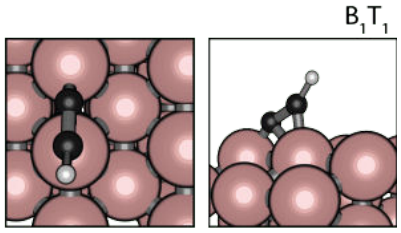

CCH_3

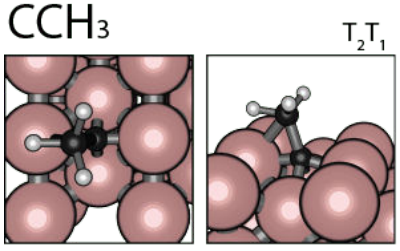

$CHCH_3$

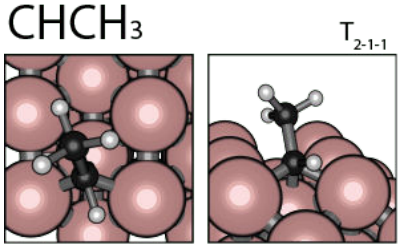

CH_2CH_3

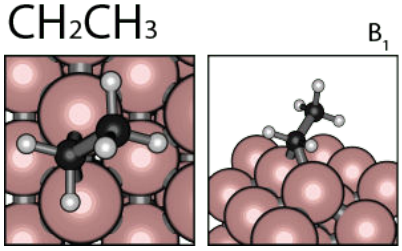

Ni(211)

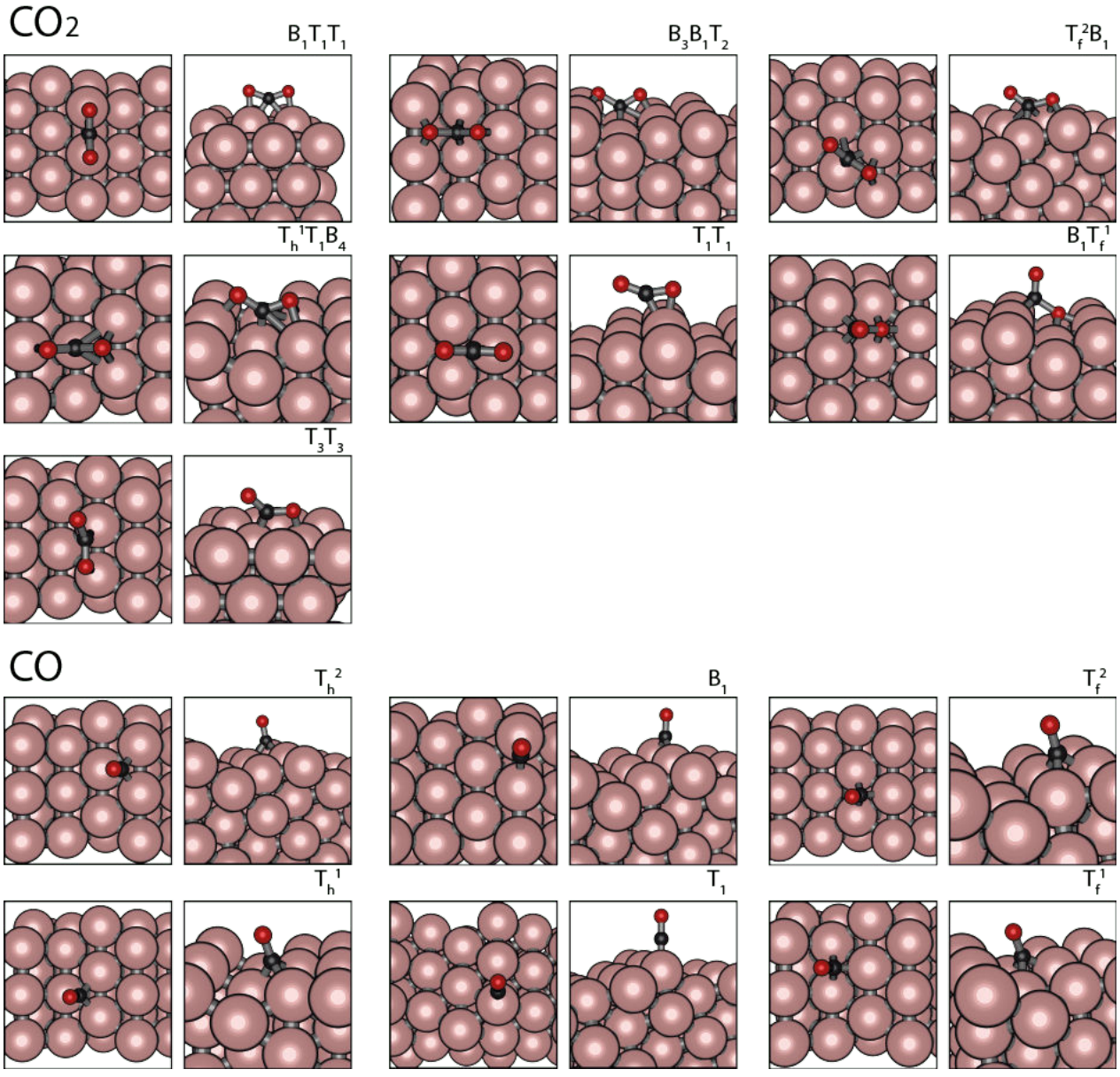
CO2
B1T1T1
B3B1T2
Tf2B1
Th1T1B4
T1T1
B1Tf1
T3T3
CO
Th2
B1
Tf2
Th1
T1
Tf1

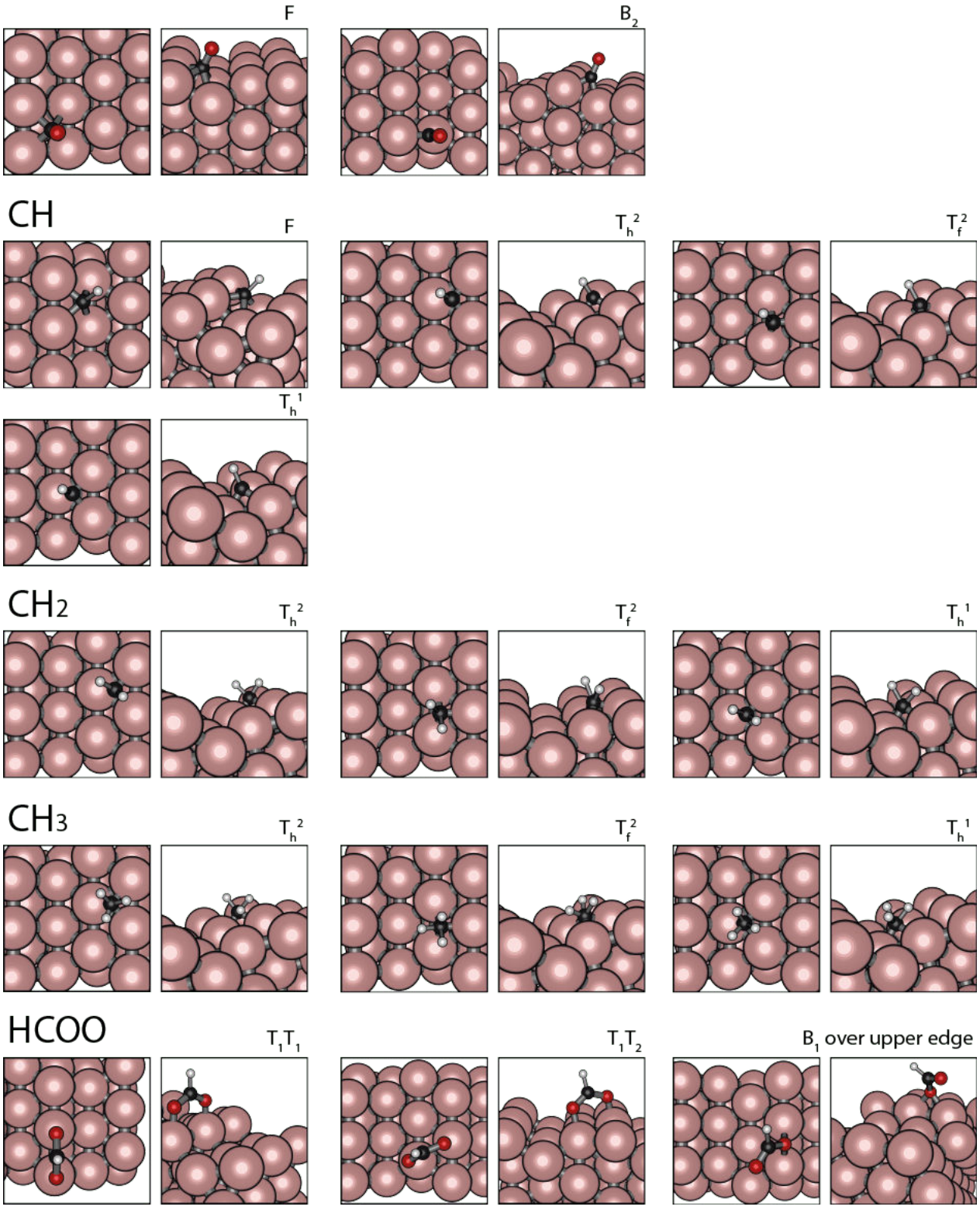
F
B2
CH
F
Th2
Tf2
Th1
CH2
Th2
Tf2
Th1
CH3
Th2
Tf2
Th1
HCOO
T1T1
T1T2
B1 over upper edge

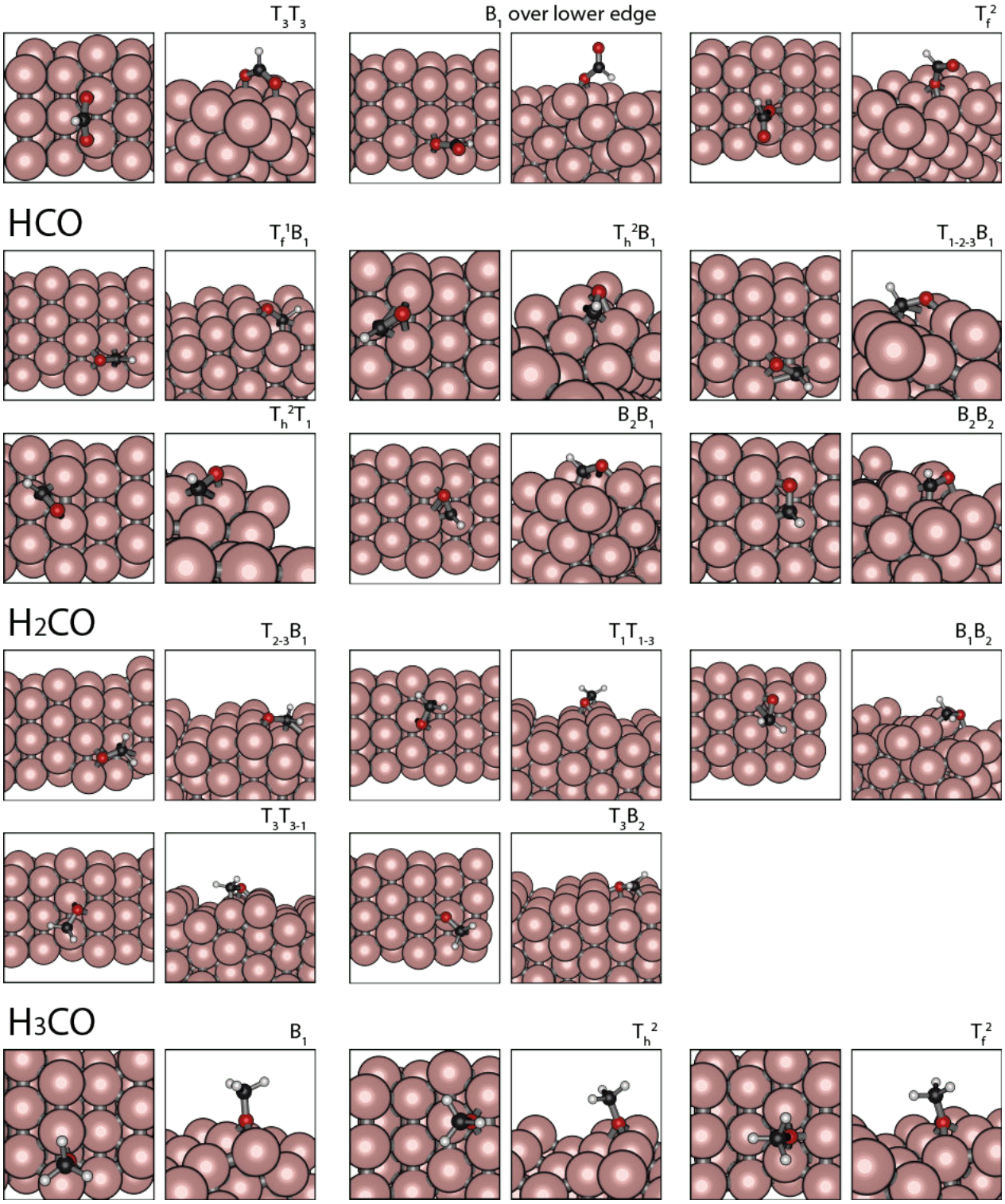
T3T3
B1 over lower edge
Tf2
HCO
Tf1B1
Th2B1
T1-2-3B1
Th2T1
B2B1
B2B2
H2CO
T2-3B1
T1T1-3
B1B2
T3T3-1
T3B2
H3CO
B1
Th2
Tf2

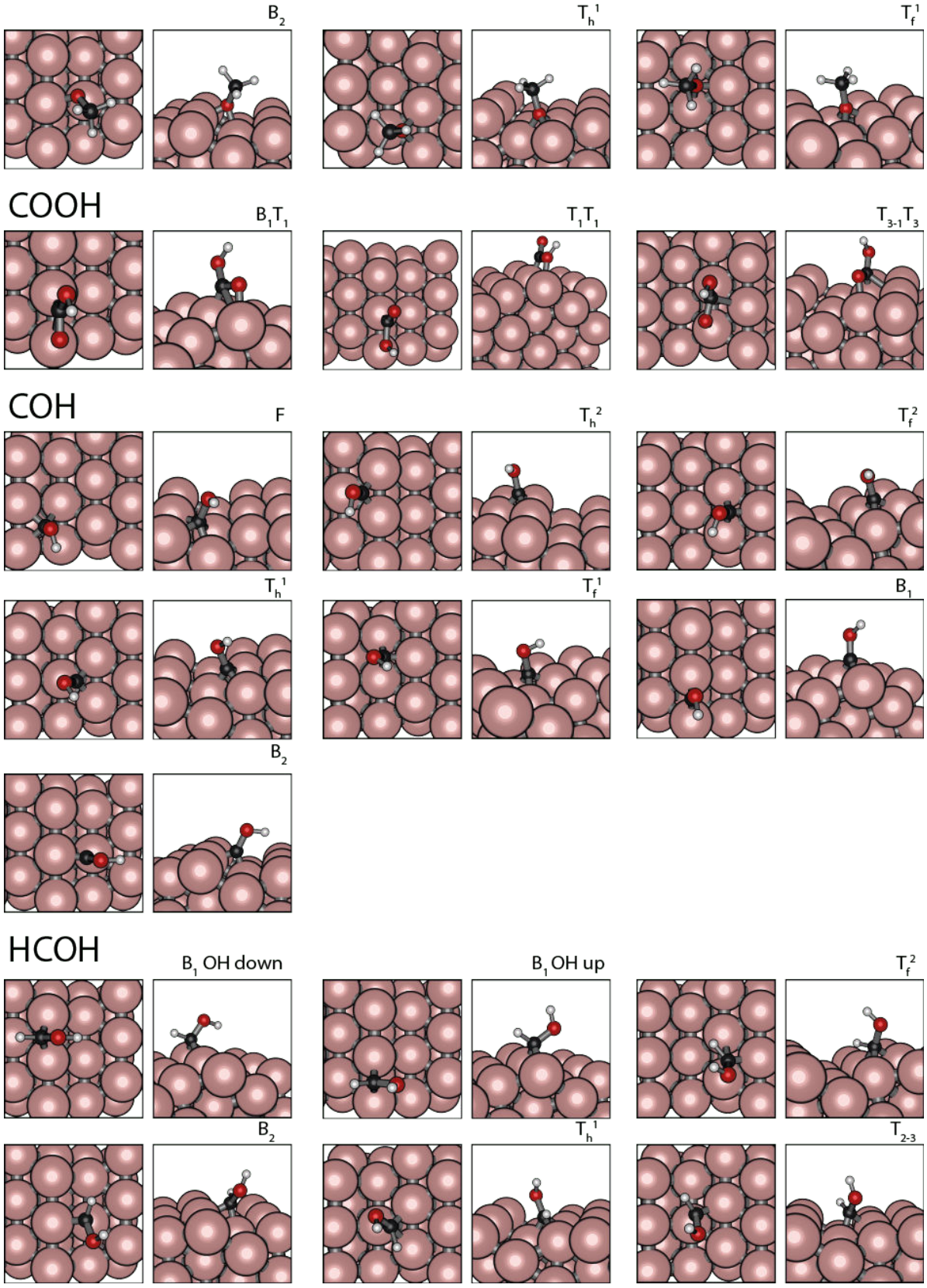
B2
Th1
Tf1
COOH
B1T1
T1T1
T3-1T3
COH
F
Th2
Tf2
Th1
Tf1
B1
B2
HCOH
B1 OH down
B1 OH up
Tf2
B2
Th1
T2-3

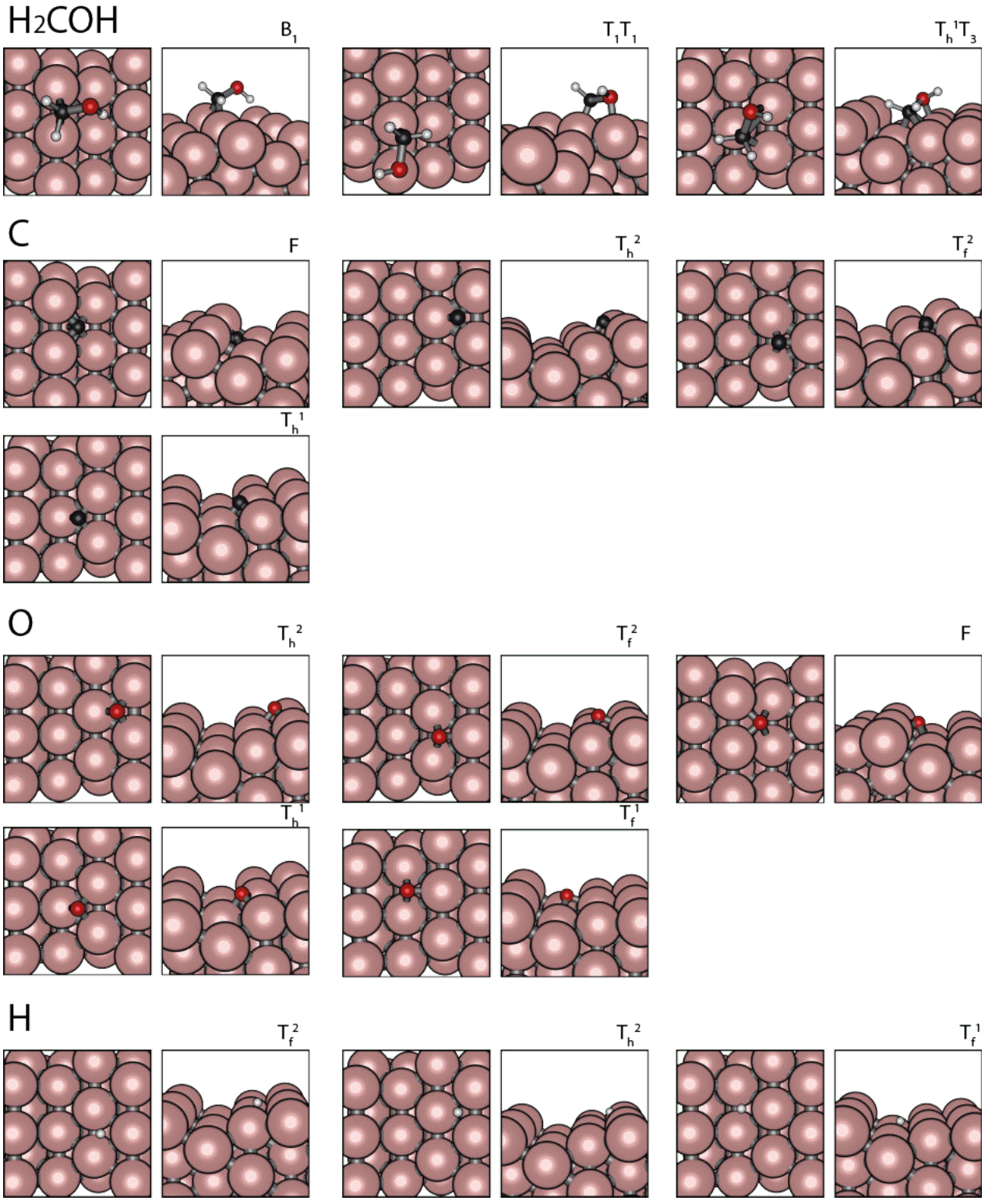
H2COH
B1
T1T1
ThT3
C
F
Th2
Tf2
Th1
O
Th2
Tf2
F
Th1
Tf1
H
Tf2
Th2
Tf1

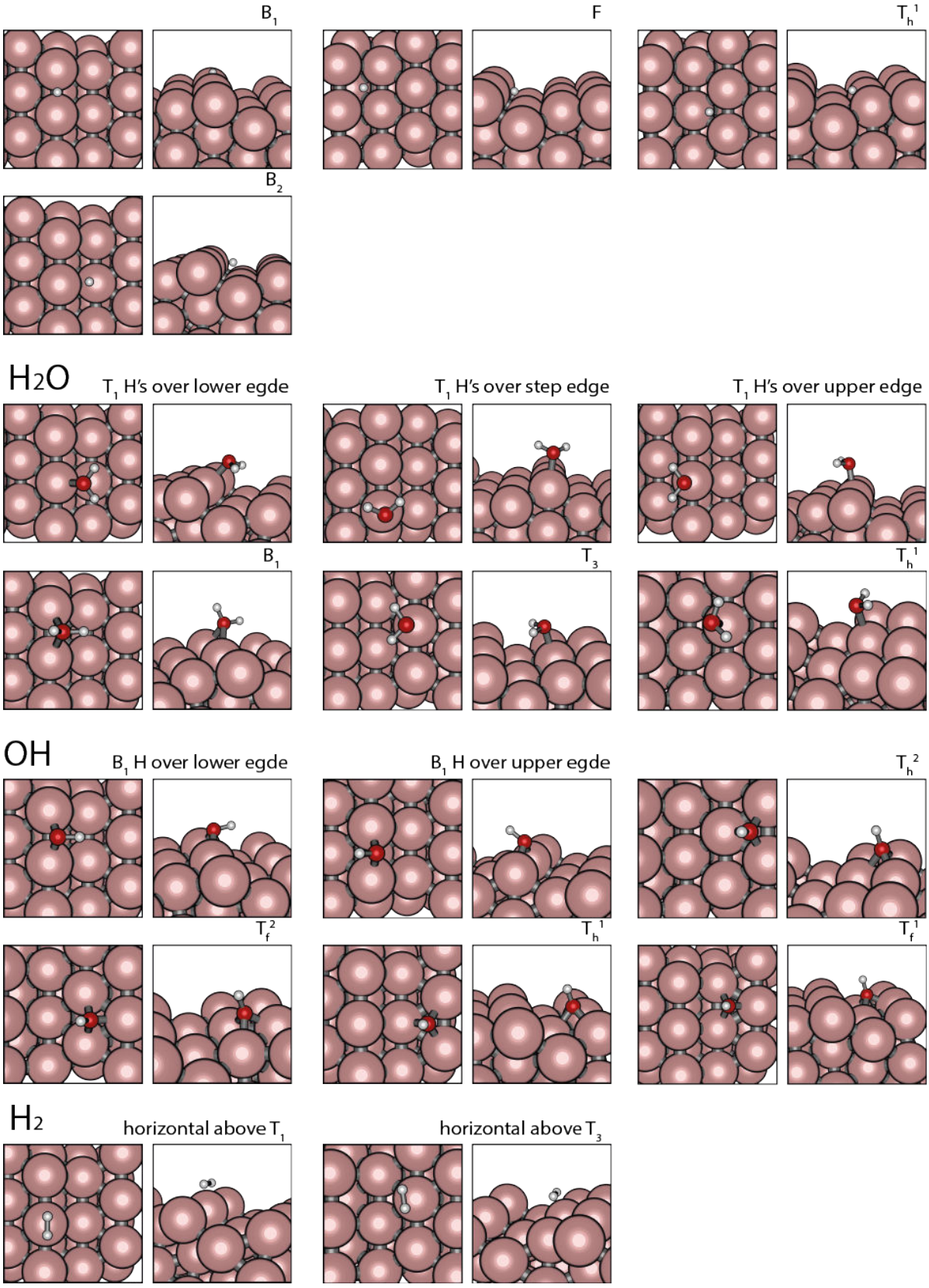
B1
F
Th1
B2
H2O
T1 H's over lower egde
T1 H's over step edge
T1 H's over upper edge
B1
T3
Th1
OH
B1 H over lower egde
B1 H over upper egde
Th2
Tf2
Th1
Tf1
H2
horizontal above T1
horizontal above T3

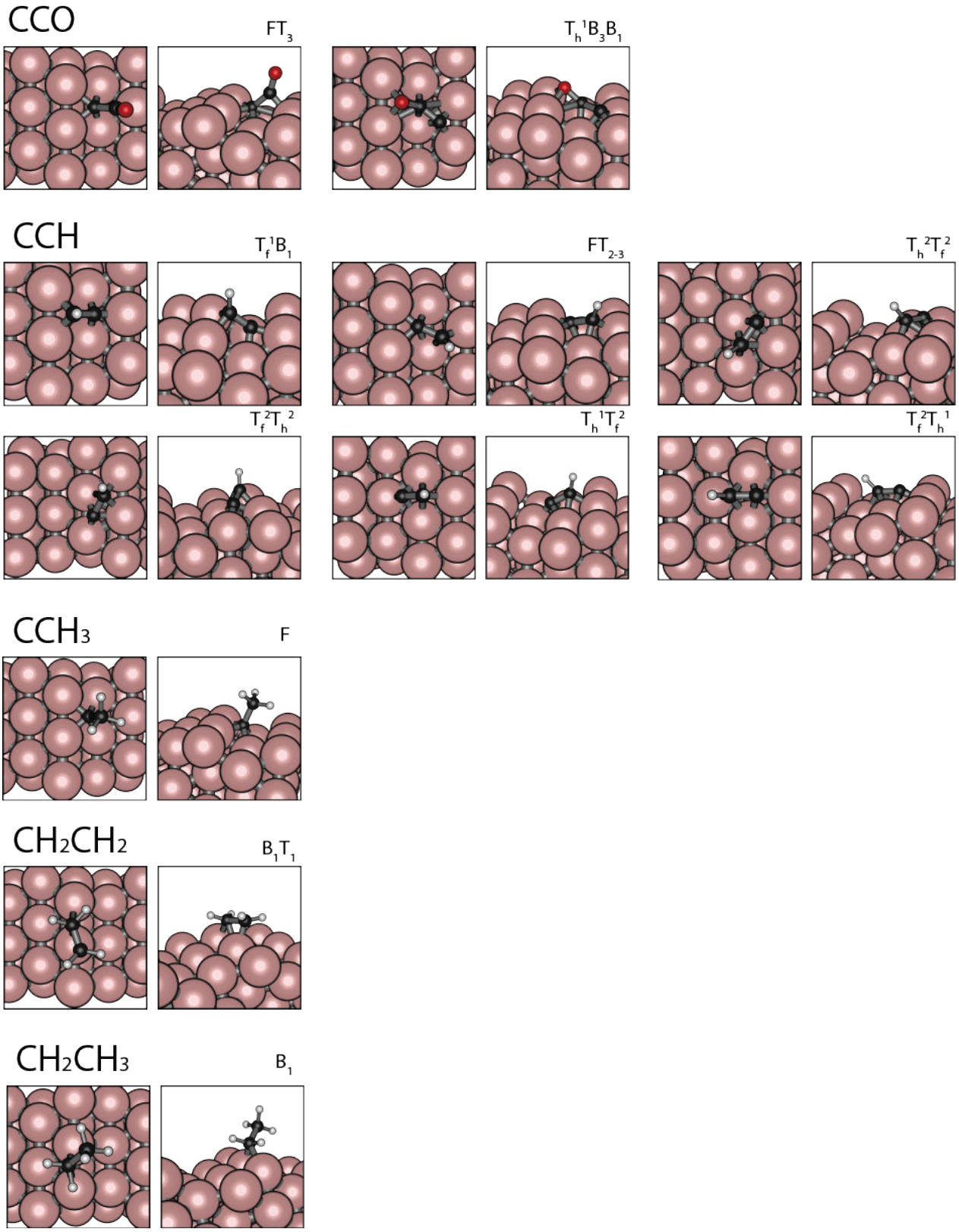
CCO
FT3
Th1B3B1
CCH
Tf1B1
FT2-3
Th2Tf2
Tf2Th2
Th1Tf2
Tf2Th1
CCH3
F
CH2CH2
B1T1
CH2CH3
B1

B Adsorption Energy Stable Geometries

Table B.1: Adsorption energy in kJ/mol of reaction intermediates on Ni(111).

Adsorbate	**Adsorption Site**	$\mathbf{E_{ads}}$	**Adsorbate**	**Adsorption Site**	$\mathbf{E_{ads}}$
CO_2	BTT	35.5	O	T_f	-692.4
	TT	26.6		T_h	-680.9
	T_fTT	24.3	H	T_f	-361.7
CO	T_h	-178.6		B	-361.6
	T_f	-178.1		T_h	-360.9
	B	-158.8		T	-310.6
	T	-144.3	H_2O	T	-22.5
CH	T_f	-603.3	OH	T_f	-364.9
	T_h	-600.5		T_h	-356.2
CH_2	T_f	-454.2		B	-352.1
	T_h	-449.7	H_2	Above B	11.6
CH_3	T_f	-238.3		Above T	11.3
	T_h	-235.8	CCO	T_f	-575.5
HCOO	TT	-277.3		T_h	-568.4
	T_f	-224.3	CCH	T_fT_h	-590.0
	T_h	-218.1		T_hT_f	-589.2
HCO	BT over fcc	-201.2		T_f	-510.0
	BT over hcp	-200.8		T_h	-503.7
	T	-165.9	CCH_3	T_h	-572.8
H_2CO	T_fT	-57.7	CH_2CH_2	T_fT	-72.8
	T_hT	-57.3	CH_2CH_3	B	-182.4
H_3CO	T_h	-218.0			
	T_f	-206.4			
COOH	BT over fcc	-210.9			
	TT	-210.8			
	BT over hcp	-209.5			
	TT	-188.7			
COH	T_h	-410.5			
	T_f	-410.4			
HCOH	T_h	-270.8			
H_2COH	BT over hcp	-146.7			
	BT over fcc	-145.5			
C	T_h	-773.8			
	T_f	-770.0			

Table B.2: Adsorption energy in kJ/mol of reaction intermediates on Ni(100).

Ni(100)					
Adsorbate	**Adsorption Site**	**E_{ads}**	**Adsorbate**	**Adsorption Site**	**E_{ads}**
CO_2	BTT	-16.3	OH	F	-388.4
	TT	-6.5		B	-381.6
CO	F	-174.8	H_2	Horizontal above T	-28.5
	B	-166.3		Vertical above T	-0.3
	T	-147.6		Vertical above B	1.5
CH	F	-667.6	CCO	FT	-636.1
CH_2	B	-436.8	CCH	FB	-652.7
CH_3	B	-233.8	CCH_3	F	-615.0
HCOO	TT over F	-293.8	CH_2CH_2	BT	-79.7
	BB	-292.6	CH_2CH_3	B	-200.0
	TT over B	-257.8			
	F	-240.9			
HCO	BB	-264.6			
H_2CO	BB	-127.9			
H_3CO	F	-251.9			
COOH	TT	-232.9			
	TT	-207.9			
COH	F	-447.5			
	B	-375.1			
HCOH	B	-285.2			
H_2COH	B	-159.4			
C	F	-909.4			
O	F	-724.2			
H	F	-364.5			
	B	-350.5			
	T	-311.6			
H_2O	T	-31.1			

Table B.3: Adsorption energy in kJ/mol of reaction intermediates on Ni(110).

Ni(110)					
Adsorbate	**Adsorption Site**	**E_{ads}**	**Adsorbate**	**Adsorption Site**	**E_{ads}**
CO_2	$T_1T_1T_1$	-41.9	H_2COH	T_1T_1	-173.6
	$T_2B_1B_1$	-38.9		B_1	-166.9
	$B_1T_1T_1$	-35.0	C	B_2	-836.1
CO	B_1	-174.5		T_2	-819.0
	T_1	-157.3		B_1	-699.6
	B_2	-145.6	O	T_f	-676.4
CH	T_1T_1	-613.7		B_1	-671.2
	T_2	-600.7		T_2	-654.5
	B_1	-522.7		T_{1-1-2}	
CH_2	T_2	-452.9	H	B_2	-351.6
	B_1	-442.2		B_1	-349.1
CH_3	B_1	-252.2		T_2	-341.6
HCOO	T_1T_1 over lower edge	-327.8		T_1	-308.8
	$T_{1-1}T_{1-1}$	-251.8	H_2O	T_1	-38.5
	T_{1-1}	-229.3	OH	B_1	-398.6
HCO	T_fB_1	-239.6		T_{1-1}	-358.1
	T_2T_{1-1}	-217.2	H_2	horizontal above T_1	-1.2
	B_1	-206.5		vertical above T_1	1.3
	$T_{1-1}B_1$	-200.8		vertical above B_1	0.4
	T_fB_1	-176.0		vertical above T_2	-62.4
H_2CO	T_fB_1	-190.3	CCO	T_2B_1	-1715.8
	B_1T_f	-164.3		B_2T_1	-1702.0
	$T_{1-1}T_{1-1}$	-138.1		B_1T_1	-1628.3
H_3CO	B_1	-259.5	CCH	T_fB_1	-283.4
	T_{1-1}	-211.6		B_2B_1	-254.4
COOH	T_{1-1} over lower edge	-248.1		B_1T_1	-172.2
	T_{1-1}	-247.7	CCH_3	T_2T_1	-555.7
	T_{1-1}	-229.6	$CHCH_3$	T_{2-1-1}	*
	T_{1-1}	-224.6	CH_2CH_3	B_1	-220.1
COH	B_2	-378.9			
	B_1	-362.0			
	T_1	-251.3			
HCOH	B_1	-317.3			
	T_{1-1}	-250.0			

* Calculation of reference frequency of $CHCH_3$ in vacuum did not succeed, due to isomerization of $CHCH_3$ to CH_2CH_2.

Table B.4: Adsorption energy in kJ/mol of reaction intermediates on Ni(211).

Ni(211) part 1					
Adsorbate	**Adsorption Site**	**E_{ads}**	**Adsorbate**	**Adsorption Site**	**E_{ads}**
CO_2	$B_1T_1T_1$	-39.1		B_1B_2	-71.2
	$B_3B_1T_2$	-39.0		T_3T_{3-1}	-70.7
	$T_f^2B_1$	-20.9		T_3B_2	-55.2
	$T_h^1T_1B_4$	-14.8	H_3CO	B_1	-269.1
	T_1T_1	4.6		T_h^2	-256.1
	$B_1T_f^1$	10.3		T_f^2	-233.2
	T_2T_2	17.8		B_2	-208.2
CO	T_h^2	-186.7		T_h^1	-204.7
	B_1	-182.5		T_f^1	-187.7
	T_f^2	-177.2	COOH	B_1T_1	-257.0
	T_h^1	-172.9		T_1T_1	-229.3
	T_1	-165.0		$T_{3-1}T_3$	-202.5
	T_f^1	-160.3	COH	F	-415.6
	F	-159.2		T_h^2	-413.0
	B_2	-154.2		T_f^2	-401.0
CH	F	-634.2		T_h^1	-397.8
	T_h^2	-603.0		T_f^1	-388.0
	T_f^2	-592.2		B_1	-374.1
	T_h^1	-590.3		B_2	-362.0
CH_2	T_h^2	-467.8	HCOH	B_1 OH down	-314.4
	T_f^2	-4439		B_1 OH up	-302.9
	T_h^1	-438.8		T_f^2	-270.4
CH_3	T_h^2	-265.6		B_2	-267.9
	T_f^2	-258.8		T_h^1	-262.2
	T_h^1	-211.6		T_{2-3}	-255.1
HCOO	T_1T_1	-340.6	H_2COH	B_1	-192.6
	T_1T_2	-301.6		T_1T_1	-189.5
	B_1 over upper edge	-278.6		$T_h^1T_3$	-137.0
	T_3T_3	-269.0	C	F	-874.1
	B_1 over lower edge	-264.2		T_h^2	-786.8
	T_F^2	-224.8		T_f^1	-762.1
HCO	$T_f^1B_1$	-248.2		T_h^1	-761.1
	$T_h^2B_1$	-237.0	O	T_h^2	-711.4
	$T_{1-2-3}B_1$	-227.4		T_f^2	-686.5
	$T_h^2T_1$	-227.2		F	-680.7
	B_2B_1	-224.2		T_h^1	-663.4
	B_2B_2	-219.2		T_f^1	-661.8
H_2CO	$T_{2-3}B_1$	-90.3	H	T_f^2	-363.7
	T_1T_{1-3}	-86.6			

Table B.5: Adsorption energy in kJ/mol of reaction intermediates on Ni(211).

Ni(211) part 2					
Adsorbate	**Adsorption Site**	**E_{ads}**	**Adsorbate**	**Adsorption Site**	**E_{ads}**
H	T_h^2	-359.2		T_h^1	-335.4
	T_f^1	-358.4		T_f^1	-323.0
	B_1	-356.5	H_2	horizontal above T_1	-38.9
	F	-354.4		horizontal above T_3	-12.9
	T_h^1	-354.3	CCO	FT_3	-609.7
	B_2	-342.0		$T_h^1B_3B_1$	-554.6
H_2O	T_1 H's over lower edge	-48.5	CCH	$T_f^1B_1$	-659.8
	T_1 H's over step edge	-41.0		FT_{2-3}	-635.1
	T_1 H's over upper edge	-40.3		$T_h^2T_f^2$	-604.7
	B_1	-37.2		$T_f^2T_h^2$2	-594.2
	T_3 H's over lower edge	-27.4		$T_h^1T_f^2$	-575.3
	T_3 H's over upper edge	-14.1		$T_f^2T_h^1$	-572.7
OH	B_1 H over lower edge	-415.0	CCH_3	F	-580.0
	B_1 H over upper egde	-412.5	CH_2CH_2	B_1T_1	-119.5
	T_h^2	-388.0	CH_2CH_3	B_1	-26.0
	T_f^2	-363.7			

C Geometries of Elementary Reaction Steps

The geometries of the initial- transition- and final states of the elementary reaction steps relevant in CO_2 hydrogenation over nickel are shown in this Appendix.

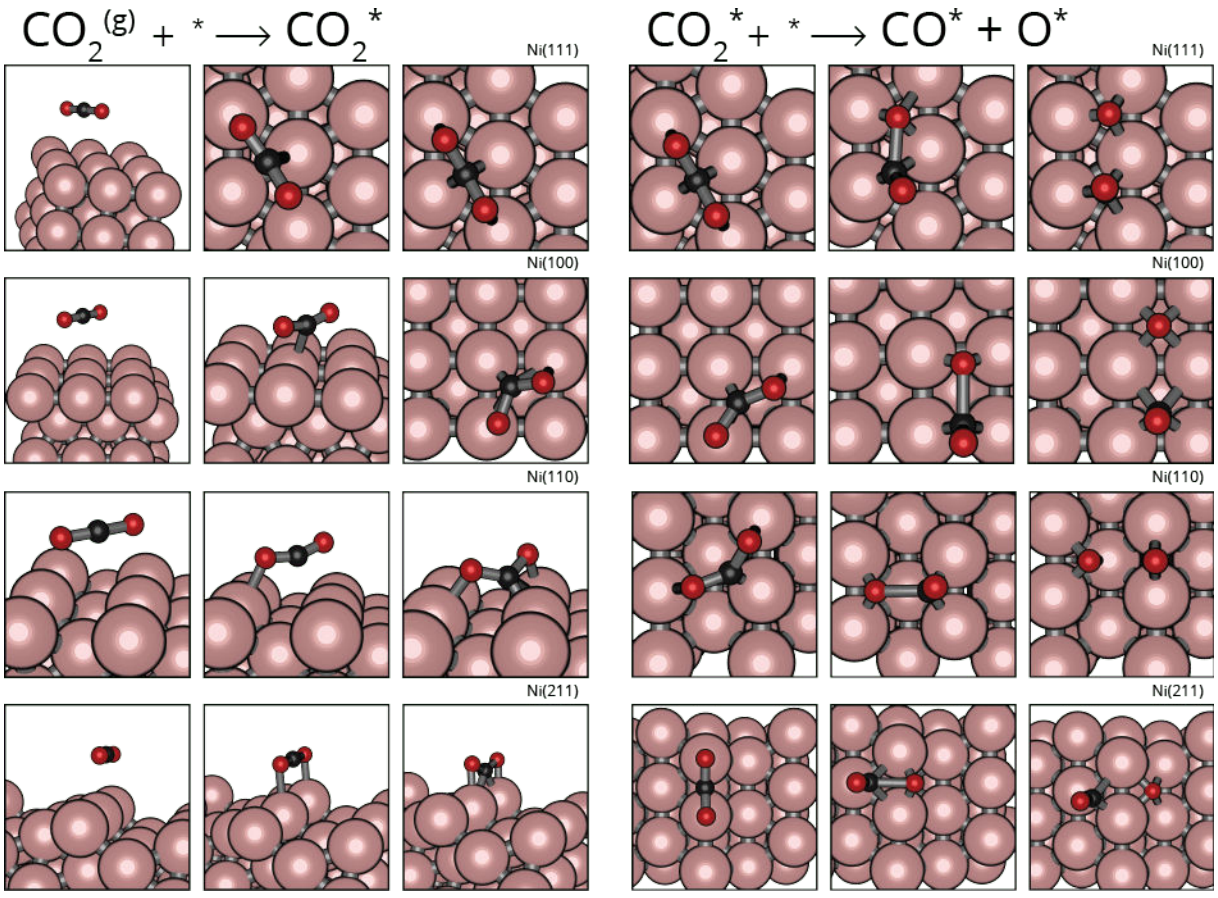

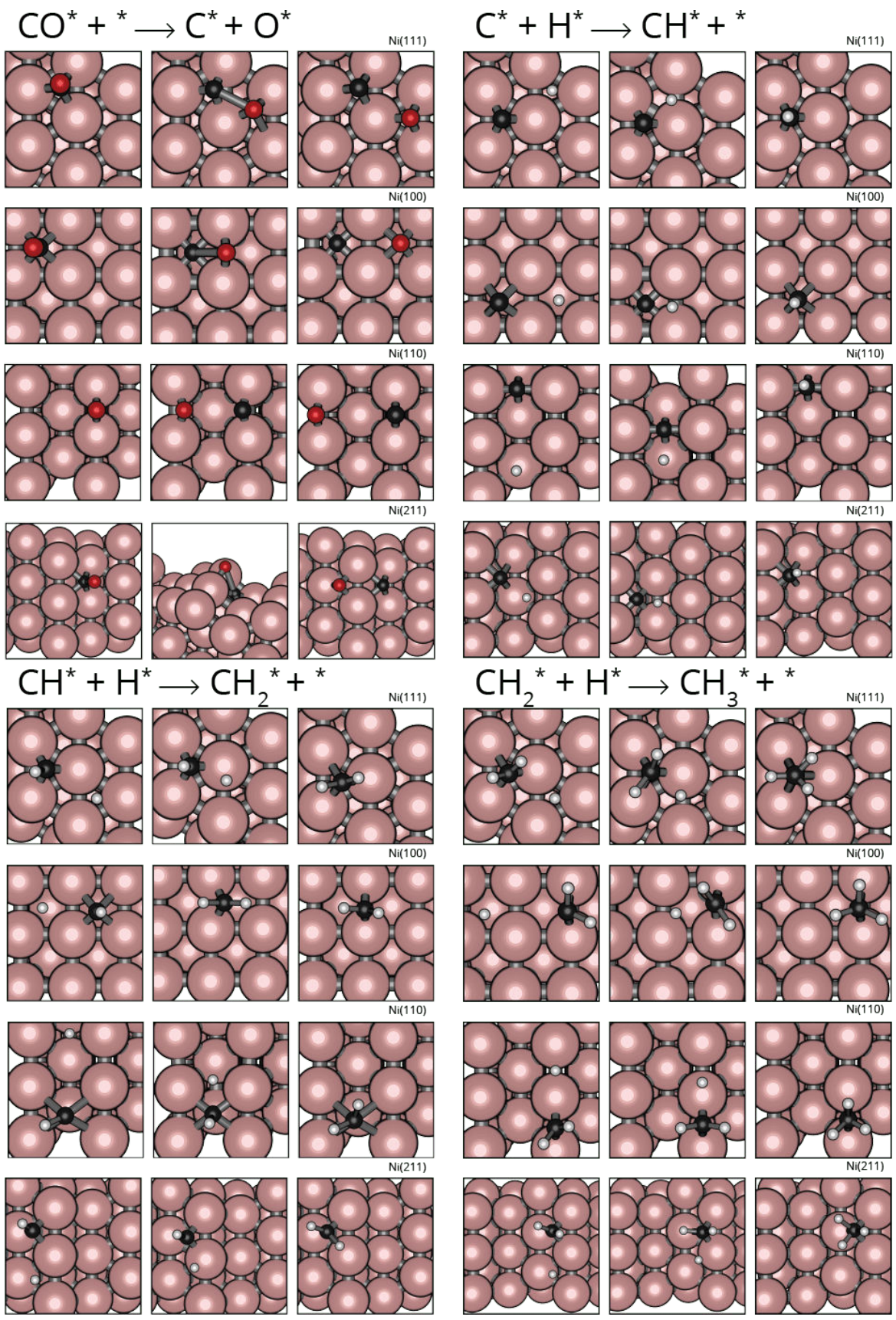
CO* + * ⟶ C* + O*
C* + H* ⟶ CH* + *
CH* + H* ⟶ CH2* + *
CH2* + H* ⟶ CH3* + *
Ni(111)
Ni(100)
Ni(110)
Ni(211)

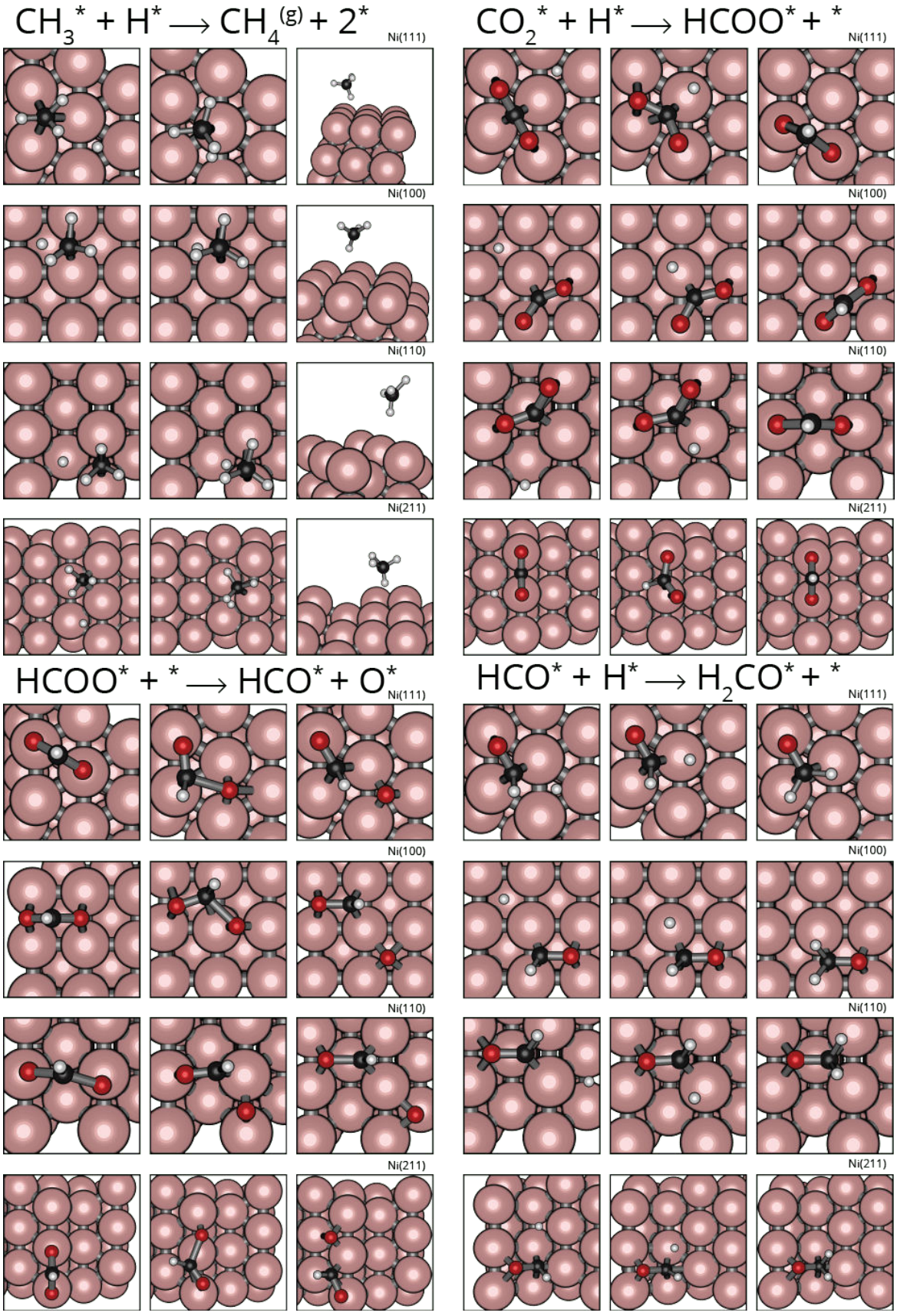
CH3* + H* ⟶ CH4(g) + 2*
CO2* + H* ⟶ HCOO* + *
HCOO* + * ⟶ HCO* + O*
HCO* + H* ⟶ H2CO* + *
Ni(111)
Ni(100)
Ni(110)
Ni(211)

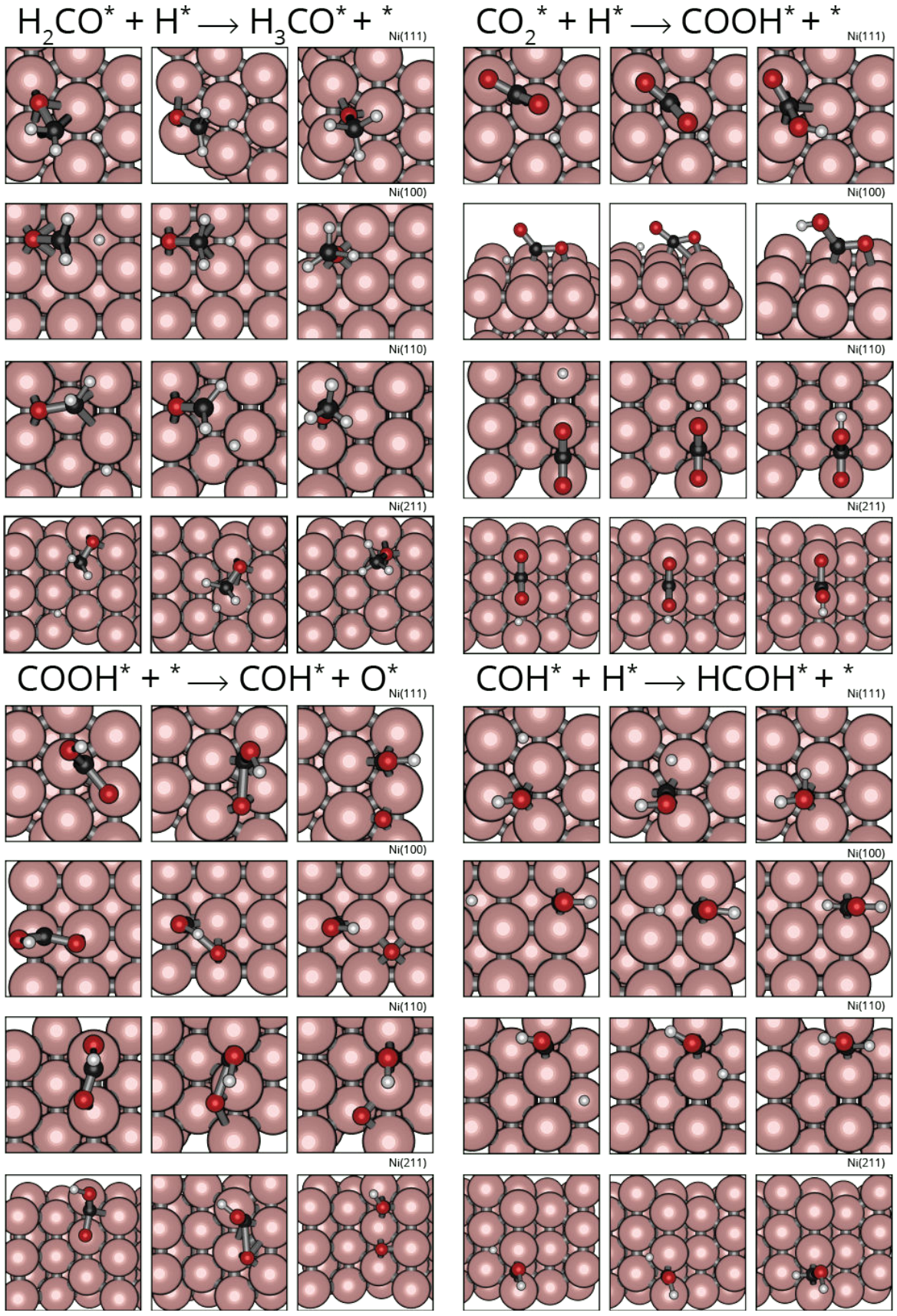
$H_2CO^* + H^* \longrightarrow H_3CO^* + *$
$CO_2^* + H^* \longrightarrow COOH^* + *$
$COOH^* + * \longrightarrow COH^* + O^*$
$COH^* + H^* \longrightarrow HCOH^* + *$
Ni(111)
Ni(100)
Ni(110)
Ni(211)

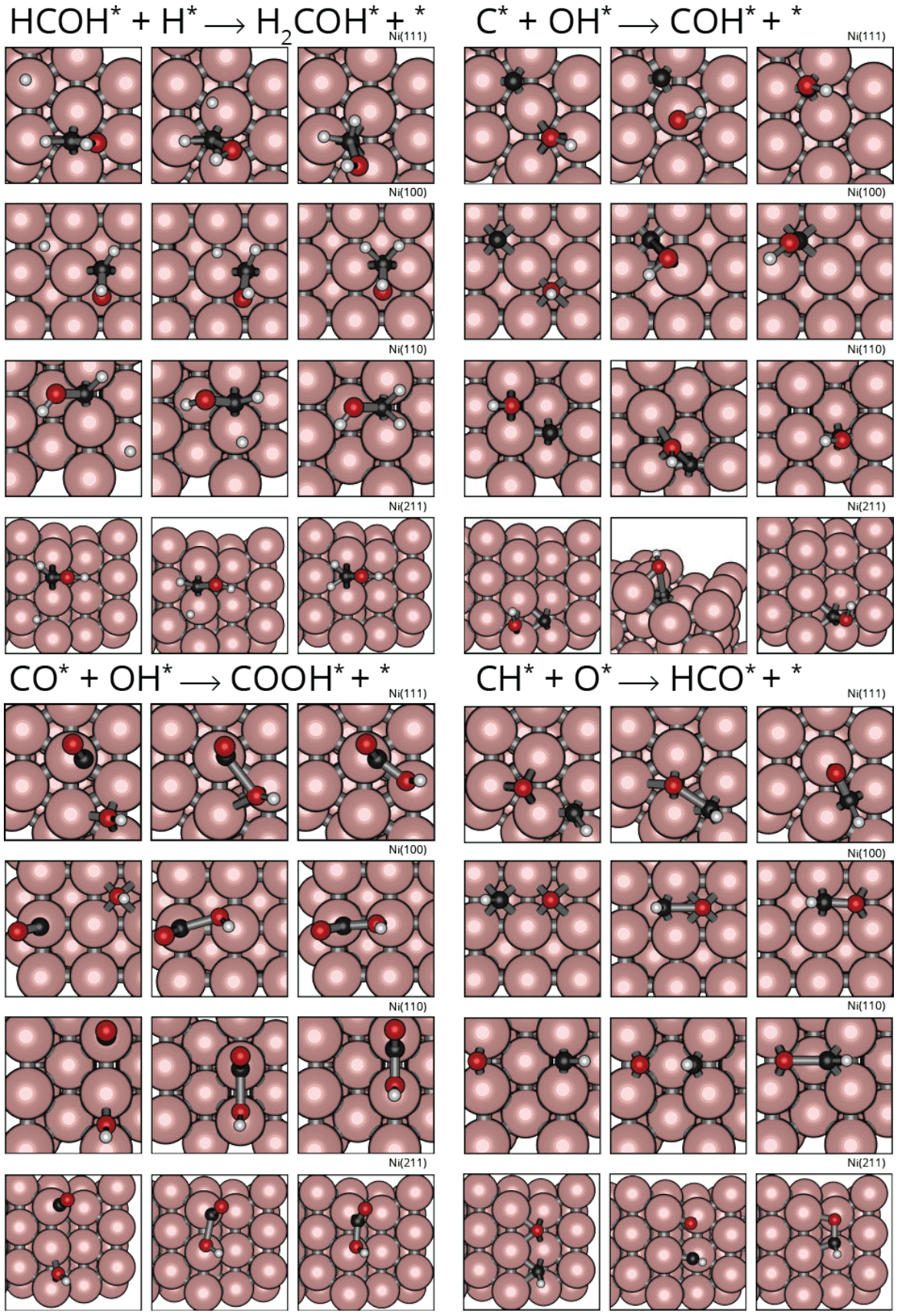
HCOH* + H* ⟶ H2COH* + *
C* + OH* ⟶ COH* + *
CO* + OH* ⟶ COOH* + *
CH* + O* ⟶ HCO* + *
Ni(111)
Ni(100)
Ni(110)
Ni(211)

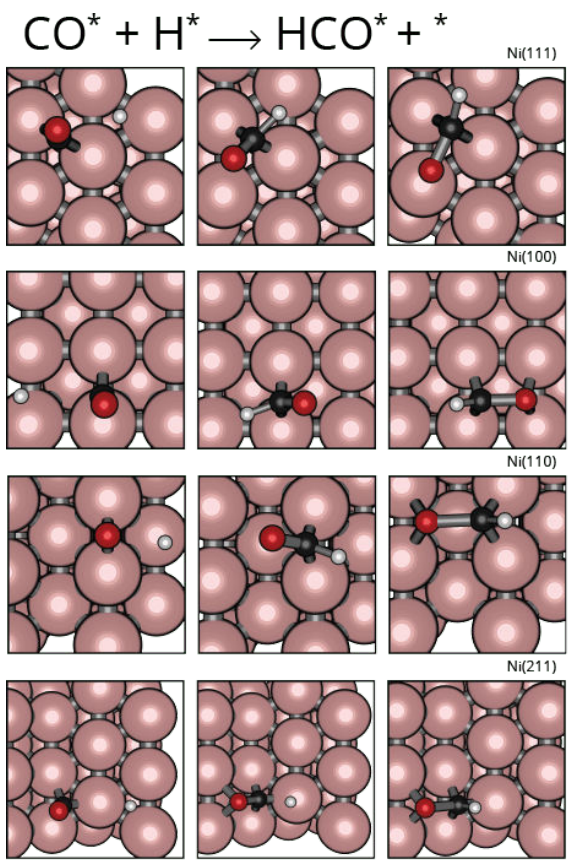
CO* + H* ⟶ HCO* + *
Ni(111)
Ni(100)
Ni(110)
Ni(211)

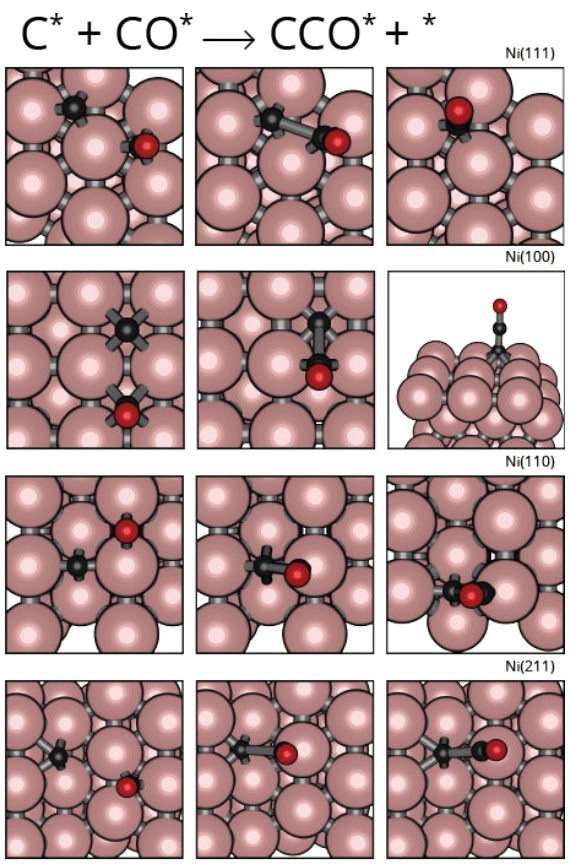
C* + CO* ⟶ CCO* + *
Ni(111)
Ni(100)
Ni(110)
Ni(211)

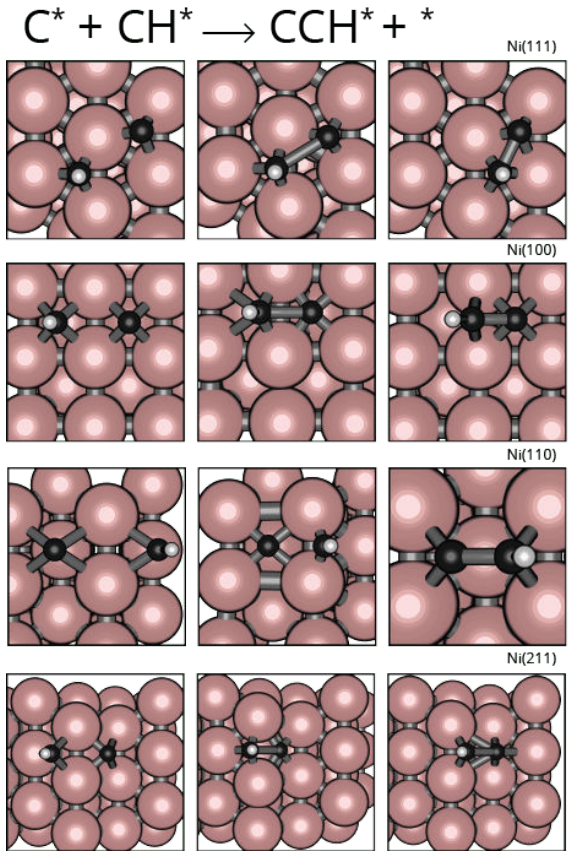
C* + CH* ⟶ CCH* + *
Ni(111)
Ni(100)
Ni(110)
Ni(211)

D Density of States $CO_2^* \rightarrow CO^* + O^*$

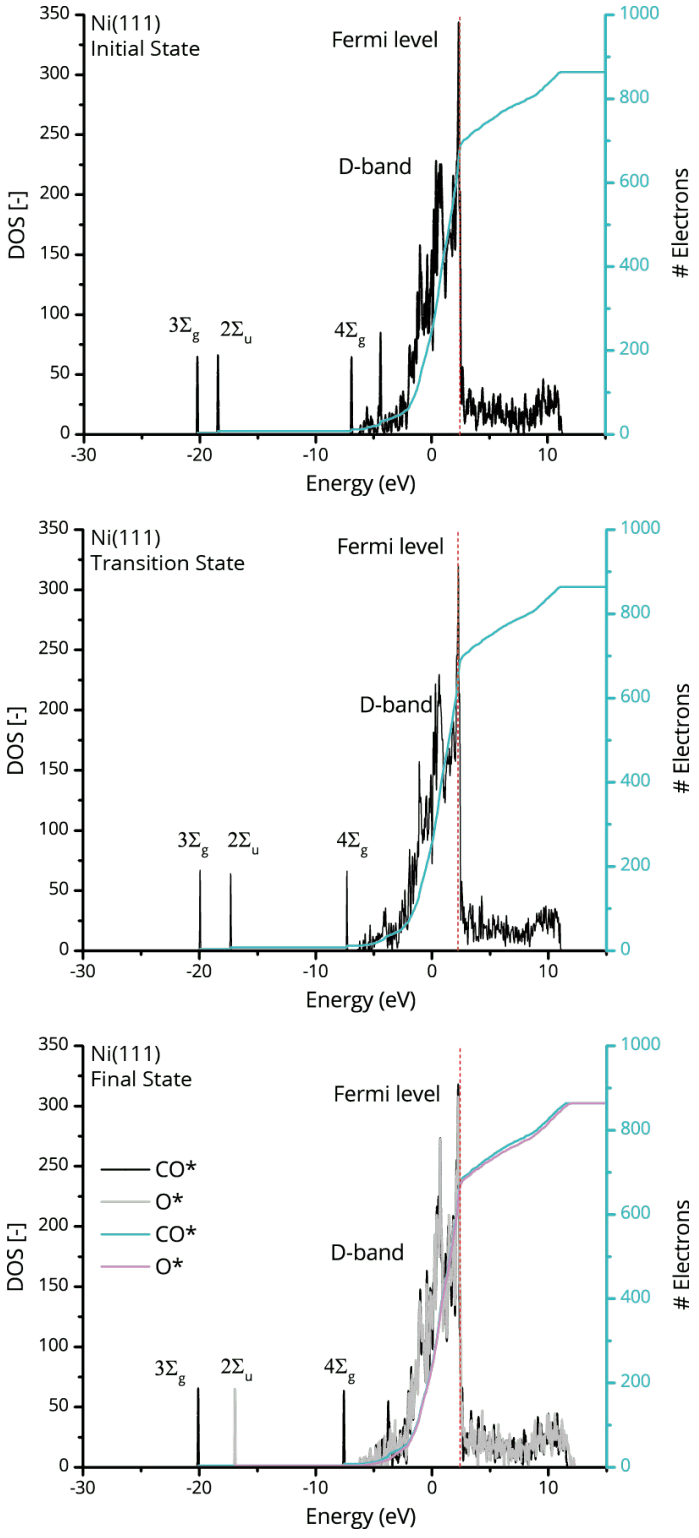

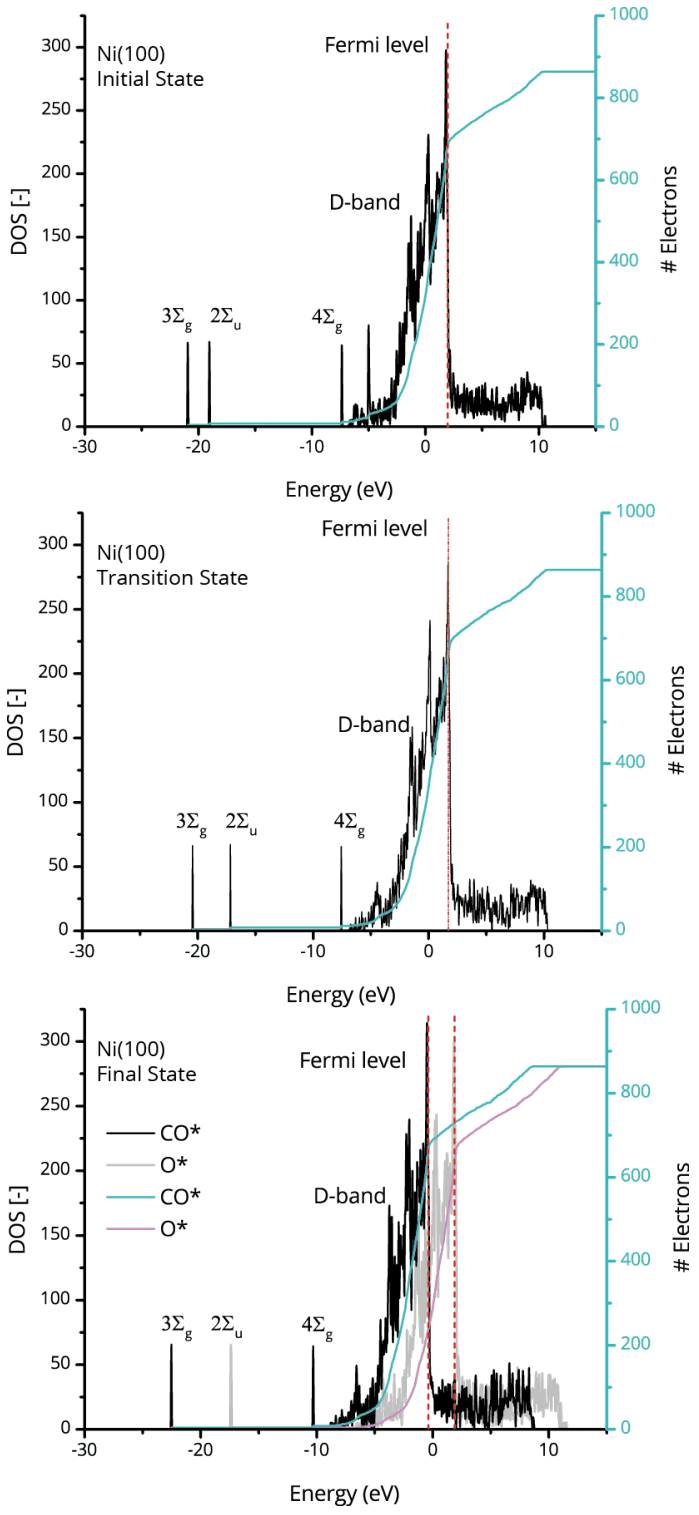
Ni(100)
Initial State
Fermi level
D-band
$3\Sigma_g$
$2\Sigma_u$
$4\Sigma_g$
DOS [-]
Electrons
Energy (eV)
Ni(100)
Transition State
Fermi level
D-band
$3\Sigma_g$
$2\Sigma_u$
$4\Sigma_g$
DOS [-]
Electrons
Energy (eV)
Ni(100)
Final State
Fermi level
CO*
O*
CO*
O*
D-band
$3\Sigma_g$
$2\Sigma_u$
$4\Sigma_g$
DOS [-]
Electrons
Energy (eV)

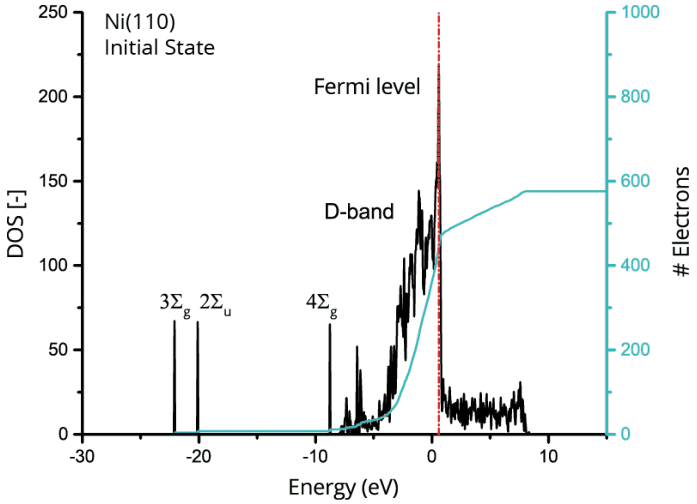
Ni(110)
Initial State
Fermi level
D-band
$3\Sigma_g$ $2\Sigma_u$
$4\Sigma_g$
DOS [-]
Electrons
Energy (eV)

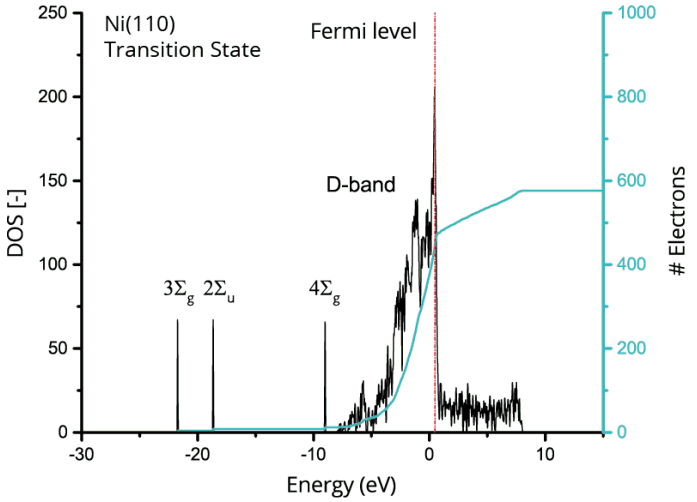
Ni(110)
Transition State
Fermi level
D-band
$3\Sigma_g$ $2\Sigma_u$
$4\Sigma_g$
DOS [-]
Electrons
Energy (eV)

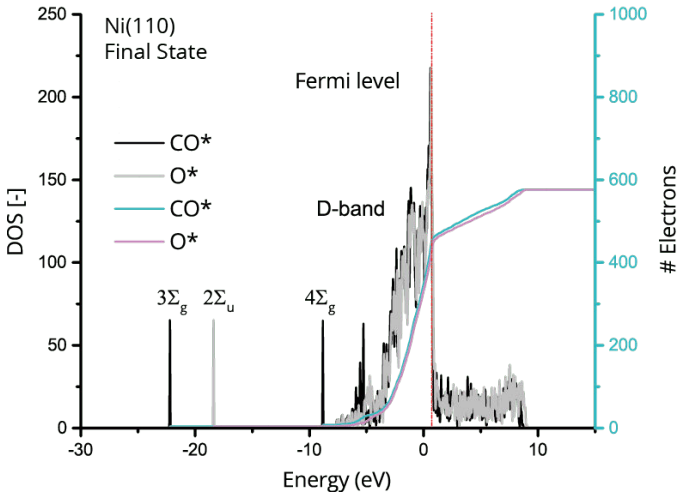
Ni(110)
Final State
Fermi level
CO*
O*
CO*
O*
D-band
$3\Sigma_g$ $2\Sigma_u$
$4\Sigma_g$
DOS [-]
Electrons
Energy (eV)

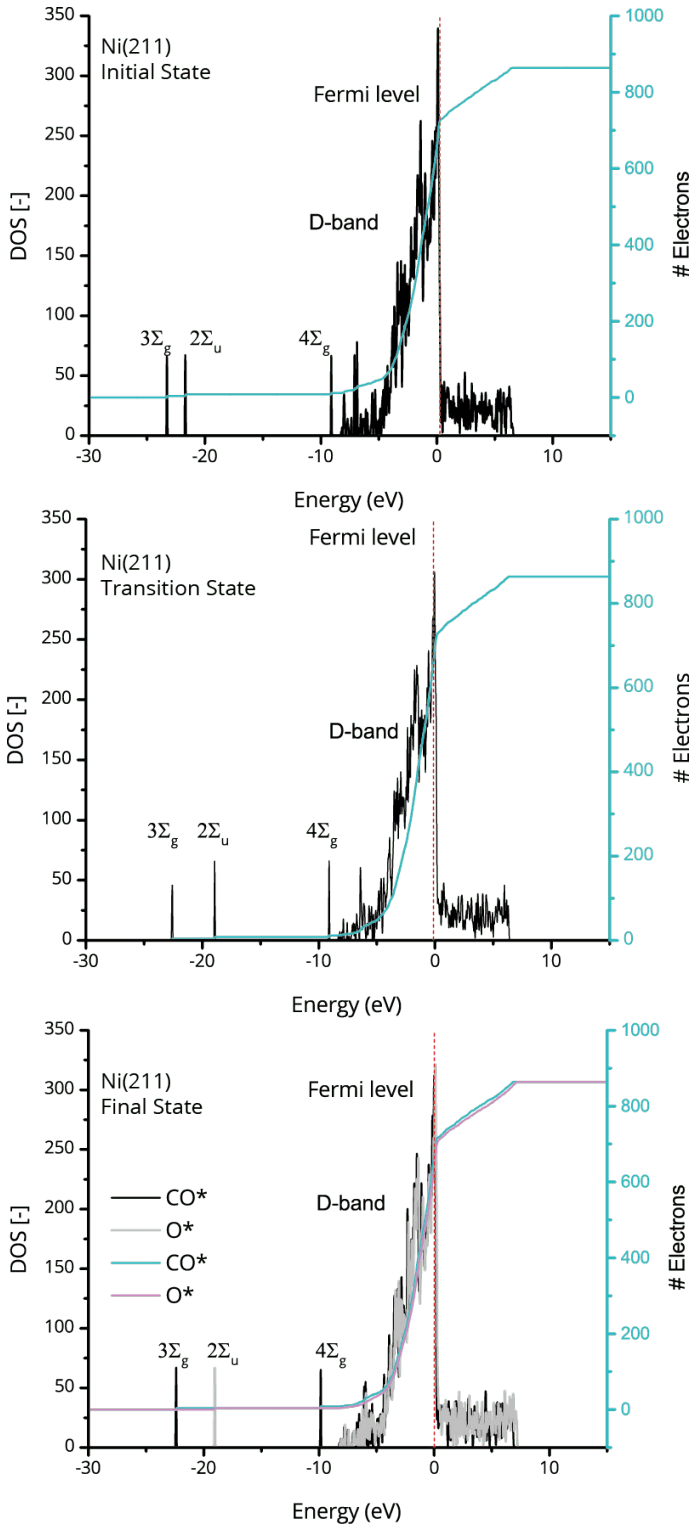
Ni(211)
Initial State
Fermi level
D-band
$3\Sigma_g$ $2\Sigma_u$
$4\Sigma_g$
DOS [-]
Electrons
Energy (eV)
Ni(211)
Transition State
Fermi level
D-band
$3\Sigma_g$ $2\Sigma_u$
$4\Sigma_g$
DOS [-]
Electrons
Energy (eV)
Ni(211)
Final State
Fermi level
D-band
CO*
O*
CO*
O*
$3\Sigma_g$ $2\Sigma_u$
$4\Sigma_g$
DOS [-]
Electrons
Energy (eV)

E Electron Density Plots $CO_2^{\ddagger}$

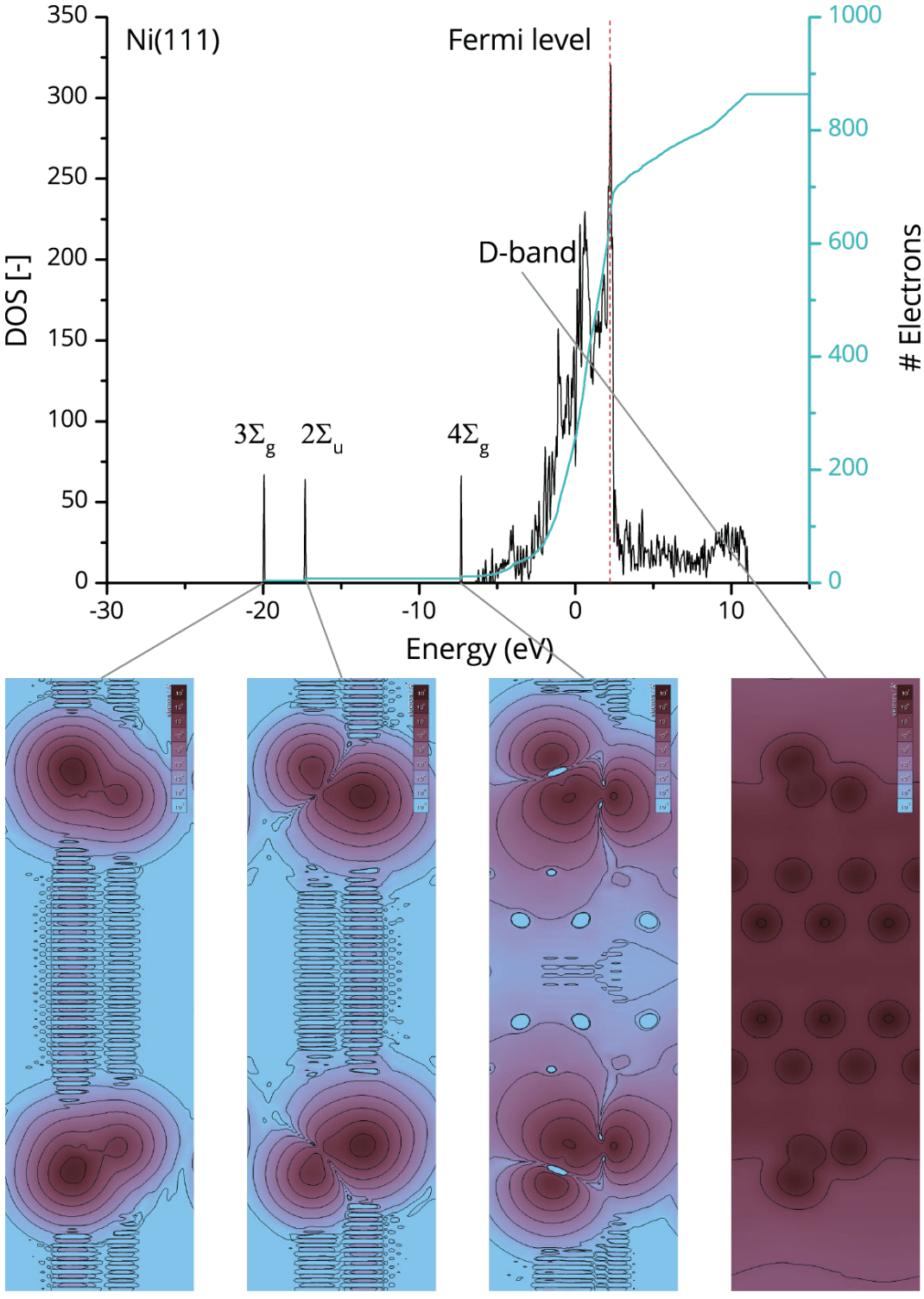

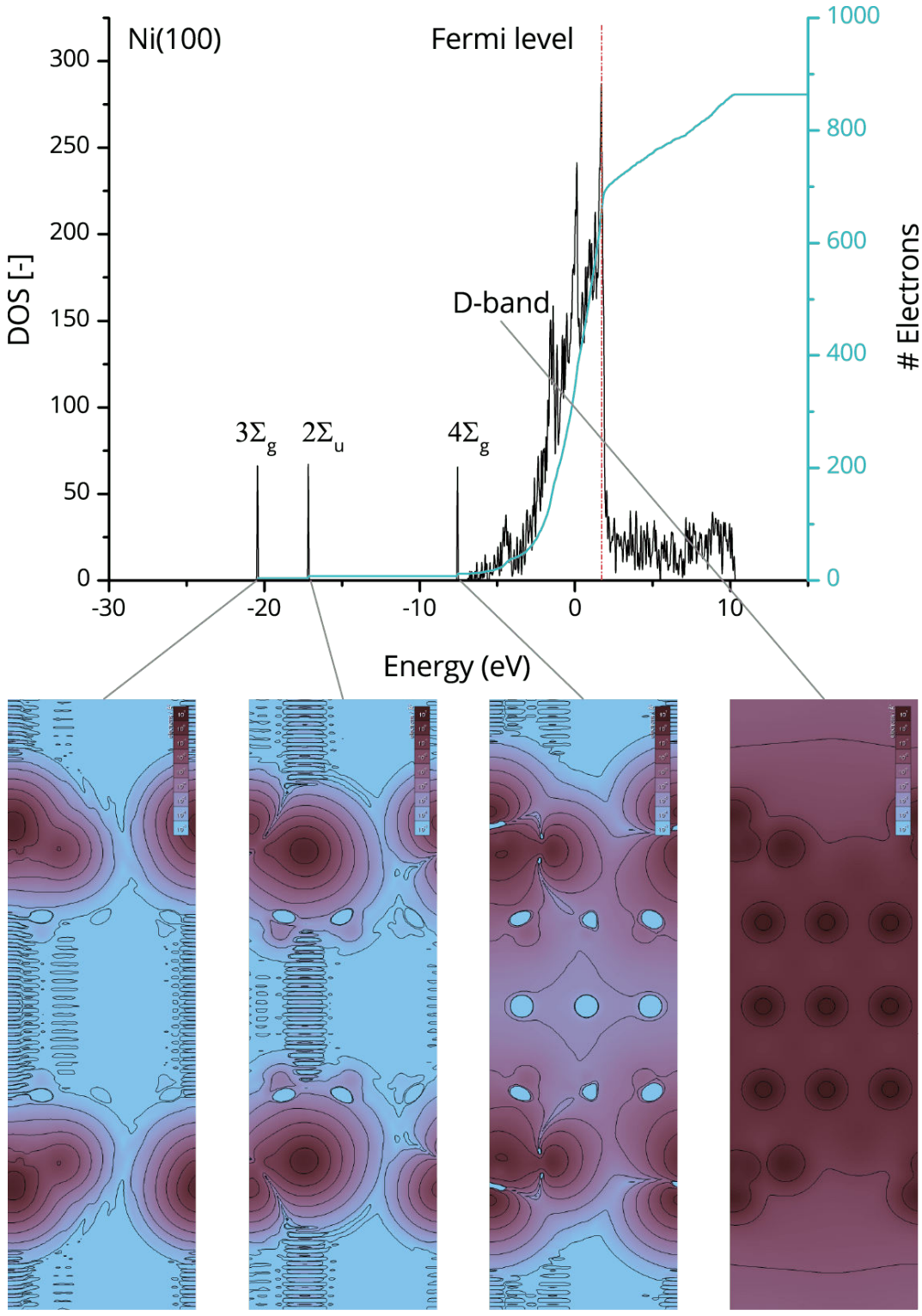
Ni(100)
Fermi level
D-band
$3\Sigma_g$
$2\Sigma_u$
$4\Sigma_g$
DOS [-]
Electrons
Energy (eV)
300
250
200
150
100
50
0
1000
800
600
400
200
0
-30
-20
-10
0
10

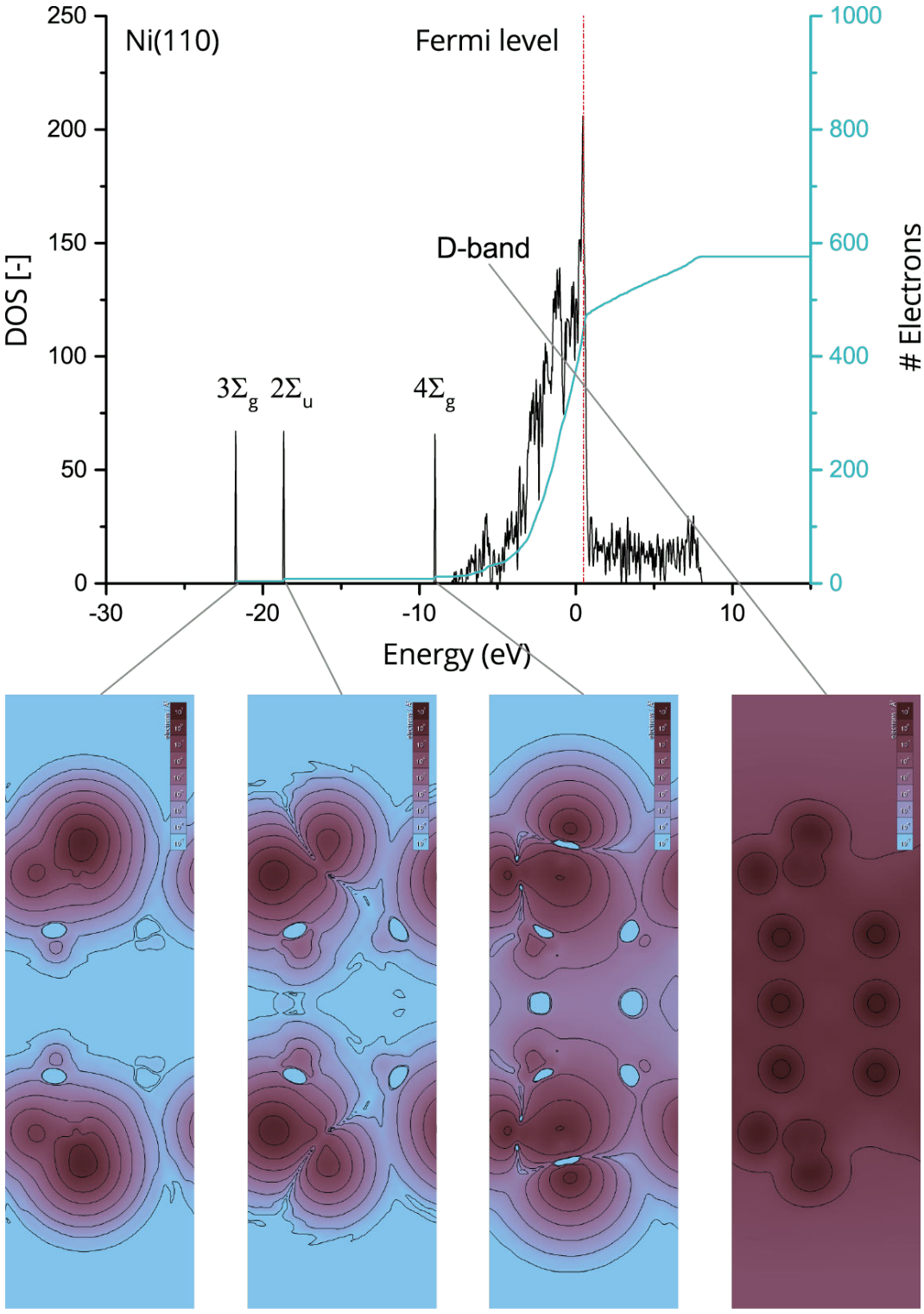
Ni(110)
Fermi level
D-band
$3\Sigma_g$ $2\Sigma_u$
$4\Sigma_g$
DOS [-]
Electrons
Energy (eV)
250
200
150
100
50
0
1000
800
600
400
200
0
-30
-20
-10
0
10

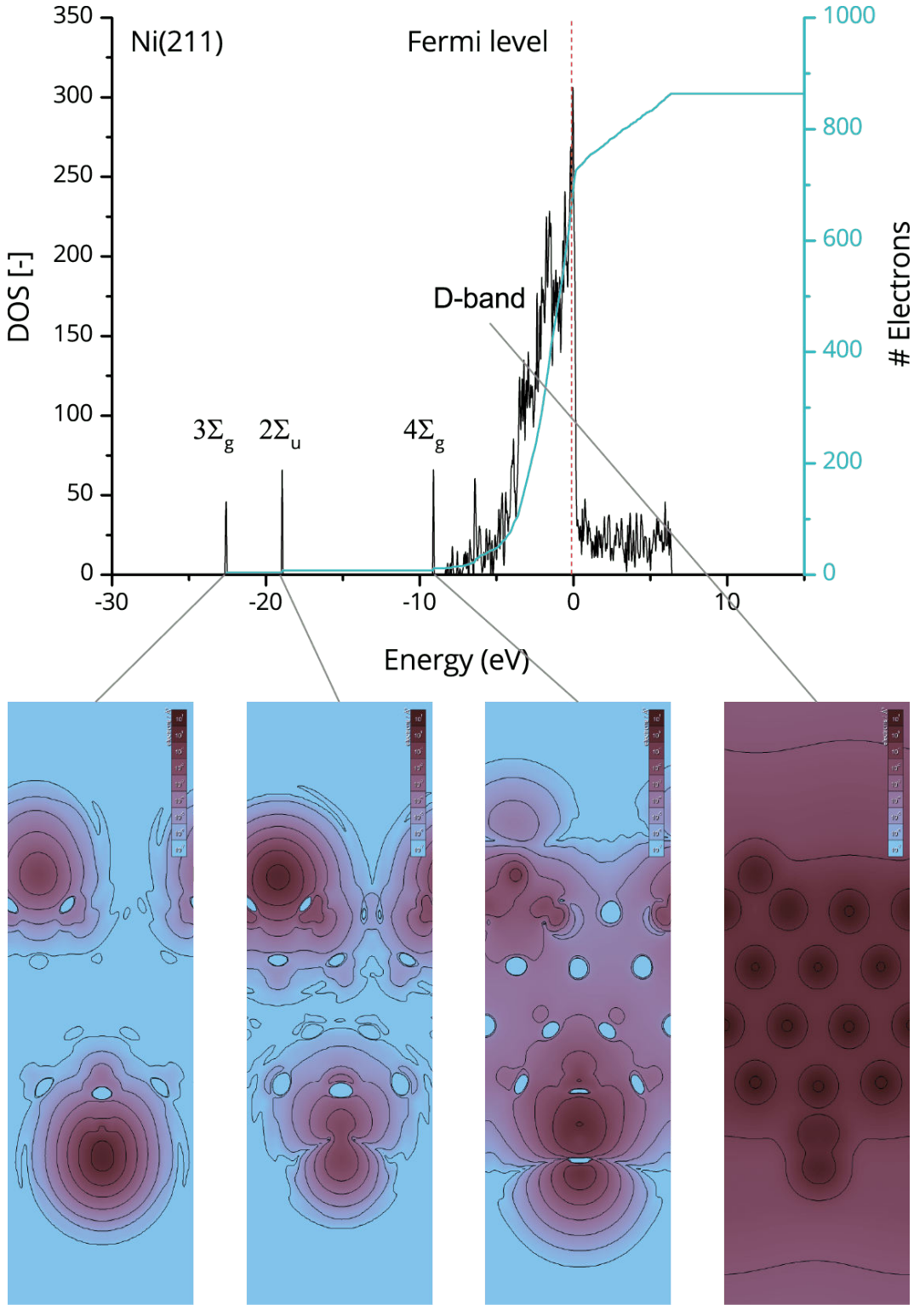
Ni(211)
Fermi level
D-band
$3\Sigma_g$
$2\Sigma_u$
$4\Sigma_g$
DOS [-]
Electrons
Energy (eV)
350
300
250
200
150
100
50
0
1000
800
600
400
200
0
-30
-20
-10
0
10